

The Pennsylvania State University

The Graduate School

College of Engineering

**INVESTIGATION OF NOISE REDUCTION METHODS ON SUPERSONIC JETS
EXHAUSTING FROM SCALE MODELS OF MILITARY STYLE NOZZLES**

A Thesis in

Aerospace Engineering

by

Russell W. W. Powers

© 2012 Russell W. W. Powers

Submitted in Partial Fulfillment
of the Requirements
for the Degree of

Master of Science

August 2012

The thesis of Russell W. W. Powers was reviewed and approved* by the following:

Dennis K. McLaughlin
Professor of Aerospace Engineering
Thesis Advisor

Philip J. Morris
Professor of Aerospace Engineering
Boeing / A.D. Welliver Professor of Aerospace Engineering

George A. Lesieutre
Professor of Aerospace Engineering
Head of the Department of Aerospace Engineering

*Signatures are on file in the Graduate School

ABSTRACT

Increasingly powerful and noisy military aircraft have generated the need for research leading to the development of supersonic jet noise reduction devices. The hot high speed supersonic jets exhausting from military aircraft during takeoff present a most challenging problem. Laboratory measurements are important so that noise reduction concepts can be evaluated early in the design process. Experimental research was conducted in the Penn State high speed jet noise facility on two separate methods of noise reduction of supersonic jet flows. The first noise reduction method was the beveled exit plane nozzle concept explored most recently by Viswanathan and the second was the internal nozzle corrugations pioneered by Seiner *et al.* The combination of the two methods was also explored.

The jet plume from beveled nozzles was examined and shown to deflect less than 5 degrees for both over-expanded and under-expanded flows. A new method of rotating the exit plane about the centerline was used to create the beveled nozzles. This results in an extension of the bottom lip and a shortening of the top lip. Results show that for heated jets, noise in the peak emission direction was reduced by 3-4 dB on the long lip side of the nozzle. Similar magnitudes of noise reductions were still present with the forward flight capability being used. A novel research idea of creating fluidic corrugations similar to the nozzle corrugations has been started by Penn State. To further the understanding and analysis of the fluidic corrugations, the present study focused on the flow field and acoustic field of nozzles with two, three, and six nozzle corrugations. The effect of the combination of the internal corrugations with a beveled nozzle was explored. The results show that significant noise reductions of over 3 dB of both the mixing noise and the broad band shock associated noise can be achieved. Additionally, the combination nozzle was shown to reduce the noise over a wider range of polar angles and operating conditions than either the purely beveled nozzle or the nozzle with only hard walled nozzle corrugations.

Table of Contents

LIST OF FIGURES	vi
LIST OF TABLES	xi
LIST OF SYMBOLS	xii
ACKNOWLEDGEMENTS	xv
Chapter 1 Introduction	1
1.1 Motivation	1
1.2 Aerodynamic Noise Theory	2
1.2.1 Definition of Important Parameters	3
1.2.2 Components of Jet Noise	4
1.3 Effect of Scaling on the Jet Noise Acoustics	8
1.3.1 The Effect of Noise Source Distribution	9
1.4 Nozzle Modifications for Noise Reduction	10
1.5 Scope of Thesis	11
1.5.1 Research Objectives	11
1.5.2 Thesis synopsis	12
Chapter 2 Facility Description	14
2.1 High Speed Jet Noise Facility at the Pennsylvania State University	14
2.2 The Use of Helium for Heat-Simulated Supersonic Jets	17
2.3 Forward Flight Simulation	18
Chapter 3 Experimental Setup and Methodology	20
3.1 Data Acquisition	20
3.2 Acoustic Measurements	20
3.3 Schlieren and Shadowgraph Setup	23
3.3.1 Overview	23
3.3.2 Image Acquisition and Equipment Settings	25
3.4 Model Geometry of Military-Style Supersonic Converging-Diverging Nozzles	28
3.5 Methodology for Creating the Corrugation Nozzle	31
3.5.1 Axisymmetric Method of Characteristics Design	32
3.5.2 Corrugation Design	34
Chapter 4 Examination of the Effects of the Beveled Exit Plane on a Supersonic Converging-Diverging Nozzle	36
4.1 Motivation and Review of Prior Work	36
4.2 Flow Field Analysis	38
4.3 Acoustic Results and Noise Reduction	40

Chapter 5 Examination of the Effects of Interior Hard Walled Nozzle Corrugations	49
5.1 Motivation and Review of Prior Work.....	49
5.2 Flow Field Analysis	52
5.3 Acoustic Results and Noise Reduction	61
5.3.1 Unheated (Cold) Jets	61
5.3.2 Heat Simulated Jets	65
Chapter 6 Comparison of the Combination of Interior Hard Walled Nozzle Corrugations and a Beveled Exit Plane	71
6.1 Motivation and Review of Prior Work.....	71
6.2 Flow Field Analysis	72
6.3 Acoustic Results and Noise Reduction	73
6.3.1 Unheated (Cold) Jets	73
6.3.2 Heat Simulated Jets	75
Chapter 7 Conclusions and Future Work.....	80
7.1 Summary of Goals	80
7.2 Major Results	81
7.3 Future Work	82
Bibliography	84
Appendix Processing Codes	88

LIST OF FIGURES

Figure 1.1: Similarity spectra on the two components of mixing noise: Large Scale Turbulent Mixing Noise (Red) and Fine Scale Turbulent Mixing Noise (Blue)	5
Figure 1.2: Averaged Schlieren image of an over-expanded jet issuing from a converging-diverging military-style nozzle.	7
Figure 2.1: Schematic and Photograph of the Pennsylvania State University High Speed Jet Noise Facility.....	14
Figure 3.1: Flow Chart of the Data Acquisition Process	21
Figure 3.2: Schlieren/Shadowgraph Z-type Setup used in the High Speed Jet Noise Facility at the Pennsylvania State University.....	24
Figure 3.3: Comparison between the A) Old Low Resolution Camera, and the B) New High Resolution Mightex Camera at a similar jet condition.....	26
Figure 3.4: Image Comparison between three different techniques of Schlieren and Shadowgraph at the same nozzle pressure ratio. A) Instantaneous Shadowgraph Image, $TTR = 1$. B) Digitally Averaged Shadowgraph Image, $TTR = 1$. C) Optically Averaged Schlieren Image, $TTR = 1.2$	28
Figure 3.5: The Beveled Nozzles – Left: 2-D Cross-Sectional Drawing; Right: Image of Rapid Prototyped Nozzles.....	30
Figure 3.6: Image of the corrugation nozzles used in this study. From left to right, top row: Md1.65 Baseline, Md1.65 2Corrug, Md1.65 3Corrug. Bottom row: Md1.65 6Corrug, Md1.65 6CorBev35	31
Figure 3.7: The Hard Walled Corrugation Design. Shown in the plot are the Normalized effective nozzle radius of the baseline nozzle (without corrugations) and the Method of Characteristics designed nozzle (baseline nozzle with corrugations). Also shown is the distance to the tip of the corrugation at each axial location.....	34
Figure 3.8: Computer-Aided Design Renders of the Military-Style Nozzle with Six Corrugations (Left), and Six Corrugations and a Beveled Exit Plane (Right)	35
Figure 4.1: Shadowgraph Images – Top Row: $M_j = 1.4$; Center Row: $M_j = 1.6$; Bottom Row: $M_j = 1.9$ Left: Baseline Nozzle; Middle Bevel24 Nozzle, Right: Bevel35 Nozzle	38

Figure 4.2: Top – Schlieren Imagery of the Bevel24 Nozzle with M_j (from Left to Right) = 1.47, 1.64, 1.77 Bottom – Comparison of the Flow Exit Angles at $M_j = 1.47$, 1.64, 1.77.....	39
Figure 4.3: Spectra and <i>OASPL</i> Comparison of Heated jets, measured at $\phi = 0^\circ$ (Long Lip Side), issuing from $M_d = 1.65$ Beveled Nozzle, with $M_j = 1.47$, $TTR = 3$, $D_{noz} = 0.708''$, $f_c = 42693$ Hz, Scaled $R/D_j = 100$	41
Figure 4.4: Spectra and <i>OASPL</i> Comparison of Heated jets, measured at $\phi = 180^\circ$ (Short Lip Side), issuing from $M_d = 1.65$ Beveled Nozzle, with $M_j = 1.47$, $TTR = 3$, $D_{noz} = 0.708''$, $f_c = 42693$ Hz, Scaled $R/D_j = 100$	41
Figure 4.5: Spectra and <i>OASPL</i> Comparison of Heated jets, measured at $\phi = 0^\circ$ (Long Lip Side), issuing from $M_d = 1.65$ Beveled Nozzle, with $M_j = 1.64$, $TTR = 3$, $D_{noz} = 0.708''$, $f_c = 43644$ Hz, Scaled $R/D_j = 100$	42
Figure 4.6: Spectra and <i>OASPL</i> Comparison of Heated jets, measured at $\phi = 180^\circ$ (Short Lip Side), issuing from $M_d = 1.65$ Beveled Nozzle, with $M_j = 1.64$, $TTR = 3$, $D_{noz} = 0.708''$, $f_c = 43644$ Hz, Scaled $R/D_j = 100$	42
Figure 4.7: Spectra and <i>OASPL</i> Comparison of Heated jets issuing from $M_d = 1.65$ Beveled Nozzle, with $M_j = 1.47$, $TTR = 3$, $D_{noz} = 0.708''$, $f_c = 42693$ Hz, Scaled $R/D_j = 100$. The beveled nozzle jet data are shown for various azimuthal angles.	44
Figure 4.8: Spectra and <i>OASPL</i> Comparison of Heated jets issuing from $M_d = 1.65$ Beveled Nozzle, with $M_j = 1.64$, $TTR = 3$, $D_{noz} = 0.708''$, $f_c = 43644$ Hz, Scaled $R/D_j = 100$, again at various azimuthal angles.	44
Figure 4.9: Spectra and <i>OASPL</i> Comparison of Heated jets, issuing from Md1.65 Bevel35 Nozzle, with $NPR = 3.0$, $M_j = 1.36$, $TTR = 3$, $D_{noz} = 0.708''$, $f_c = 41562$ Hz, Scaled $R/D_j = 100$	46
Figure 4.10: Delta <i>OASPL</i> Azimuthal Comparison of Heated jets issuing from Md1.65 Bevel35 Nozzle, with $NPR = 3.0$, $M_j = 1.36$, $TTR = 3$	46
Figure 4.11: Spectra and <i>OASPL</i> Comparison of Heated Baseline jet with and without Forward Flight, issuing $M_d = 1.65$ Beveled Nozzle, with $M_j = 1.47$, $TTR = 3$, $D_{noz} = 0.708''$, $f_c = 42693$ Hz, Scaled $R/D_j = 100$. The forward flight data have been corrected for outer stream shear layer refraction.	48
Figure 4.12: Spectra and <i>OASPL</i> Comparison of Heated jets issuing from $M_d = 1.65$ Beveled Nozzle, with Forward Flight of $M_f = 0.17$, with $M_j = 1.47$, $TTR = 3$, $D_{noz} = 0.708''$, $f_c = 42693$ Hz, Scaled $R/D_j = 100$	48
Figure 5.1: Narrowband Spectra Data from Seiner <i>et al.</i> [44] at model scale (1/10th Scale) which shows the effect of the interior nozzle corrugations. Three polar angles (measured from the upstream axis) are shown.....	50

Figure 5.2: *OASPL* Data from Seiner *et al.* [44] [25] which shows the effect of the interior nozzle corrugations. The left image is model scale (1/10th Scale) and the right is a full scale test. The polar angles are measured from the upstream axis.50

Figure 5.3: Averaged Shadowgraph Imagery of jets issuing from three different nozzles with $NPR = 3.0$, $M_j = 1.36$, $TTR = 1.2$, $D_{noz} = 0.708''$. From top to bottom the nozzles in each image are Md1.65 Baseline, Md1.65 2Corrug (Horizontal), Md1.65 2Corrug (Vertical). To the left of each image is also a description and visualization of the nozzle being used.54

Figure 5.4: Averaged Shadowgraph Imagery of jets issuing from three different nozzles with $NPR = 3.0$, $M_j = 1.36$, $TTR = 1.2$, $D_{noz} = 0.708''$. From top to bottom the nozzles in each image are Md1.65 3Corrug (Horizontal), Md1.65 3Corrug (Vertical), Md1.65 6Corrug. To the left of each image is also a description and visualization of the nozzle being used.55

Figure 5.5: Averaged Shadowgraph Imagery of jets issuing from three different nozzles with $NPR = 3.5$, $M_j = 1.47$, $TTR = 1.2$, $D_{noz} = 0.708''$. From top to bottom the nozzles in each image are Md1.65 Baseline, Md1.65 2Corrug (Horizontal), Md1.65 2Corrug (Vertical). To the left of each image is also a description and visualization of the nozzle being used.57

Figure 5.6: Averaged Shadowgraph Imagery of jets issuing from three different nozzles with $NPR = 3.5$, $M_j = 1.47$, $TTR = 1.2$, $D_{noz} = 0.708''$. From top to bottom the nozzles in each image are Md1.65 3Corrug (Horizontal), Md1.65 3Corrug (Vertical), Md1.65 6Corrug. To the left of each image is also a description and visualization of the nozzle being used.58

Figure 5.7: Averaged Schlieren Imagery of jets issuing from two different nozzles at two azimuthal orientations each with $NPR = 3.5$, $M_j = 1.47$, $TTR = 1.2$, $D_{noz} = 0.708''$. From top to bottom the nozzles in each image are Md1.65 2Corrug (Horizontal), Md1.65 2Corrug (Vertical), Md1.65 6Corrug (Horizontal), and Md1.65 6Corrug (Vertical). To the left of each image is also a description and visualization of the nozzle being used.59

Figure 5.8: Averaged Shadowgraph Imagery of jets issuing from two different nozzles with $NPR = 4.0$, $M_j = 1.56$, $TTR = 1$, $D_{noz} = 0.708''$. From top to bottom the nozzles in each image are Md1.65 3Corrug Baseline, Md1.65 6Corrug. To the left of each image is also a description and visualization of the nozzle being used.61

Figure 5.9: Spectra and *OASPL* Comparison of Heated jets, measured at two azimuthal angles, issuing from Md1.65 2Corrug Nozzle, with $NPR = 3.05$, $M_j = 1.37$, $TTR = 1$, $D_{noz} = 0.708''$, $f_c = 24085 \text{ Hz}$, Scaled $R/D_j = 100$ 63

Figure 5.10: Spectra and *OASPL* Comparison of Heated jets, measured at three azimuthal angles, issuing from Md1.65 3Corrug Nozzle, with $NPR = 3.05$, $M_j = 1.37$, $TTR = 1$, $D_{noz} = 0.708''$, $f_c = 24085 \text{ Hz}$, Scaled $R/D_j = 100$ 63

- Figure 5.11:** Spectra and *OASPL* Comparison of Heated jets, measured at two azimuthal angles, issuing from Md1.65 **6Corrug** Nozzle, with $NPR = 3.05$, $M_j = 1.37$, $TTR = 1$, $D_{noz} = 0.708''$, $f_c = 24085$ Hz, Scaled $R/D_j = 100$ 64
- Figure 5.12:** Spectra and *OASPL* Comparison of Heated jets, measured at two azimuthal angles, issuing from Md1.65 **6Corrug** Nozzle, with $NPR = 3.5$, $M_j = 1.47$, $TTR = 1$, $D_{noz} = 0.708''$, $f_c = 24673$ Hz, Scaled $R/D_j = 100$ 64
- Figure 5.13:** Spectra and *OASPL* Comparison of Heated jets, measured at two azimuthal angles, issuing from Md1.65 **2Corrug** Nozzle, with $NPR = 3.0$, $M_j = 1.36$, $TTR = 3$, $D_{noz} = 0.708''$, $f_c = 41562$ Hz, Scaled $R/D_j = 100$ 66
- Figure 5.14:** Spectra and *OASPL* Comparison of Heated jets, measured at two azimuthal angles, issuing from Md1.65 **3Corrug** Nozzle, with $NPR = 3.0$, $M_j = 1.36$, $TTR = 3$, $D_{noz} = 0.708''$, $f_c = 41562$ Hz, Scaled $R/D_j = 100$ 66
- Figure 5.15:** Spectra and *OASPL* Comparison of Heated jets, measured at two azimuthal angles, issuing from Md1.65 **2Corrug** Nozzle, with $NPR = 3.5$, $M_j = 1.47$, $TTR = 3$, $D_{noz} = 0.708''$, $f_c = 42735$ Hz, Scaled $R/D_j = 100$ 67
- Figure 5.16:** Spectra and *OASPL* Comparison of Heated jets, measured at two azimuthal angles, issuing from Md1.65 **3Corrug** Nozzle, with $NPR = 3.5$, $M_j = 1.47$, $TTR = 3$, $D_{noz} = 0.708''$, $f_c = 42735$ Hz, Scaled $R/D_j = 100$ 67
- Figure 5.17:** Spectra and *OASPL* Comparison of Heated jets, issuing from Md1.65 **6Corrug** Nozzle, with $NPR = 3.0$, $M_j = 1.36$, $TTR = 3$, $D_{noz} = 0.708''$, $f_c = 41562$ Hz, Scaled $R/D_j = 100$69
- Figure 5.18:** Spectra and *OASPL* Comparison of Heated jets, issuing from Md1.65 **6Corrug** Nozzle, with $NPR = 3.5$, $M_j = 1.47$, $TTR = 3$, $D_{noz} = 0.708''$, $f_c = 42735$ Hz, Scaled $R/D_j = 100$69
- Figure 5.19:** Spectra and *OASPL* Comparison of Heated jets, issuing from Md1.65 **6Corrug** Nozzle, with $NPR = 4.0$, $M_j = 1.56$, $TTR = 3$, $D_{noz} = 0.708''$, $f_c = 43531$ Hz, Scaled $R/D_j = 100$70
- Figure 6.1:** Averaged Shadowgraph Imagery of jets issuing from the Md1.65 6CorBev35 Nozzle with three different jet conditions. All jets are $TTR = 1$, $D_{noz} = 0.708''$. From top to bottom the jet conditions in each image are $NPR = 3.0$, $NPR = 3.5$, $NPR = 4.0$. To the left of each image is also a description and visualization of the nozzle being used.72
- Figure 6.2:** Spectra and *OASPL* Comparison of Cold jets, issuing from Md1.65 **6CorBev35** Nozzle from three azimuthal orientations on the long lip side, with $NPR = 3.05$, $M_j = 1.37$, $TTR = 1$, $D_{noz} = 0.708''$, $f_c = 24085$ Hz, Scaled $R/D_j = 100$74
- Figure 6.3:** Spectra and *OASPL* Comparison of Cold jets, issuing from Md1.65 **6CorBev35** Nozzle from three azimuthal orientations on the short lip side, with $NPR = 3.05$, $M_j = 1.37$, $TTR = 1$, $D_{noz} = 0.708''$, $f_c = 24085$ Hz, Scaled $R/D_j = 100$74

Figure 6.4: Spectra and <i>OASPL</i> Comparison of Heated jets, issuing from Md1.65 6CorBev35 Nozzle, with $NPR = 3.0$, $M_j = 1.36$, $TTR = 3$, $D_{noz} = 0.708''$, $f_c = 41562$ Hz, Scaled $R/D_j = 100$	76
Figure 6.5: Spectra and <i>OASPL</i> Comparison of Heated jets, issuing from Md1.65 6Corrug , Md1.65 Bevel35 , and Md1.65 6CorBev35 Nozzles with $NPR = 3.0$, $M_j = 1.36$, $TTR = 3$, $D_{noz} = 0.708''$, $f_c = 41562$ Hz, Scaled $R/D_j = 100$	76
Figure 6.6: Spectra and <i>OASPL</i> Comparison of Heated jets, issuing from Md1.65 6CorBev35 Nozzle, with $NPR = 3.5$, $M_j = 1.47$, $TTR = 3$, $D_{noz} = 0.708''$, $f_c = 42735$ Hz, Scaled $R/D_j = 100$	77
Figure 6.7: Spectra and <i>OASPL</i> Comparison of Heated jets, issuing from Md1.65 6Corrug , Md1.65 Bevel35 , and Md1.65 6CorBev35 Nozzles with $NPR = 3.5$, $M_j = 1.47$, $TTR = 3$, $D_{noz} = 0.708''$, $f_c = 42735$ Hz, Scaled $R/D_j = 100$	77
Figure 6.8: Delta <i>OASPL</i> Comparison for Different Nozzles, $NPR = 3.0$, $M_j = 1.36$, $TTR = 3$	78
Figure 6.9: Delta <i>OASPL</i> Comparison for Different Nozzles, $NPR = 3.5$, $M_j = 1.47$, $TTR = 3$	79
Figure 6.10: Delta <i>OASPL</i> Comparison for Different Nozzles, $NPR = 4.0$, $M_j = 1.56$, $TTR = 3$	79

LIST OF TABLES

Table 4.1: Nozzle Parameters and Jet Conditions for Experiments	37
Table 5.1: Nozzle Parameters and Jet Conditions for Experiments	52

LIST OF SYMBOLS

U_j	=	jet velocity
p_0	=	jet stagnation pressure
p_∞	=	ambient pressure
NPR	=	nozzle pressure ratio
D, D_{noz}	=	diameter of nozzle at exit plane
R	=	physical distance of the microphones from the jet exit
a_j	=	jet acoustic velocity
M_j	=	average Mach number of the fully expanded jet
M_d	=	design Mach number of the nozzle
D_j	=	fully expanded diameter of the jet plume
γ	=	specific heat ratio of air
f	=	frequency
St	=	Strouhal number
f_c	=	characteristic frequency U_j / D_j
T_o	=	jet stagnation temperature
T_∞	=	ambient temperature
T_j	=	jet static temperature
TTR	=	total temperature ratio, T_o / T_∞
SPL	=	Sound pressure level
dB	=	decibel
μ	=	emission angle of Mach wave radiation
M_c	=	convection Mach number of the jet
M_j	=	average Mach number of the fully expanded jet

$BBSAN$	=	Broadband Shock Associated Noise
Re	=	Reynolds number
R_{gas}	=	gas constant for Air
$R_{gas,mix}$	=	gas constant for the helium-air mixture
a_{heated}	=	acoustic velocity of heated air
a_{mix}	=	acoustic velocity of helium-air mixture
γ_{mix}	=	specific heat ratio of helium-air mixture
$T_{j,mix}$	=	temperature of the jet of helium air mixture
ρ_j	=	density of the jet
$OASPL$	=	overall sound pressure level
θ	=	polar angle, measured from the jet downstream direction
ϕ	=	azimuthal angle, measurement zero depends on the specific nozzle
M_f	=	forward flight Mach number.
Δf	=	frequency resolution bandwidth
ΔSt	=	Strouhal resolution bandwidth
FFT	=	fast fourier transform
PSD	=	power spectral density
CCD	=	charge coupled device
$CMOS$	=	complementary metal-oxide-semiconductor
fps	=	frames per second
sps	=	spark flashes per second
FDM	=	rapid prototyping technique, fused deposition modeling
$HDSL$	=	rapid prototyping technique, high definition Stereolithography
MLN	=	minimum length nozzle

x	=	axial distance in the nozzle measured from the throat
r_{th}	=	radius of the nozzle at the throat
CAD	=	computer aided design

Subscripts:

j	:	quantity relative to the jet
raw	:	as measured
mix	:	quantity of a helium-air mixture jet
∞	:	ambient quantity
0	:	stagnation quantity

ACKNOWLEDGEMENTS

I would like to sincerely thank my thesis advisor, Prof. Dennis McLaughlin. I am very thankful for his academic and career advice and the opportunity to learn from his extensive experience. I am grateful for the fairness and encouragement he always provides when working with me. I would also like to thank Prof. Philip Morris for his many insights and discussions throughout my research.

I would like to thank the DoD SMART Program for my scholarship, along with my Mentor from NAVAIR Mr. Allan Aubert. This work was also partially supported by the Office of Naval Research and Lockheed Martin Corp.

I would like to thank post-doctoral fellow of the Aerospace Department Dr. Ching-Wen Kuo for his assistance and advice in laboratory experiments. Additional thanks also go to Richard Auhl, Mark Catalano and Kirk Heller for facility and technical help. I would also like to thank past and current graduate and undergraduate students who helped or contributed to this research, specifically, Benjamin Day, Maureen Senft, Chris Gumke, Brian Wallace, and Leighton Myers.

Lastly, I would like to thank my family and friends for their support and company.

Chapter 1

Introduction

1.1 Motivation

Military aircraft noise is becoming a more important topic for both the public at large and the United States government, specifically the U.S. Navy. The communities around airports and military bases are concerned with the noise levels during military aircraft operation. In commercial subsonic aircraft, the large bypass ratios and relatively slow jet exhaust speeds cause the dominant components of the noise to be spread almost equally between the aft fan, inlet fan, and main exhaust jet. Subsequently, the overall sound produced by the aircraft is lower than the noise produced by military aircraft with engines that produce supersonic jet exhausts. The hot supersonic jet exhausts of military aircraft, along with the required low bypass ratios due to drag considerations, cause the exhaust jet to be the dominant noise source. Additionally, because of the complex nature of this hot supersonic exhaust, and the very strict drag and weight considerations for military aircraft, the control and suppression of the noise of these fighter aircraft is a more complicated problem than in the commercial sector. This is even further exacerbated by the close proximity of Naval Aircraft Carrier personnel to these aircraft during launch. Furthermore, it is not unforeseeable that in the future, noise emission regulations will be implemented for military aircraft. For all these reasons there are current efforts being made to develop new methods and improve upon old methods to reduce the noise produced by such aircraft.

1.2 Aerodynamic Noise Theory

The noise produced by jet exhausts is a complex subject, and there have been many years of research to better understand and model the physics of the jet. The hot supersonic jet exhausts that are produced by military aircraft engines add another layer of complexity to the jet noise field. To date, there has not been a comprehensive summary of past research and the current understanding of these jet exhausts. However, key references and a brief summary of the important developments in the field will be given.

Sir James Lighthill [1] [2] published two papers in 1952 and 1954 which founded the field of aeroacoustics. Beginning with the momentum equation and rearranging terms to create a source term, Lighthill obtained the inhomogeneous wave equation, which formed the foundation of Lighthill's Acoustic Analogy Theory. This derivation separates wave propagation from the sound sources which behave as quadrupoles. He further developed his theory to show that the acoustic power radiated by a jet varies with the eighth power of the jet velocity, U_j^8 . Several modifications and extensions to the Acoustic Analogy Theory have been made. Ffowcs-Williams [3] concluded that by including source convection terms the scaling law actually behaves as the third power of velocity, U_j^3 , for very high speed jets. Lilley [4] then extended the theory to include mean flow refraction of the sound waves. The propagation of the sound waves through the non-uniform jet flow causes a refraction of the waves away from the direction of the jet, and creates the cone of silence close to the jet axis.

Before continuing with more in depth discussion, important parameters and notation which are commonly used throughout this and the following chapters will be defined.

1.2.1 Definition of Important Parameters

The jets used in this study all exhausted from small scale nozzles which use the same internal geometry as the engine exhaust nozzle of the GE 404 engine in the F-18 military fighter aircraft. The nozzle exit diameter is given by D , and is used to non-dimensionalize the position of the microphones to more easily compare to larger scale tests. The distance from the microphones to the jet, R , is normally presented as the non-dimensional position R/D . The ratio between the jet velocity, U_j , and the speed of sound within the jet, a_j , is the jet Mach number, M_j . The nozzle pressure ratio (NPR) is calculated by dividing the stagnation pressure, p_0 , upstream of the nozzle by the ambient pressure, p_∞ , at the nozzle exit. The jet exit Mach number can be calculated from the nozzle pressure ratio using the isentropic flow relations. The design Mach number of the nozzle, M_d , is the Mach number at the exit if the flow is expanded from high pressure to a static pressure that is exactly ambient pressure. Therefore when a nozzle operates at a nozzle pressure ratio that results in a jet Mach number which is lower than the design Mach number, the flow is said to be over-expanded, and the exit static pressure is lower than the ambient pressure. When the exit pressure is higher than the ambient pressure (jet Mach number higher than design Mach number) the flow is under-expanded. The design Mach number of the nozzle can also be calculated from the exit area to throat area ratio using the isentropic relations.

The pressure differences at the exit of the nozzle for over- and under-expanded jets cause the diameter of the jet to shrink or expand, respectively. Because of altitude and operational considerations, typical military jet engines have over-expanded flow during the takeoff portion of the flight. A spatially averaged jet diameter, D_j , can be calculated using equation 1.1, which is derived from isentropic relations. This is accurate for the first few diameters of the flow near the nozzle exit, which is prior to the downstream mixing of the jet flow.

$$D_j = \left[\frac{1 + \frac{\gamma-1}{2} M_j^2}{1 + \frac{\gamma-1}{2} M_d^2} \right]^{\frac{\gamma+1}{4(\gamma-1)}} \left(\frac{M_d}{M_j} \right)^{1/2} D \quad 1.1$$

As the final goal of any research involving the potential noise reduction of supersonic jets is to implement at full-scale, efforts must be made to make comparisons between nozzle sizes easy; this is achieved through the use of non-dimensional acoustic spectra. The frequency content of the noise produced by jet flow depends upon the diameter of the jet. For this reason, the Strouhal number, St , frequency divided by the characteristic frequency, f_c , is commonly used.

$$St = \frac{f}{f_c}, \text{ where } f_c = \frac{U_j}{D_j} \quad 1.2$$

The study of hot jets requires the use of a parameter which defines the jet temperature. The total temperature of the jet, T_0 , is more easily directly measured than the static temperature and thus the total temperature ratio (TTR) is used. The total temperature ratio is the total temperature of the jet divided by the ambient temperature. This can be found using equation 1.3.

$$TTR = \frac{T_0}{T_\infty} = \frac{T_j}{T_\infty} \left(1 + \frac{\gamma-1}{2} M_j^2 \right) \quad 1.3$$

1.2.2 Components of Jet Noise

The noise field produced by exhaust jets can be described in terms of two components. These components consist of turbulent mixing noise and shock-associated noise, each radiating from different portions of the jet and contributing to the far field noise with different spatial distributions. The turbulent mixing noise is present in all jets, hot and cold, supersonic and subsonic, while the shock associated noise only occurs in supersonic shock containing jets.

1.2.2.1 Turbulent Mixing Noise

Turbulent mixing noise is present in all jets at all observation positions, and is the only source of noise for subsonic or fully-expanded supersonic jets. It contains broad frequency content with a varying peak amplitude and corresponding frequency at varying observation polar angle. Upon the discovery of large coherent turbulent structures in shear layers [5] [6] [7], jet noise research began to change direction. Researchers have shown that the turbulent mixing noise is itself comprised of two components, the fine scale turbulent mixing noise and the large scale turbulent mixing noise. By fitting two spectra to all of the jet noise data in the NASA Langley database Tam, Golebiowski, and Seiner [8] found two empirical spectra that corresponded to the large scale and fine scale turbulent mixing noise. These spectra have been shown to fit most noise fields produced by shock free jets (either subsonic or perfectly-expanded supersonic). The two similarity spectra produced are shown in Figure 1.1.

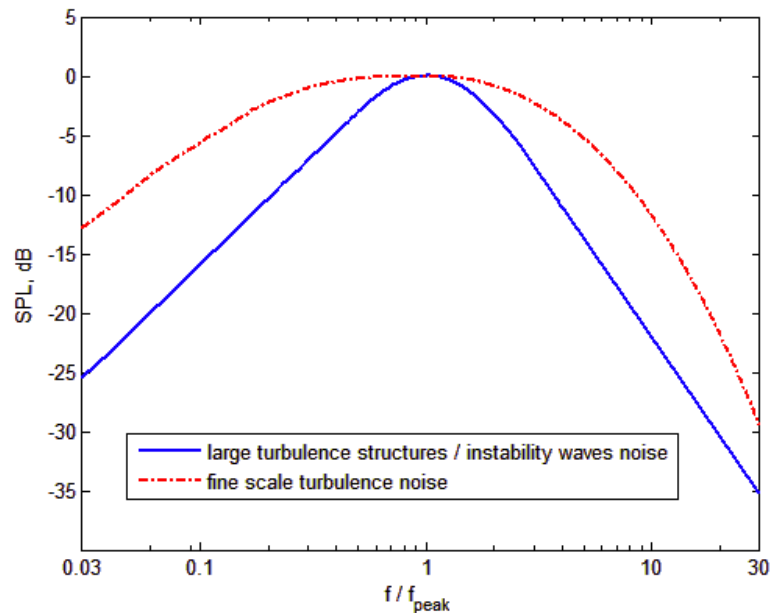


Figure 1.1: Similarity spectra on the two components of mixing noise: Large Scale Turbulent Mixing Noise (Red) and Fine Scale Turbulent Mixing Noise (Blue)

The axially coherent large scale structures emit Mach wave radiation when they convect supersonically with respect to the ambient acoustic velocity. The Mach wave radiation can be modeled simply using the wavy wall analogy. The direction of the Mach wave radiation can be found by using the convection Mach number, M_c , which is the velocity of the large coherent structures divided by the ambient acoustic velocity. The relation between the angle of emission of the Mach wave radiation and the convection Mach number is given by equation 1.4. A good summary of Mach wave radiation is given by Krothapalli *et al.* [9].

$$\mu = \sin^{-1} \left(1/M_c \right) \quad 1.4$$

It has however been shown that jets with convection Mach numbers that are subsonic sometimes still emit noise in a similar fashion to Mach wave radiation. The instability wave model attempts to describe the large scale coherent turbulent structures and the Mach wave phenomena. Morris and Tam [10] developed the theoretical model which treats the structures as a linear superposition of instability waves and extended it in further studies [11] [12]. Validation that the large scale coherent structures can be described by the instability wave model was done with experimental measurements performed in laboratory scale facilities by McLaughlin *et al.* [13], Morrison and McLaughlin [14], and Troutt and McLaughlin [15]. The instability wave model uses small amplitudes near the nozzle exit which then grow to maximum amplitude and subsequently decrease as they propagate farther downstream. Physically, this corresponds to the growth and emergence of the large scale turbulent structures in the shear layer near the nozzle exit and then the subsequent decay. This growth and decay causes the wave number spectrum of the turbulence to be very broad. The result is that the phase velocity of different sized structures can be individually higher at high frequencies than the ambient acoustic velocity. As shown by Veltin, Day, and McLaughlin [16] this results in some portions of the spectrum producing Mach wave radiation, thus allowing subsonically convecting jets to produce Mach wave radiation.

1.2.2.2 Shock-Associated Noise

Supersonic jets issuing from conical nozzles and supersonic jets issuing from converging-diverging nozzles operating off the design condition both contain standing shock waves within the flow. With either under or over-expanded flow, the pressure difference at the nozzle exit causes the flow to either expand or contract, and because the flow is supersonic this can only occur through shocks or expansion waves. Shock waves propagate through the jet and are reflected from the opposing shear layer as expansion waves. This standing shock pattern commonly referred to as shock cell or shock diamond pattern, can be seen in the schlieren image of an over-expanded jet shown in Figure 1.2.

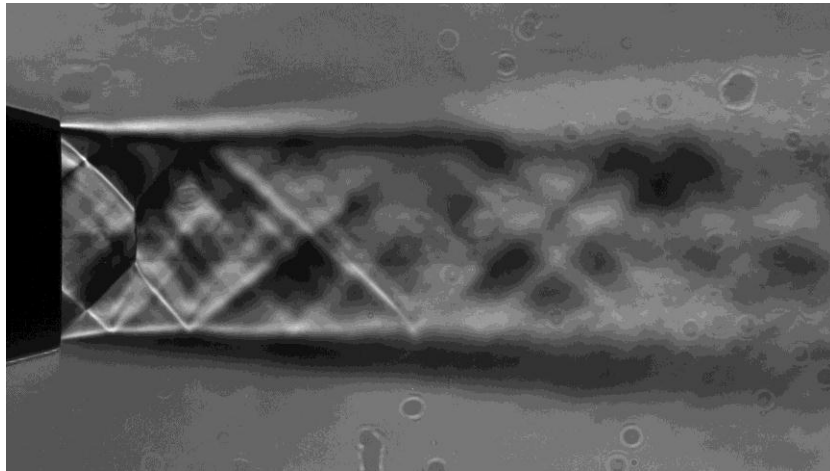


Figure 1.2: Averaged Schlieren image of an over-expanded jet issuing from a converging-diverging military-style nozzle.

The shock-associated noise only exists when there are standing shocks in the flow. There are two components of shock associated noise, the broadband shock associated noise (BBSAN) and screech. Broadband shock associated noise arises from the interaction between the large scale turbulent structures convecting downstream through the shear layer and the standing shock cell pattern. The broad frequency range of the structures convecting through the shock cells causes noise to be produced over a wide frequency range. The BBSAN is emitted over a broad range of

observation angles, but it is the dominant source in the acoustic sideline and forward arc (Angles above 90 degrees from the jet axis). In the aft arc the high energy large scale mixing noise overwhelms the acoustic spectra. It has been shown that the amplitude of the BBSAN is directly related to the pressure change across the shocks within the flow, which can be related to the design of the nozzle and the nozzle pressure ratio [17]. Many complex models have been created as attempts to model the BBSAN, such as a recent one by Miller and Morris [18]. The total temperature ratio of the jet has also been shown to have an effect on the amplitude and dominance of the BBSAN. A study by Kuo, Morris, and McLaughlin [19] showed these effects and documented that most of the effects of temperature are achieved once the total temperature ratio surpasses 2.0.

The second component of shock associated noise is screech. Screech occurs as discrete frequency tones in spectra at the same frequency over all observation angles. Screech tones occur due to a phase locked feedback loop between the shock noise and the nozzle exit. Many studies have been performed to understand [20], [21] model [22], and suppress the screech tones [23] [24], however it should be noted that the large temperature ratios in military engine exhaust jets normally break down the feedback loop and suppress the screech tones.

1.3 Effect of Scaling on the Jet Noise Acoustics

While the data obtained from full-scale acoustic measurements, either engine tie-down [25] or aircraft flyover [26], is very valuable, these studies can be very expensive and time consuming. Therefore in early design stages the use of small scale facilities, such as the High Speed Jet Noise facility at the Pennsylvania State University, are very important. While understanding of the physics and acoustics at small scales is desired, it is important to also be able to relate and compare to larger scale experiments. Many different researchers have compared and

analyzed experiments at the small ($\sim 1/35$), moderate ($\sim 1/5$), and full scale ($1/1$). A comprehensive review was performed by Viswanathan [27]. A major conclusion from this study is that the Reynolds' number of the jet needs exceed 500,000 to adequately reproduce the important components of the jet that contribute to the acoustic far field. Another important parameter is the interior geometry of the nozzle. Comparisons using the same military-style nozzle shapes between the small scale facility at Penn State and the moderate scale facility at NASA Glenn Research Center (GRC) were performed by Kuo and colleagues [28] [29] and more extensively in McLaughlin, Bridges, and Kuo [30]. These studies have shown excellent agreement between the PSU facility and the NASA GRC facility. An additional parameter to be aware of at the small scale is the nozzle lip thickness, as this can directly influence the feedback loop that causes the screech tones [31]. The non-dimensional comparison methodology used for these experiments is clearly outlined in reference [29] and will be discussed in more detail in section 3.2.

1.3.1 The Effect of Noise Source Distribution

The noise source of jets is distributed throughout the plume of the jet. The high frequency noise is mostly generated near the nozzle exit, while the low frequency noise is generated mostly near and somewhat downstream of the end of the potential core. Because of the distribution of the sound sources when placing microphones in the acoustic field at specific polar angles, it is important for the microphones to be far enough away to be considered in the acoustic far field. Many studies [32] [33] have been performed to attempt to quantify a lower limit upon which you are at the edge of the acoustic far field of the jet. Viswanathan [34] proposed that for a cold subsonic jet you must be at least 35 to nozzle diameters to achieve far field results. However it has been shown that the potential core of hot supersonic jets can be as much as twice as long as

subsonic jets [35]. As documented by Kuo [36] this causes the dominant noise sources of the jet to extend even farther downstream, and therefore to be in the acoustic far field the microphones should be over ~ 100 nozzle diameters away.

1.4 Nozzle Modifications for Noise Reduction

Many different design concepts which either modify the exhaust nozzle geometry or the jet flow have been researched in attempts to reduce the noise emitted by supersonic jets. Non-axisymmetric geometries such as rectangular nozzles [37] were among the first modifications to be explored. Chevrons have been thoroughly researched with many different design parameters, most recently by Henderson and Bridges [38] and Schlinker *et al.* [39]. They have been explored in the Penn State facility by Kuo, Veltin, and McLaughlin [40]. Chevrons have been shown to create counter-rotating vortices that propagate downstream which reduce the peak frequency noise by increasing mixing, but increase the high frequency noise through the increase of the fine scale turbulence. They are one of the most promising modifications because of their simple implementation and very minor impact on performance. They have already been tested and implemented at full-scale in several studies [41] [42], and there is currently a plan to put them in operation on active U.S. Navy F-18 aircraft. Additional modifications, such as the beveled nozzle exit plane [43], and interior nozzle corrugations [44] [45] have been shown to reduce the noise produced by supersonic jets and will be further explored in this study.

The corrugated nozzle inserts, pioneered by Seiner *et al.* [44] [45], reduce noise in two ways. First, they reduce and almost eliminate the dominate peak of the broadband shock associated noise because the effective area ratio is reduced which produces a perfectly expanded condition, rather than the over-expanded jet condition of current nozzle flows at aircraft take-off conditions. Second, they produce stream wise vortices, similar to chevrons, which (apparently)

increase mixing to reduce the length of high speed turbulent flow producing large scale structure noise. However, one of the main limitations of the corrugations is that while they reduce noise at takeoff conditions while not adversely affecting the thrust, they are not designed for, and subsequently negatively affect the engine operation (thrust) during cruise. While noise reduction is important during takeoff, nozzle corrugations were never fully implemented by the U.S. Navy because of these performance considerations.

For these reasons Penn State (Kuo, Morris and McLaughlin [46]) have initiated a research program to develop “fluidic corrugations” in a military style supersonic nozzle for noise reduction. The concept is that nozzle blowing would be activated for aircraft takeoff (for noise suppression) and altered for cruise flight where the blowing air would be diverted to its “normal” wall cooling function, and thus not negatively affecting engine performance.

1.5 Scope of Thesis

1.5.1 Research Objectives

The main goal of this study is to further the understanding of the acoustic field and noise generation mechanisms of two noise reduction methods, the converging-diverging beveled nozzle, and interior nozzle corrugations. The high speed jet noise laboratory at The Pennsylvania State University (PSU) has contributed to studies of jet noise source generation and suppression mechanisms for some time. Studies which focus on realistic and accurate representations of military style nozzle geometries and noise reduction concepts for these nozzles have been performed. The experiments in this study were performed with three major goals in mind.

- 1) Extend the results previously shown by Viswanathan and Czech [43] on the supersonic converging-diverging beveled nozzle. This study will be performed using a slightly different methodology in the design of the nozzle bevel.
- 2) Explore the interior nozzle corrugations used by Seiner *et al.* [44] [45]. The primary focus will be to create an understanding that can be used to help further the research of the “fluid corrugated” nozzle being used by Penn State. It is important to show that Penn State can replicate the same noise benefits Seiner *et al.* achieved in order to better understand the more complicated “fluid corrugated” nozzles. We refer to the conventional designs as “hard walled corrugated nozzles”.
- 3) Examine the effect of the combination of the beveled exit plane and interior nozzle corrugations. This combination has been only sparsely explored, it is not clearly understood whether the noise suppression mechanisms of these are different enough for the noise reduction to be additive.

1.5.2 Thesis synopsis

The remaining portions of this thesis evaluate several noise reduction nozzle modifications. Chapter 2 starts with a description of the High Speed Jet Noise Facility at the Pennsylvania State University. Attention is paid to the use of the forward flight systems and the use of helium in heat-simulated jets. Chapter 3 describes the setup and processing methodology for both the acoustic and flow visualization experiments. The military-style nozzle design used in this study will be examined, as well as a brief explanation of the method of characteristic design of an axisymmetric nozzle and the corresponding design of the hard walled corrugations.

The results are presented in Chapters 4, 5, and 6. Chapter 4 presents the acoustic measurements and flow field visualizations of converging-diverging beveled nozzles using the

new Penn State methodology to create the beveled exit. Chapter 5 outlines the study to increase the understanding of the effect of interior nozzle corrugations. Both acoustic measurements and flow field visualizations will be shown. Chapter 6 examines the combination of the two noise reduction methods shown in the previous chapters. Acoustic measurements and flow visualization will be used to describe the effects of the combination. Finally, Chapter 7 will offer conclusions from the experimental results and present possible avenues for future work to take.

Chapter 2

Facility Description

2.1 High Speed Jet Noise Facility at the Pennsylvania State University

The Pennsylvania State University high speed jet noise facility was used for all of the experiments presented in the following study. The facility allows the use of several different experimental techniques to be used on air jets exhausting from a plenum into an anechoic chamber. The facility is located within rooms 26 and 30 of the Hammond Building in University Park, PA. The anechoic chamber walls, floor and ceiling are covered with fiberglass wedges which results in wedge-wedge dimensions of 5.02 x 6.04 x 2.79 m (16.5 x 19.82 x 9.15 ft). This produces a theoretical cut-off frequency of 250 *Hz*. During experiments the facility pressure, temperature, and humidity are each measured using a barometer, thermometer, and hydrometer, respectively, which are mounted within the chamber. A schematic and photograph of the facility can be seen in Figure 2.1. The current chamber is a result of a series of a facility upgrades that began in 1999 and mostly concluded in 2008. An overview of the facility and it's operation will be included, but more detailed descriptions and design can be found in previous Penn State Ph.D. theses by Doty [46] , Kuo [36] and Veltin [47].

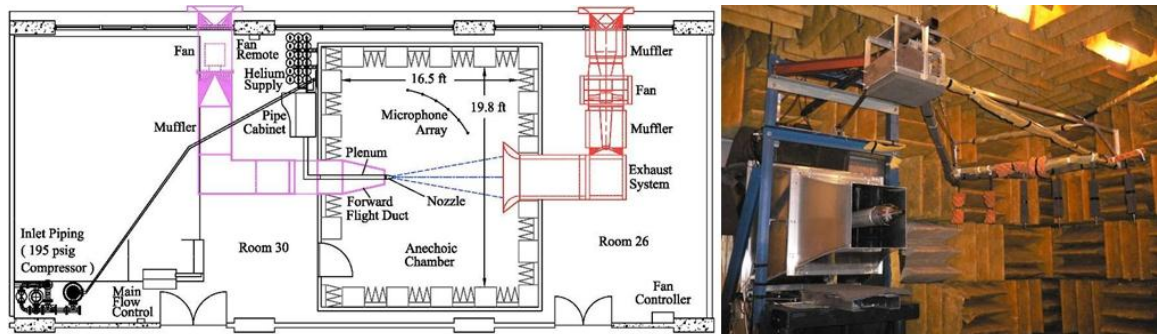


Figure 2.1: Schematic and Photograph of the Pennsylvania State University High Speed Jet Noise Facility

The air for the facility is supplied by a CS-121 compressor combined with a KAD-370 air dryer, both of which were manufactured by *Kaeser Compressors*. The compressor fills a 56.6 m^3 reservoir tank with a maximum gauge pressure of 1.34 MPa (195 psig) which then supplies the air for the piping system.

As temperature ratio is an important parameter for these studies, this facility uses helium-air mixtures to simulate the high temperature of aircraft engine exhaust jets. This mixture has been shown by Kinzie and McLaughlin [48] to accurately reproduce the acoustic properties of conventionally heated jets and its methodology and procedures will be discussed in more detail in section 2.2. The helium supply for the facility is provided by helium bottles. Up to six bottles, each initially at 13.8 MPa (2000 psig), can be equipped at one time.

The air and helium flow is controlled using a series of pressure regulators and control valves located within a piping cabinet near the workstation. The air flow exiting the piping cabinet enters the high pressure plenum which is a 1.83 m (6 ft) long aluminum pipe with a 11.43 cm (4.5 in) inside diameter. Upon entering the plenum the air passes through a 12.7 cm (5 in) long conical section of perforated plate and 7.62 cm (3 in) of honeycomb which reduce turbulence intensity levels and increase the mixing to allow for adequate mixtures of the helium and air. A pitot probe is then embedded in the middle section of the plenum which, via a calibrated pressure transducer, provides the total pressure upstream of the exhaust jets. The end of the plenum was designed in such way that different geometry jet nozzles can be easily attached and tested. These nozzles are typically fabricated quickly and cheaply using computer-aided design and rapid prototyping techniques.

Typical exhaust nozzle sizes range from diameters of 12.7 mm (0.5 inches) to 25.4 mm (1 inch). The high pressure air supply previously described allows for pure air exhaust jets with maximum jet Mach numbers of 2.3 and 1.7, respectively, for the range of nozzle sizes.

Furthermore, exhaust jets of $M_j = 1.5$ can be continuously and stably supplied for 50 minutes and 7 minutes, respectively.

The facility also includes two additional fans, the first of which is a *Twin City Mixed Flow* fan, model QSL 270. This fan produces flow which exhausts from a 0.381 m (15 in) square duct around the jet plenum. The inlet fan is used for forward flight simulation during experiments, which will be described in more detail in section 2.3. The second fan, a *Buffalo* vane-axial exhaust fan model 38A9, is connected to an exhaust collector on the far side of the anechoic chamber. The exhaust fan serves two purposes. First, the exhaust fan minimizes any possible helium accumulation inside the anechoic chamber. Second, it draws the jet plume from the inlet fan out of the chamber which allows the forward flight capability to reach higher speeds while maintaining a constant chamber pressure.

Acoustic measurements are currently performed using six microphones, each of which is supported by a boom that extends from the plenum stand, which can also be seen in in Figure 2.1. The microphone array can be freely rotated around a point located at the center of the nozzle exit plane. The microphones are positioned so that the ends are at a grazing incidence to the centerline of the jet exhaust and are equally spaced every 10° from the jet axis. The average physical radial distance of all the microphones to the nozzle exit is 1.78 meters. When testing jet nozzles smaller than an 2 cm in diameter this allows for the microphones to be considered in the acoustic far field. Because the microphones are assumed to be located in the acoustic far field, spherical spreading can be applied to the data to propagate the values to different (far-field) radial positions.

2.2 The Use of Helium for Heat-Simulated Supersonic Jets

The facility uses helium-air jet mixtures to simulate heated air jets. The methodology was demonstrated and developed over ten years ago by Doty and McLaughlin [49]. Heated jets have a lowered density and an increased acoustic velocity (for a given pressure ratio between the plenum total pressure and ambient pressure), and both of these features can be achieved through helium-air mixture jets. Kinzie and McLaughlin [48] have demonstrated that the mixture of helium and air is able to capture the dominant noise characteristics of actual heated jets. Doty and McLaughlin [49] and Papamoschou [50] have shown that mixtures of helium and air can appropriately simulate the noise of heated jets to a reasonable accuracy by matching the acoustic velocity of the heated gas. Miller and Veltin [51] presented a good agreement of the flow properties between the experimental data from helium-air mixture jets and the numerical calculation of heated air jets. Additionally, a comparison was made between experimental data from the laboratory helium-air jet noise facility at Penn State and the moderate scaled heated jet noise facility at NASA Glenn Research Center. McLaughlin, Bridges, and Kuo [30] documented how the acoustic data measured in the two facilities compare with very good engineering accuracy.

Helium gas has a lower density and a higher gas constant than pure air. This allows mixtures of air and helium to simulate the two parameters which are altered by heating the jet, lowered density and increased acoustic velocity. However, both the acoustic velocity, a , and the density of the jet, ρ_j , cannot be precisely matched at the same time. Therefore two different matching methods exist and were presented by Doty and McLaughlin [49]. Acoustically, the discrepancy between the two methods has been shown to be within 1 *dB* across both the frequency range in narrowband spectra and in *OASPL* levels. For experimental consistency the acoustic velocity matching method was selected.

The acoustic velocity matching method simply matches the acoustic velocity of the desired heated jet condition to the acoustic velocity of a helium-air mixture.

$$a_{heated} = \sqrt{\gamma R_{gas} T_j} \xrightarrow{\text{yields}} a_{mix} = \sqrt{\gamma_{mix} R_{gas,mix} T_{j,mix}} \quad 2.5$$

Both the gas constant and specific heat ratio are constant for pure air, so the desired jet temperature, T_j , is selected to produce a desired acoustic velocity, a_{heated} . Then that is set equal to the mixture acoustic velocity, a_{mix} . Since the jet mixture temperature, $T_{j,mix}$, can be calculated using the stagnation temperature (typically standard atmosphere) and jet temperature ratio (found using isentropic relations), then the only unknowns to make the two acoustic velocities equal are the mixture gas constant, $R_{gas,mix}$, and the mixture specific heat ratio, γ_{mix} . Both the mixture gas constant and the mixture specific heat ratio are dependent upon the helium concentration within the mixture. Therefore the desired molar mass ratio between the pure air and helium can be calculated such that the acoustic velocity of the heated and desired mixture case match. Then the molar mass ratio can be used to find desired partial pressures of both the helium and the air. The partial pressures of both the helium and air are then regulated in the piping cabinet to produce the desired jet condition.

2.3 Forward Flight Simulation

The forward flight stream generates a co-flow around the nozzle which simulates the ambient air conditions while an aircraft is moving, specifically during takeoff and landing. Some measurements were conducted with the forward flight stream on in addition to the supersonic jet through the nozzle. The inlet fan pulls through a muffler and acoustically treated 0.91 meter (36 inch) square duct from the outside of the building. The duct goes through three ninety degree turns to reduce the amount of fan noise that is propagated to the anechoic chamber. Once the air

ducts enter the chamber there is a contraction section which ends with a 0.38 m (15 inch) square duct located 0.30 m (12 inches) from the nozzle exit. Corner fillets are present in the contraction section to reduce the presence of vortices that would contaminate acoustic measurements and alter the mixing layer of the forward flight stream. The inlet duct can be seen in Figure 2.1. By using both the inlet fan and the exhaust fan simultaneously, the co-flow forward flight stream can reach speeds of 57.91 m/s (190 ft/s), or a forward flight Mach number, M_f , of 0.17.

The noise produced by the supersonic jet is affected by the existence of the forward flight stream. The effect on the noise and how to correct the results because of the existence of the outer shear layer are described in detail by Viswanathan and Czech [52]. The specific equations and processing methodology used for correction in the Penn State Facility is described by Veltin, Day and McLaughlin [53]. For these results, all noise frequencies were assumed to be produced at the exit plane. This is obviously imperfect, but provides a practical method to obtain an acceptable accuracy for the correction. The data shown for the forward flight case have been corrected for the forward flight stream shear layer refraction to produce data that would be measured in a forward flight stream wind tunnel of larger size than the distance from the jet to the observer microphones, such as if an observer was moving with the nozzle. For the forward flight measurements, two additional microphone boom angles were used to allow for raw data ranging from $\theta=20^\circ$ to $\theta=130^\circ$ in increments of 5° . This allows for a more accurate interpolation of data during the correction for shear layer refraction.

Chapter 3

Experimental Setup and Methodology

3.1 Data Acquisition

The facility has several different data acquisition types, two of which are used and presented in the following chapters, acoustic acquisition and schlieren and shadowgraph imagery. Both of the methods use a laboratory desktop PC running *Microsoft Windows XP* to acquire data. The imagery is acquired using one of two usb cameras and the accompanying software for the specific usb camera. The acoustic measurements are acquired using a 16-bit PCI-6123 *National Instruments* 8 channel DAQ.

The data acquisition can acquire 8 channels simultaneously. The typical channels acquired are six microphones located on the boom and the voltage from the pressure transducer which is attached to the pitot probe measuring upstream total pressure in the plenum. The data acquisition and storing is accomplished with *LabVIEW* software. The code *acquire_DAQmx_v002.vi* originally developed by Doty [46] is used within the *LabVIEW* software. The sampling rate is set at 300 kHz for the data acquisition and 204,800 or 409,600 data points are collected, the reduced data set being used for helium-air mixture jets in order to reduce the amount of helium used during an experiment.

3.2 Acoustic Measurements

The microphones are all 1/8" pressure-field microphones of type 4138 from *Brüel and Kjaer* (B&K), and type 40DP from *GRAS*. Following calibration corrections the acoustic data have a frequency response reliably accurate to 120 kHz. This is adequate to analyze all

predominant frequencies important to jet noise at this small scale for supersonic exhaust jets. Each acoustic measurement was performed with the microphone boom in at least two locations which allows for data from $\theta=20^\circ$ to $\theta=130^\circ$ (measured from the jet downstream direction originated from the nozzle exit plane) in increments of 10° . The microphone calibration is performed with a *B&K* acoustic calibrator, model 4231, and the microphone calibration constants are recorded to provide the conversion from the measured voltages to the equivalent pressure. The analog time-domain signals from the microphones are routed through a *Nexus*, *B&K* signal conditioner or a *GRAS* model 12AN power module, and then amplified and filtered for antialiasing thus enabling their accurate digital conversion in the following data processing. A high-pass filter is also set to 500 Hz, removing any undesirable low frequency noise that could contaminate the data. Then the data is routed through an Analog to Digital Converter board and acquired using the *LabVIEW* software already described. Then the data is imported into *Matlab* for further processing and plotting functions. The flow chart of this acquisition process can be seen in Figure 3.1.

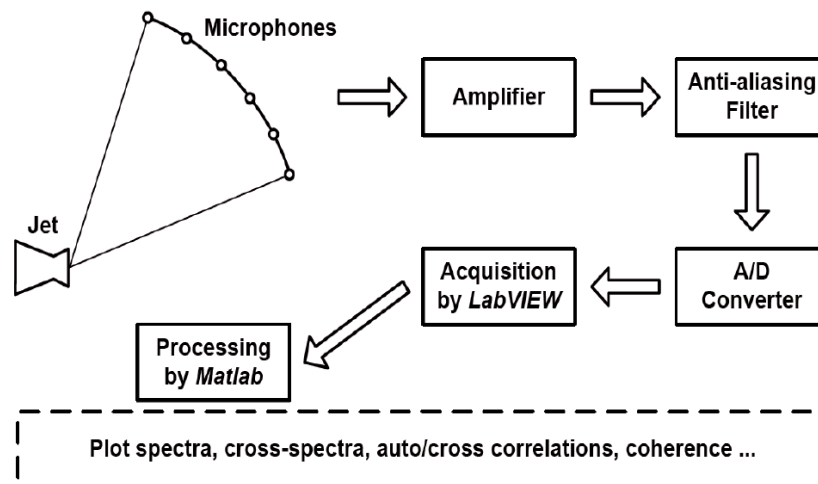


Figure 3.1: Flow Chart of the Data Acquisition Process

Once imported into *Matlab* the raw data are sequentially split into 4096 point segments and a Hanning window function is applied with 50 percent overlap between each window. The Fast Fourier Transform (*FFT*) is calculated in each window and the value is averaged from the 199 segments (or 99 segments for helium). This yields the power spectral density (*PSD*) with a narrowband bandwidth of 74 *Hz* which is then converted to decibels (*dB*) using a reference pressure of 20 μPa .

Three corrections are then applied to the raw sound pressure level (*SPL*) to compute the lossless *SPL* as explained in Kuo, Veltin, and McLaughlin [29]. Data were corrected for microphone spectral response characteristics based on the manufacturer's descriptions of each individual microphone obtained during the factory actuator calibration ($\Delta C_{act}(f)$) including the appropriate free field response ($\Delta C_{ff}(f)$). The spectra were also corrected for the daily variations in atmospheric attenuation by calculating the attenuation (ISO 9613-2:1996) for each microphone using measured ambient pressures, humidities, and temperatures ($\Delta C_{atm}(f)$) and adding back the sound lost due to the atmospheric attenuation from the jet to the microphone. Finally, the spectra are then non-dimensionalized to *PSD* per unit Strouhal number. Equation 3.1 summarizes the different steps that lead to the *PSD* per unit Strouhal number as explained in Kuo *et al.* [29].

$$PSD(St) = PSD_{raw}(f) - \Delta C_{act}(f) - \Delta C_{ff}(f) + C_{am}(f) + 10 \log_{10} f_c \quad 3.1$$

The experimental data were processed into non-dimensionalized lossless acoustic spectra to allow for easier comparison to acoustic spectra from larger model scales and full scale jets. Most measurements were made at distances close to $R_{raw} = 100$ jet diameters. Following processing, the resulting data were (back) propagated to an exact radius of 100 jet diameters (assuming spherical spreading of the acoustic field). This “back” propagated *PSD* is determined from Equation 3.2.

$$PSD(St) = PSD(St) + 20 \log_{10} \left(\frac{R_{raw}}{R} \right) \quad 3.2$$

From the *SPL*, given at intervals of Δf , the *OASPL* is calculated from the following formula:

$$OASPL = 10 \log_{10} \left[\Delta f \sum 10^{\left(\frac{SPL(f)}{10}\right)} \right] = 10 \log_{10} \left[\Delta St \sum 10^{\left(\frac{SPL(St)}{10}\right)} \right] \quad 3.3$$

3.3 Schlieren and Shadowgraph Setup

Shadowgraphy is a light refraction technique which can be related to the strength of the gradient of the density field within the flow. The schlieren technique is the nearly the same, with the addition of a knife edge at the refocusing point of the return beam shown in Figure 3.2. Schlieren imagery is proportional to the first derivative of density, while shadowgraph is proportional to the second derivative. Shadowgraph is best for visualizing shock waves, and schlieren gives added contrast and sensitivity to smaller changes within the flow allowing more acoustic and Mach wave radiation to be visualized, as described by Settles [54].

3.3.1 Overview

All shadowgraph and schlieren images shown were taken using a z-type setup and a strobe light as the light source. The z-type setup has the light focused to a point source using a lens and slit, and is then directed towards a parabolic mirror which produces parallel light. The light passes through the desired test section and encounters another parabolic mirror which focuses the light to a point. If using the schlieren technique, a horizontal knife edge is placed at the point, and cuts the point of light in half. This causes portions of the flow which have density gradients that deflect the light downwards to be blocked by the knife edge and thus show up darker on the image, with the opposite also being true. A camera is setup after the point source to

acquire the light. The mirrors used in this facility are 6 inch mirrors with a 48 inch focal length. A schematic of this z-type setup can be seen in Figure 3.2.

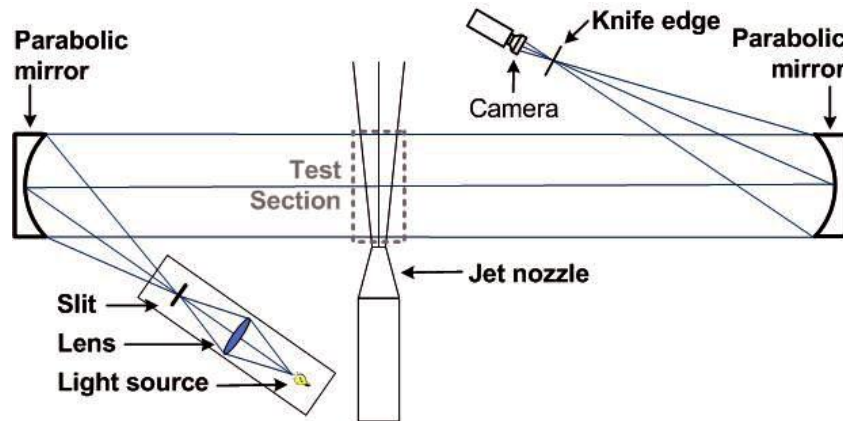


Figure 3.2: Schlieren/Shadowgraph Z-type Setup used in the High Speed Jet Noise Facility at the Pennsylvania State University

The placement angles and positions of the lens, slit, mirrors, knife edge and camera is dependent upon many different lens equations as outlined by Settles [54]. When using a digital camera to acquire images it is necessary to separate the camera from the lens, thus allowing the distance between the back of the lens and the physical CCD surface to be controlled. Controlling this distance, along with the camera focal length and focus allows the optical image to be brought into very sharp focus. Settles [54] describes that when using the schlieren technique, the image should be in very precise focus. On the other hand when acquiring shadowgraph images the image should be brought into the same focus, and then taken slightly out of focus. This allows for the very finite and small flow perturbations (such as shock waves) to be more easily seen and visualized in the image.

It should be pointed out that the schlieren and shadowgraph technique is an integration effect of the entire path of light, so that you see an integration of the perpendicular density

gradients (to the system light beam), and not just one plane within the jet, and is thus somewhat three dimensional for exhaust jet flows.

While the helium-air mixtures reproduce the flow properties and acoustic properties of the exhaust jets very adequately, the optical qualities are greatly changed. The refraction index of helium is significantly higher than air, so this causes helium-air mixture shadowgraph and schlieren images to be very sensitive. When imaging simulated high temperature ratios the inside of the jet is completely obscured by the highly turbulent helium-air mixture in the shear layer. For this reason most of the schlieren and shadowgraph images presented are of pure air, $TTR = 1$ jets. However, it will be shown that small percentages of helium, such as exists at very low total temperature ratios such as $TTR = 1.2$, can increase the technique's sensitivity and produce very clear images.

3.3.2 Image Acquisition and Equipment Settings

An upgrade to the digital camera was performed during the process of conducting the present research. The original camera was a black and white CCD camera model 109B made by *Safety & Security*. This camera had a listed frame rate of 50 *fps* (interlaced) while acquiring video with a 320 x 240 pixel resolution. The new camera was purchased from *Mightex Systems* and is a Buffered 3 Megapixel color CMOS camera. This camera, with accompanying software, allows control of the resolution and frame rate acquired as long as the combination doesn't exceed the max bitrate, ~300 MB/s, of the camera. Typical settings used were a resolution of 1368 x 1368 pixels with an exposure time of 100 *ms* and a corresponding frame rate of 10 *fps* (progressive). A comparison of shadowgraph images taken by the two cameras at nearly the same condition and nozzle is shown in Figure 3.3. The two images have been cropped to be the same size and show the same area of the flow. It is immediately apparent that the new *Mightex* camera allows for a

much greater amount of detail to be seen. The old camera produced images which were very pixelated and did not use very many levels of gray. The new camera has a much higher contrast and shows much more detail in the flow field.

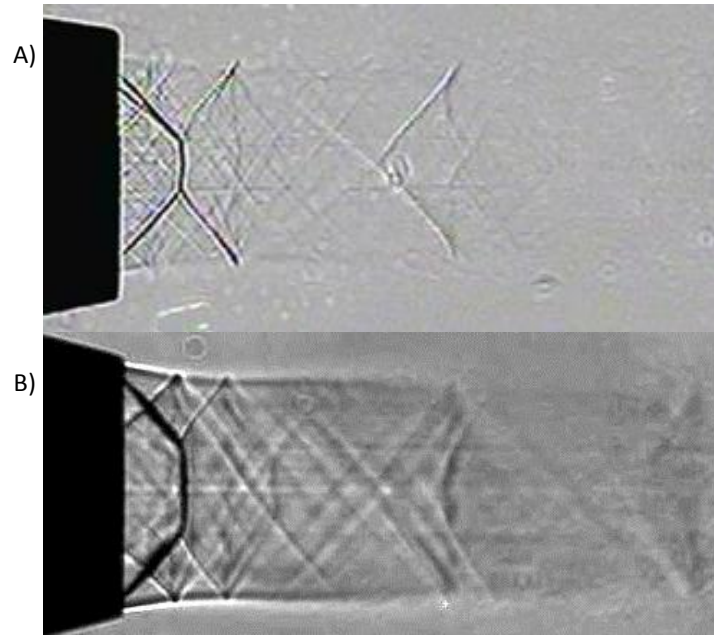


Figure 3.3: Comparison between the A) Old Low Resolution Camera, and the B) New High Resolution Mightex Camera at a similar jet condition.

The light source used for this z-type setup is a short duration spark light with a xenon lamp, specifically Spectralite Model 900 manufactured by Spectrum Dynamics. The strobe light power supply allows for external inputs to be used to force the timing of the spark flashes. Therefore the sparks per second of the strobe light can be controlled using an Agilent model 33220A signal generator.

The ability to control the camera frame rate and strobe light sparks per second, along with the digital camera gain allows for different image types to be obtained, all with adequate brightness and contrast levels. The number of optical averages of an image is the number of spark flashes during the exposure time. For example, if the camera exposure time is set to 100 *ms* with a frame rate of 10 *fps* and the strobe light frequency is set to 10 *sps* the number of optical averages

is 1. Whereas if the frame rate is set to 20 *fps* with a strobe light frequency of 60 *sps* the number of optical averages is 3.

Along with the ability to manage the optical settings prior to image acquisition, the images are imported into *Matlab* for post processing. The post processing involves two steps. First, each image has a “No-Flow” image subtracted to remove most of the imperfections from dust and or dirt on the lenses and or mirrors. Along with the “No-Flow” subtraction, the image histogram is edited to further improve the brightness and contrast. The second step involved is a digital averaging of the schlieren or shadowgraph images. For each experimental test, the flow is maintained at the desired jet condition for a length of time, ranging from fractions of a second (for helium-air mixtures) to 5-10 seconds for pure air. The result is that the digital camera produces a large number of frames at the specified jet condition. These frames can then be each digitally averaged together to obtain an average condition for the flow field. The number of digital averages is the number of frames that were averaged using *Matlab* post-processing.

A comparison of several different imaging techniques used throughout this research is shown in Figure 3.4. The three images shown are all for jets exhausting from the same nozzle at nearly identical nozzle pressure ratios. Image A and B are shadowgraph images of pure air jets with a $TTR = 1$, while image C is a schlieren image of a helium-air mixture jet with a $TTR = 1.2$. Image A has 1 optical average and 1 digital average; image B has 1 optical average and ~100 digital averages; image C has 10 optical averages and 6 digital averages. Low amounts of averaging (digital and optical) show the turbulent structure of the jet and let you see the shear layer clearly. By increasing the number of averages, the shock cell structure becomes very clear. The addition of low amounts of helium can be seen to increase the contrast and depth of the image. Both the size and shape of the shear layer and the shock cell structure are very clear. The only downside is that the helium experiments are more difficult to perform and more time consuming to process.

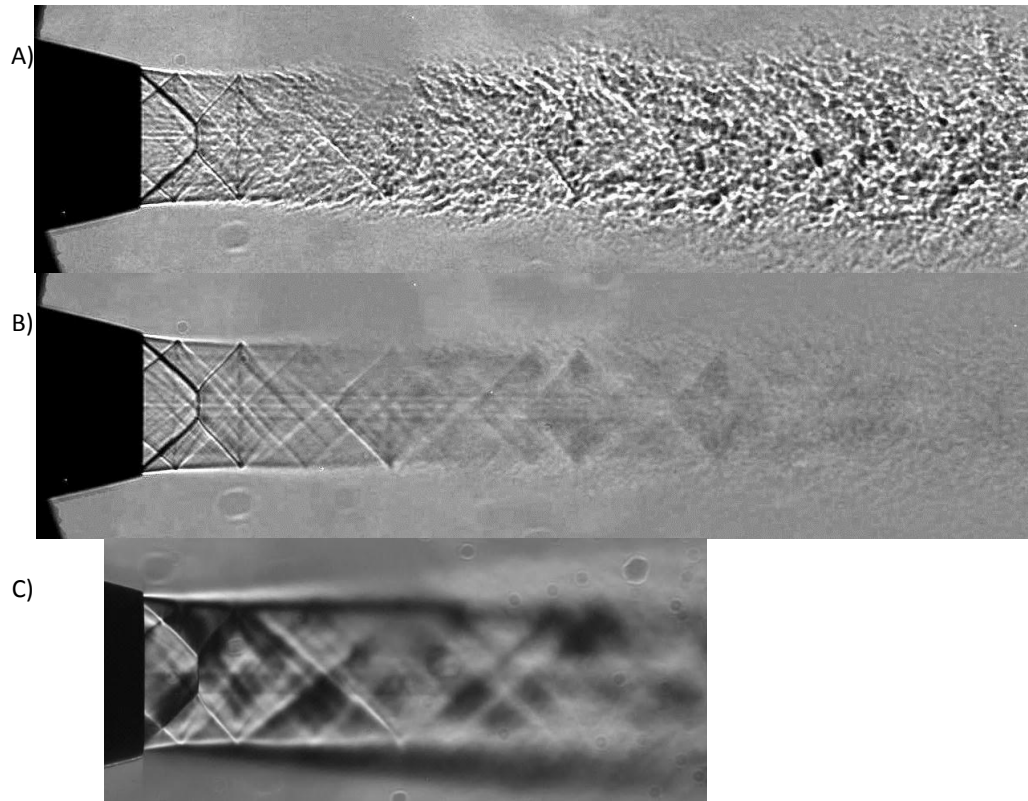


Figure 3.4: Image Comparison between three different techniques of Schlieren and Shadowgraph at the same nozzle pressure ratio. A) Instantaneous Shadowgraph Image, $TTR = 1$. B) Digitally Averaged Shadowgraph Image, $TTR = 1$. C) Optically Averaged Schlieren Image, $TTR = 1.2$

3.4 Model Geometry of Military-Style Supersonic Converging-Diverging Nozzles

The results presented in this study were conducted with military style nozzles representative of aircraft engines of the F404 (used in the F-18 aircraft) family. The exact inner contours of the military style nozzles were provided by General Electric Aviation under a previous contract for the Strategic Environmental Research and Development Program (SERDP). Such military engines have nozzles which are capable of varying the geometry to produce different exit to throat area ratios to adapt for different flight regimes. The expansion portion of these nozzles contains a flap and seal configuration which consists of 12 flat segments that are

interleaved to facilitate area adjustment of the operational nozzles. For this research, one exit to throat area ratio was selected at a typical configuration for a takeoff scenario of one of these aircraft. The area ratio selected was 1.295, which results in a design Mach number of 1.65. These nozzles were then designed with the same multi-faceted (12 segments) inside conical contour, and have an exit diameter of 1.8 cm (0.708 inches). More detail about these military style supersonic nozzles can be found in Kuo, Veltin, and McLaughlin [28] and McLaughlin, Bridges, and Kuo [30]. The nozzles were manufactured using several different rapid prototyping techniques, each having different layering thicknesses, producing different a surface roughness. The three techniques vary in accuracy and were chosen depending on the priority and needed accuracy for the specific nozzle. The three techniques and their corresponding standard layer thicknesses are: fused deposition modeling (FDM) with ABS plastic, 0.254 mm (0.01 in.), HDSL (high-definition Stereolithography with SC-5500 material, 0.127 mm (0.005 in), and PolyJet HD with the Polyjet Gray material, 0.015mm (0.0006 in). The first time a nozzle is introduced in this paper, it will be followed by the manufacturing method in parenthesis.

The beveled nozzle is a nozzle which has the exit plane rotated at an oblique angle to the flow instead of perpendicular. For a supersonic converging-diverging nozzle, there are many ways which a bevel could be added to the end of the nozzle. The methodology created and used for this study was to rotate the exit plane with the center of rotation at the center of the exit plane. This extends the bottom lip of the nozzle and shortens the top of the nozzle. This method was decided upon because it results in a projected area ratio (exit area perpendicular to the flow) of the bevel exit which is closest to the baseline area ratio. For the angles used the percent change in perpendicular exit area was less than 0.3%. There were two beveled nozzles used in this study, a military-style nozzle with a 24° exit plane rotation, Md1.65 Bevel24 (FDM), and a military style nozzle with a 35° exit plane rotation, Md1.65 Bevel35 (FDM). A two-dimensional cross section drawing of this methodology can be seen in Figure 3.5, as well as an image of the actual rapid-

prototyped nozzles. For these beveled nozzles the azimuthal angle, ϕ , was taken to be 0° on the long lip side and 180° on the short lip side.

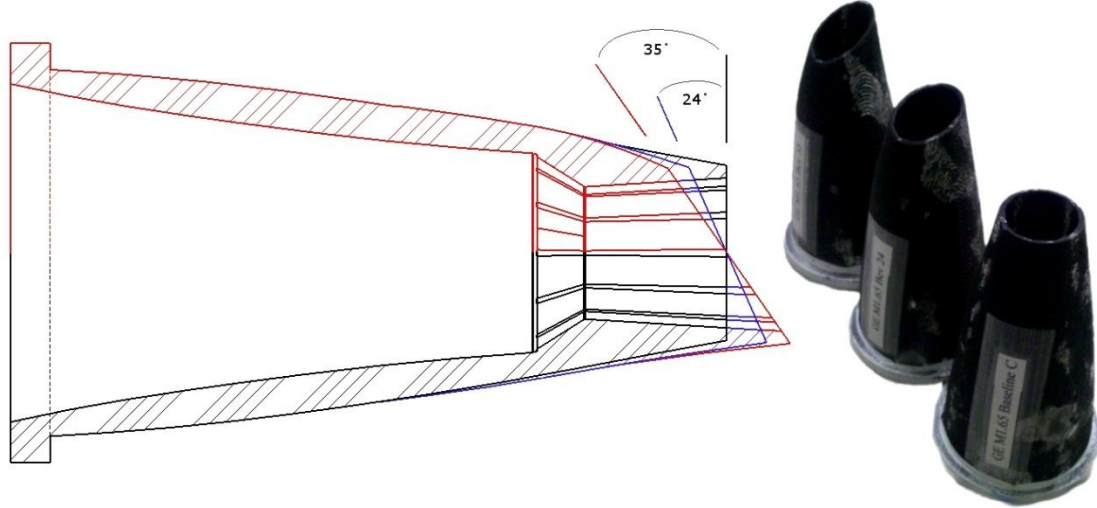


Figure 3.5: The Beveled Nozzles – Left: 2-D Cross-Sectional Drawing; Right: Image of Rapid Prototyped Nozzles

The hard wall corrugation nozzles are designed using the methodology and process briefly outlined by Seiner *et al.* [44] [55]. This process will be discussed in more detail in the following section. The final result of the corrugation design is a shape of a corrugation which is added to six of the twelve facets of the military style nozzle.

For this study several different nozzles were made. First the baseline nozzle was made (HDSL) with a jet design Mach number of 1.65. Then a nozzle was made from the hard wall corrugation design with only two of the corrugations (FDM) such that the corrugations are located on opposite facets. Next, a nozzle was made from the same corrugation design with three symmetric corrugations (FDM), such that they are equally spaced. Then the full corrugation design was used to create a nozzle with six corrugations (PolyJet HD). The nozzles with two and three corrugations were made so that the size and shape of the corrugations were the same as the six corrugation nozzle design, such that it was as if some corrugations were deleted or removed.

Finally, a nozzle was made that combined a 35 degree bevel on the jet exit centerline

with the six hard walled corrugation design (PolyJet HD). The corrugations on the long lip size of the nozzle were extended using the area as if the nozzle lip were not cut off. These five nozzles can be seen pictured in Figure 3.6, and will now be referred to as (in the order presented previously) Md1.65 Baseline, Md1.65 2Corrug, Md1.65 3Corrug, Md1.65 6Corrug, and Md1.65 6CorBev35. For the first four of these nozzles, the azimuthal angle, ϕ , was taken to be 0° when a corrugation was directly to the right, or facing the microphone boom array. For the Md1.65 6CorBev35 nozzle, the azimuthal angle was taken to be the same as for a purely beveled nozzle.



Figure 3.6: Image of the corrugation nozzles used in this study. From left to right, top row: Md1.65 Baseline, Md1.65 2Corrug, Md1.65 3Corrug. Bottom row: Md1.65 6Corrug, Md1.65 6CorBev35

3.5 Methodology for Creating the Corrugation Nozzle

The design of the corrugations starts with deciding on an optimal operating condition. The main point used by Seiner *et al.* [25], design point 8S, was a nozzle with a design Mach number of 1.64, with corrugations with a design point of nozzle pressure ratio 3.03 which results

in a jet Mach number equal to 1.37. For this study, all nozzles have a design Mach number of 1.65, and the design point chosen was a nozzle pressure ratio of 3.5 which results with an over-expanded jet of jet Mach number 1.47. However, because of the small scale and low Reynolds's numbers of this facility, we hypothesized that the boundary layers are larger in proportion to larger scale facilities. The effect of this on chevrons has been discussed and demonstrated using smooth and rough nozzle measurements with and without chevrons [40]. Therefore the most productive results were expected to be similar to those conditions run by Seiner *et al.* [44] [25]. These corrugations have been redesigned from the beginning to be used in the Penn State nozzles; the designs are outlined in the following two sub sections.

3.5.1 Axisymmetric Method of Characteristics Design

An axisymmetric method of characteristic solution was performed to produce the optimal area for the design point at each axial location of the nozzle. The solution performed calculated the minimum length nozzle (MLN) so that the corrugation shape will be able to fit inside the fixed length military-style GE nozzle. Simply put, the method of characteristics calculates the wall shape of the nozzle so that all characteristics (Mach lines) do not reflect off of it. There are two methods for calculating the nozzle shape, first, using a straight sonic line MLN. The straight sonic line involves a straight sonic line between the throat and centered expansion which is generated by the sharp wall at the throat. The second is a curved sonic line which first uses a circular arc sonic line which is followed by a conical flow region, without a centered expansion. The method used for this study was a straight sonic line MLN calculated with a second order accurate method of characteristics solution as described by Argrow and Emanuel [56] and later implemented by Behara and Srinivasan [57]. The MOC equations for steady, supersonic, irrotational, axisymmetric flow are shown in Equations 3.4 and 3.5.

$$\frac{(M^2 - 1)^{1/2}}{1 + (\gamma - 1)M^2/2} \frac{dM}{M} \pm d\theta - \frac{\tan\theta}{(M^2 - 1)^{1/2} + \tan\theta} \frac{dx}{r} = 0 \quad 3.4$$

$$\frac{dr}{dx} = \tan \left[\theta \mp \sin^{-1} \left(\frac{1}{M} \right) \right] \quad 3.5$$

Where the top symbol in the shared operator is for right running (C-) characteristics and the bottom symbol is for left running (C+) characteristics. The variables used in these equations are given as, x and r and the axial and radial coordinates, θ is the flow inclination angle, M is the local Mach number and γ is the specific heat ratio.

The method of characteristics equations can be easily differentiated and solved for the needed parameters as outlined in Argrow and Emanuel [56], who also documented the sweep procedure for the grid. Once the computational method is setup there are several parameters which must be selected, the first of which is the number of characteristics. Increasing the number of characteristics increases the computation time and results in a more complex shape and precise nozzle. The even spacing of the characteristics in the expansion section at the wall contour results in an evenly spaced grid in the downstream portion of the nozzle, however it is very sparse near the throat. For this reason a grid compression scheme [56] was used to insert extra characteristics in the near throat region and increase the nozzle accuracy. The only other parameter which can be controlled is the initial wall expansion angle.

Therefore the procedure for determining a nozzle shape is to decide upon a number of characteristics, grid compression scheme, and the initial wall angle. The code is then run and results in a given nozzle shape and exit Mach number. Iterations must then be performed to find the correct initial deflection angle which results in the desired exit Mach number.

3.5.2 Corrugation Design

The corrugations are designed such that the effective cross sectional area (Baseline Area minus Corrugation Area) of the nozzle at any point matches the area of the perfectly designed contoured axisymmetric method of characteristics nozzle. Seiner *et al.* [44] showed that for these military style nozzles six corrugations is the optimal case, with each corrugation on alternating facets. The shape of each corrugation is a truncated super ellipse, with an aspect ratio between the height and width of two. The truncated super ellipse has a radial tangent at the ends which creates the smooth contour between the corrugation and the facet wall. At each axial location the height of one of the six corrugations is calculated from the equations for the area of all of the parts of the corrugation shape. The design of these corrugations can be seen in Figure 3.7.

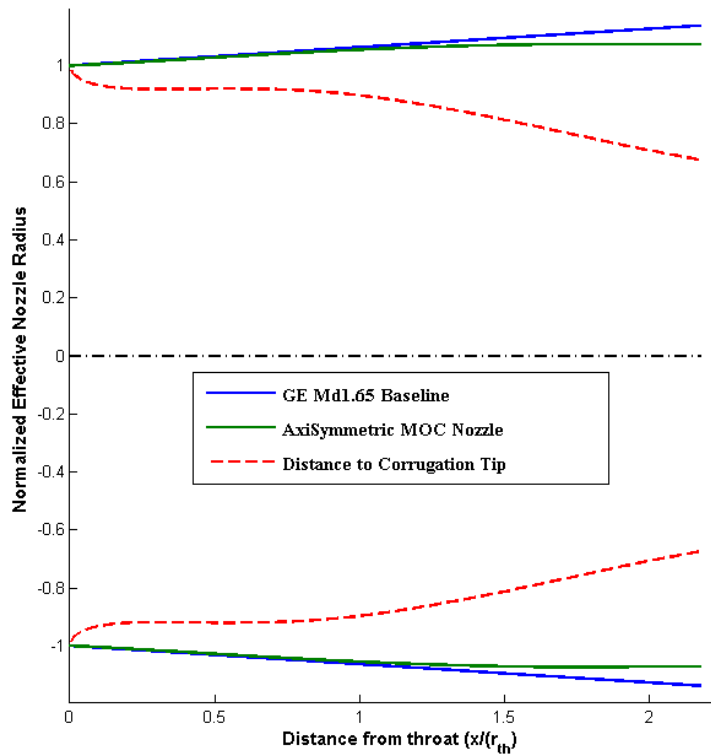


Figure 3.7: The Hard Walled Corrugation Design. Shown in the plot are the Normalized effective nozzle radius of the baseline nozzle (without corrugations) and the Method of Characteristics designed nozzle (baseline nozzle with corrugations). Also shown is the distance to the tip of the corrugation at each axial location.

The normalized effective radius of the baseline nozzle, along with the normalized effective radius of the MOC nozzle is shown for each axial location. Also plotted is the distance to the tip of the corrugation at each axial location.

The surface of the corrugations is then created using a sweep in the computer-aided design program, *Solidworks*. The corrugation shapes for the beveled nozzle are created by simply extending the nozzle areas as if there was no bevel cut plane. This is done by setting the MOC solution area at axial locations past the end of the nozzle to be equal to the area at the nozzle exit. The baseline nozzle area is extended by simply allowing the effective normalized nozzle radius to continue its linear relation with axial location. The 3D models used to create both the six corrugation nozzle and the six corrugation nozzle with the beveled exit plane (35 degrees) are shown in Figure 3.8.

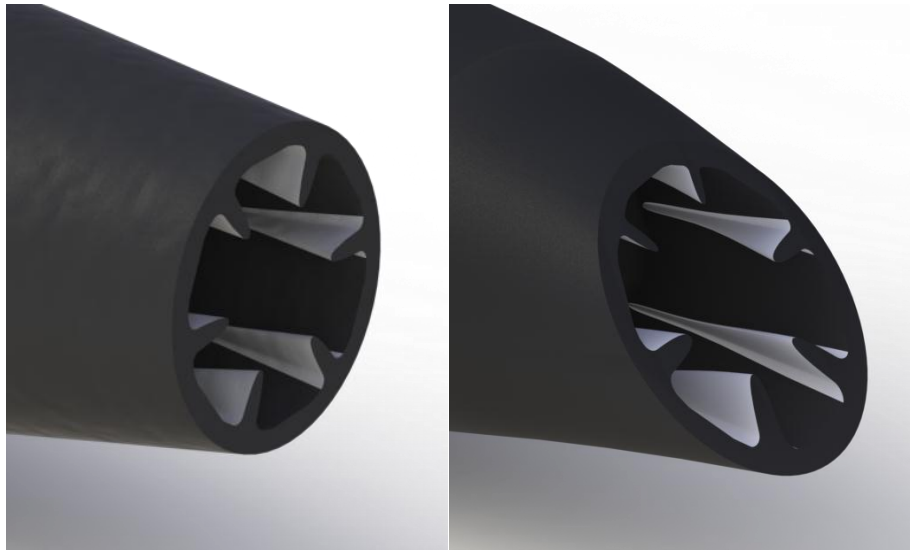


Figure 3.8: Computer-Aided Design Renders of the Military-Style Nozzle with Six Corrugations (Left), and Six Corrugations and a Beveled Exit Plane (Right)

Chapter 4

Examination of the Effects of the Beveled Exit Plane on a Supersonic Converging-Diverging Nozzle

4.1 Motivation and Review of Prior Work

In the past, studies have been performed on supersonic jets exhausting from a purely converging beveled nozzle [58]. Purely converging beveled nozzles have been shown to produce a significant deflection of the jet plume. It appeared that there was also an accompanying rotation of the acoustic field. A recent study by Viswanathan and Czech [43] documented the use of a bevel on a converging-diverging supersonic nozzle. Two different nozzle models were created with different area ratios and several different nozzle bevel angles, and all nozzles were tested at various different operating conditions. The method used to create the nozzle bevel resulted in effective area ratios which are less than the baseline nozzle, which has an effect on the flow field and the acoustic field.

Three main conclusions were drawn from the study by Viswanathan and Czech [43]. First, for supersonic converging diverging beveled nozzles the flow deflection is small, typically less than 1.5 degrees (measured by comparing the axial to perpendicular thrust), and it deflects towards the long lip for over-expanded jets while deflecting towards the short lip for under-expanded jets. Second, the axial thrust coefficient was seen to be at worst be the same as the baseline nozzle and sometimes have more thrust than the baseline. This was primarily attributed to the smaller effective area ratio of the nozzle. Finally, the beveled nozzle showed a maximum noise reduction of turbulent mixing noise in the direction of the long lip in the aft direction.

This study aims to extend these results with a slightly different methodology in the design of the nozzle bevel. For acoustic experiments, a large number of operating conditions, nozzle

azimuthal orientations and microphone positions were tested. Table 4.1 shows the matrix of these conditions. Accompanying schlieren and shadowgraph visualizations were made at similar conditions for comparison as well. Meaningful and relevant comparisons were drawn from these results in an attempt to draw out insight and major conclusions.

Table 4.1: Nozzle Parameters and Jet Conditions for Experiments

Nozzle	Jet Mach Number (M_j)	TTR	Polar Angle (ϑ) of 1 st Mic	Azimuthal Angle (ϕ)	M_f
Baseline	1.2 , 1.3 , ... , 2.1 , 2.2	1	20° , 80°	-	0
Bevel24	1.2 , 1.3 , ... , 2.1 , 2.2	1	20° , 80°	0° , 180°	0
Bevel35	1.2 , 1.3 , ... , 2.1 , 2.2	1	20° , 80°	0° , 180°	0
Bevel24	1.4 , 1.5 , 1.65 , 1.8 , 1.9	1	20° , 80°	45° , 90°	0
Bevel35	1.4 , 1.5 , 1.65 , 1.8 , 1.9	1	20° , 80°	45° , 90°	0
Baseline	1.47 , 1.64 , 1.77	3	20° , 80°	-	0
Bevel24	1.47 , 1.64 , 1.77	3	20° , 80°	0° , 45° , 90° , 180°	0
Bevel35	1.36 , 1.47 , 1.64 , 1.77	3	20° , 80°	0° , 45° , 90° , 180°	0
Baseline	1.47	1	20° , 25° , 80° , 85°	-	0.17
Bevel35	1.47	1	20° , 25° , 80° , 85°	0° , 45°	0.17
Baseline	1.47	3	20° , 25° , 80° , 85°	-	0.17
Bevel35	1.47	3	20° , 25° , 80° , 85°	0° , 45°	0.17

Notes:

- 1) In column 2, “1.2 , 1.3 , ... , 2.1 , 2.2” is an abbreviation for measurements at the jet Mach numbers of 1.2, 1.3, 1.4, 1.5, 1.6, 1.7, 1.8, 1.9, 2.0, 2.1, 2.2
- 2) Column 4 lists the polar angle of the first microphone on the boom which holds 6 microphones separated by 10 degrees. So 20° means microphones were located at 20°, 30°, 40°, 50°, 60°, and 70°.

4.2 Flow Field Analysis

Figure 4.1 contains the shadowgraph for both beveled nozzles and the baseline nozzle when over-expanded, nearly perfectly expanded, and under-expanded. The images shown in this Figure were of pure air, $TTR = 1$ jets, with 10 optical averages and about 75 digital averages each.

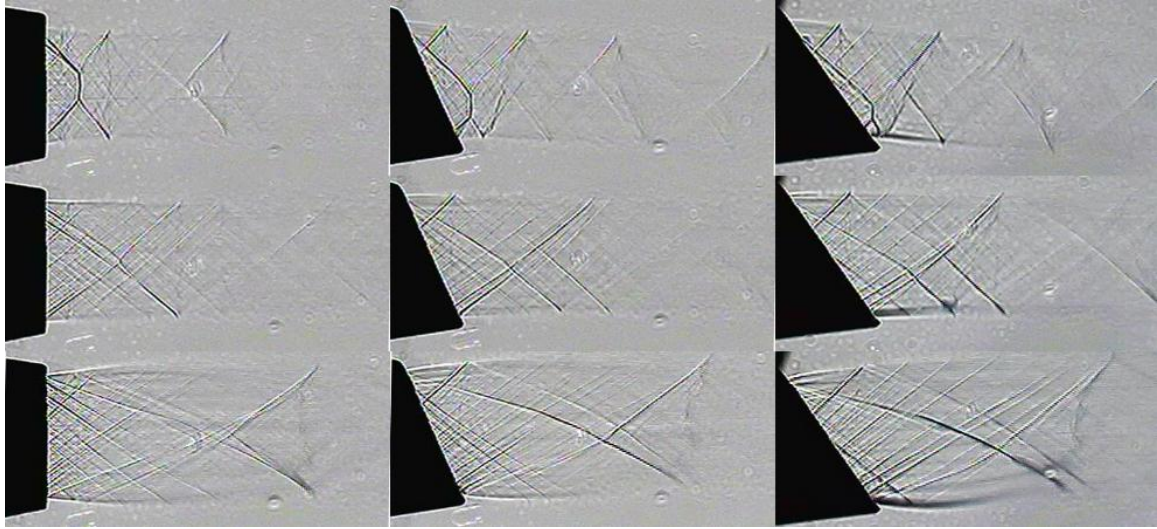


Figure 4.1: Shadowgraph Images – Top Row: $M_j = 1.4$; Center Row: $M_j = 1.6$; Bottom Row: $M_j = 1.9$ Left: **Baseline** Nozzle; Middle **Bevel24** Nozzle, Right: **Bevel35** Nozzle

For the baseline nozzle, the shock cell structure within the jet plume can clearly be seen for the over-expanded and under-expanded flow. As would be expected, the nearly perfectly expanded flow from the baseline nozzle shows only weak shocks, which result because the nozzle is a straight walled converging-diverging nozzle instead of a contoured converging-diverging nozzle designed to eliminate non-uniformities in the velocity at the nozzle exit.

The shadowgraph images of the beveled nozzles show how the flow changes because of the extension of the bottom lip, and the shortening of the top lip. The first thing that should be noticed is the deflection of the flow when compared to the baseline nozzle flow. The over-expanded flow ($M_j = 1.4$) is deflected towards the long lip side, with an average deflection of 3.4° for the Bevel24 nozzle and of 5.3° for the Bevel35 nozzle. On the other hand, the under-expanded

flow ($M_j = 1.9$) is deflected towards the short lip side, with an average deflection of 3.5° for the Bevel24 nozzle and of 5.77° for the Bevel35 nozzle.

The second thing to be seen is the change in the shock cell structure. Both the over-expanded and under-expanded flows show the shock cell shifting down towards the long lip. Additionally, the strength of the shock appears to increase as the bevel nozzle angle increases.

In addition to the cold jet shadowgraph images, schlieren images were also taken, this time with helium-air mixture jets. Figure 4.2 shows three schlieren images of the flow with helium-air being used to simulate a total temperature ratio, TTR , of 3.

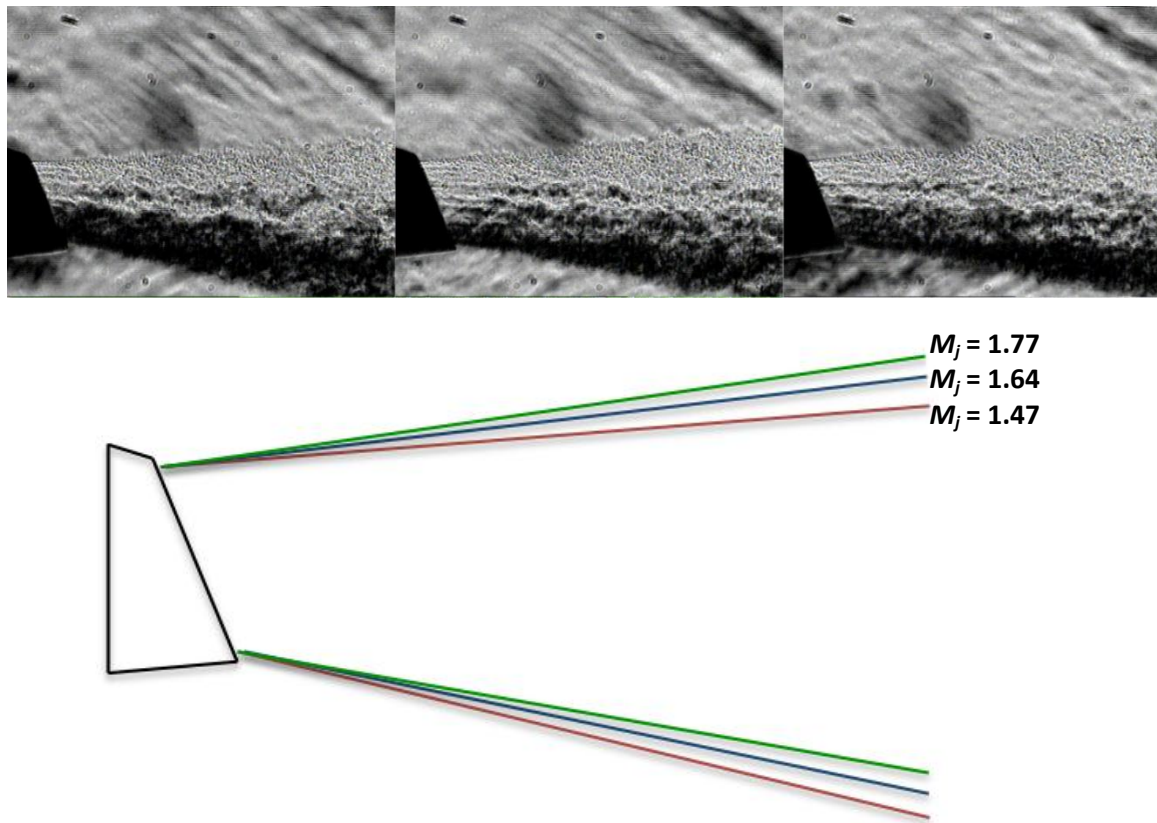


Figure 4.2: Top – Schlieren Imagery of the Bevel24 Nozzle with M_j (from Left to Right) = 1.47, 1.64, 1.77 Bottom – Comparison of the Flow Exit Angles at $M_j = 1.47, 1.64, 1.77$

These images have only 2 optical averages and 1 digital average. The strong Mach wave radiation can be seen for all three conditions. As discussed previously the internal structure of the

jet is obscured by the high turbulence and varying refraction index of the helium-air mixture. Also shown in Figure 4.2 is a schematic which compares the deflection angles for the three conditions, which can still be seen to be small angles.

4.3 Acoustic Results and Noise Reduction

Acoustic measurements were first taken with the baseline nozzle with no beveled exit, for a range of flow conditions. These measurements were followed with those made with beveled nozzles of two different bevel configurations. Each of the two nozzles were rotated to two azimuthal angles so the long lip of the nozzle was closest to the microphone array, then the nozzle was rotated 180° so the short lip was pointed towards the microphone array. The sound pressure level spectrum from all polar angles was then recorded for both of these configurations. Figure 4.3 shows the spectrum for five different polar angles emitted from the long lip side of the jet operating with a heat simulated over-expanded flow condition from all three nozzles. Below the spectrum is the variation in *OASPL* over a range of polar angles for all three nozzles. Figure 4.4 is similar, but shows the noise produced from the short lip side of the beveled nozzles. It can be seen that on the long lip side there is a reduction in peak emission noise of about 4 *dB* for the Bevel35 nozzle, with slightly less than that for the Bevel24 nozzle. There is very little noise reduction or gain in the *BBSAN*. On the short lip side, there is a slight increase in peak emission noise, with almost no change to the *BBSAN*. The *OASPL* comparison reinforces these conclusions for the noise on the long lip side, with noise reduction being seen in the low polar angles (20° - 50°) and similar noise levels for all other polar angles. The *OASPL* measured from the short lip side can be seen to be nearly identical to the baseline nozzle at most polar angles. However, at intermediate polar angles (60° - 80°) the noise emitted from the short lip side shows a slight reduction when compared to the baseline nozzle.

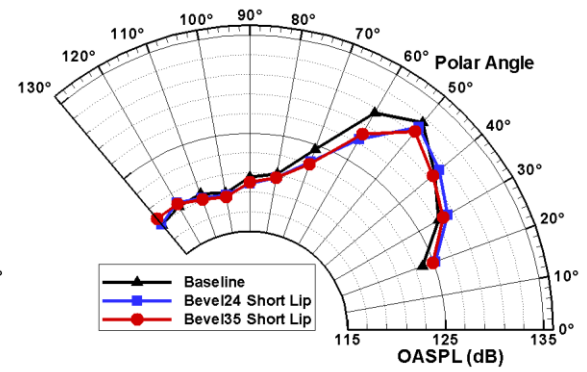
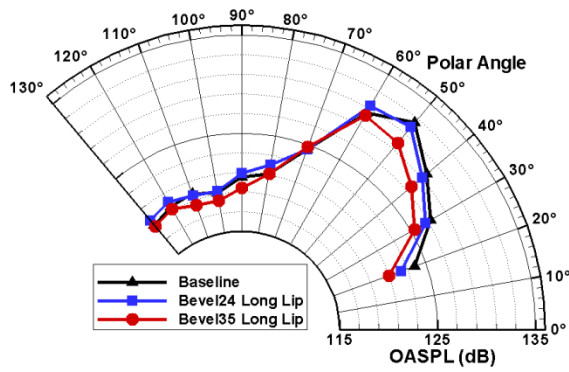
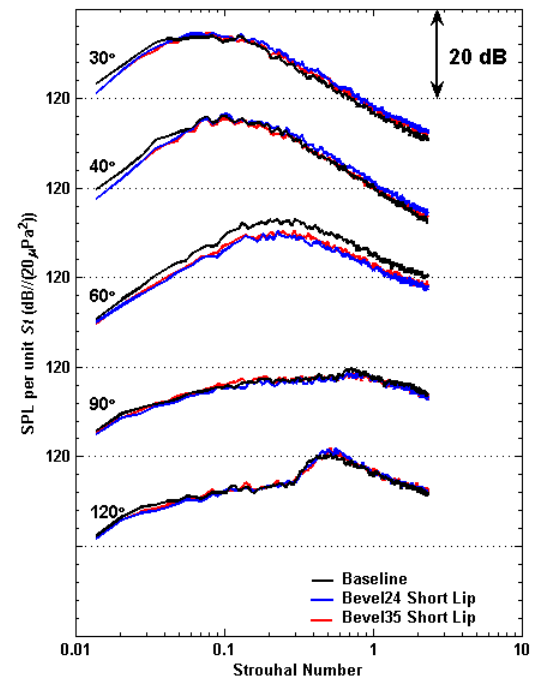
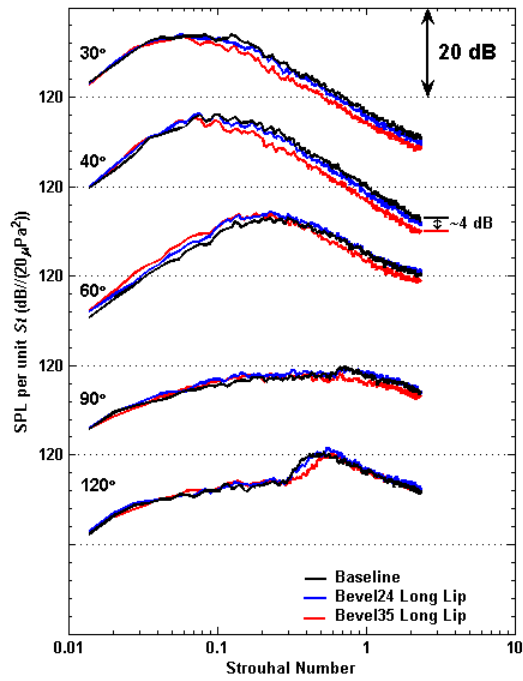


Figure 4.3: Spectra and OASPL Comparison of Heated jets, measured at $\phi = 0^\circ$ (Long Lip Side), issuing from $M_d = 1.65$ Beveled Nozzle, with $M_j = 1.47$, $TTR = 3$, $D_{noz} = 0.708''$, $f_c = 42693$ Hz, Scaled $R/D_j = 100$

Figure 4.4: Spectra and OASPL Comparison of Heated jets, measured at $\phi = 180^\circ$ (Short Lip Side), issuing from $M_d = 1.65$ Beveled Nozzle, with $M_j = 1.47$, $TTR = 3$, $D_{noz} = 0.708''$, $f_c = 42693$ Hz, Scaled $R/D_j = 100$

Figures 4.5 and 4.6 are similar to Figures 4.3 and 4.4, showing a nearly perfectly expanded jet condition instead of the over-expanded condition.

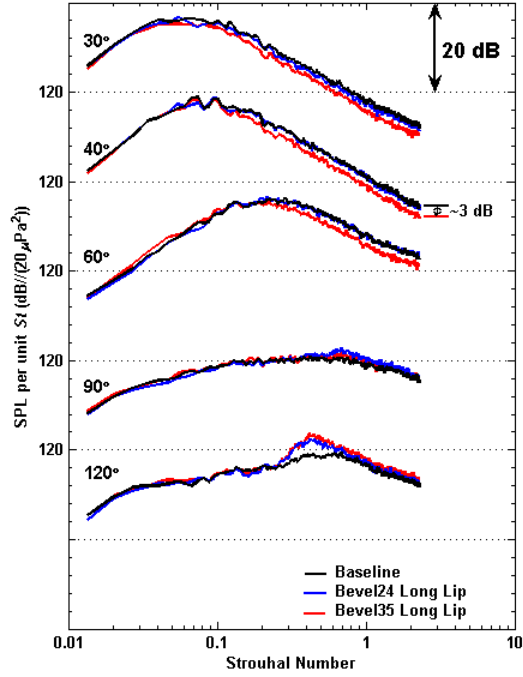


Figure 4.5: Spectra and OASPL Comparison of Heated jets, measured at $\phi = 0^\circ$ (Long Lip Side), issuing from $M_d = 1.65$ Beveled Nozzle, with $M_j = 1.64$, $TTR = 3$, $D_{noz} = 0.708''$, $f_c = 43644$ Hz, Scaled $R/D_j = 100$

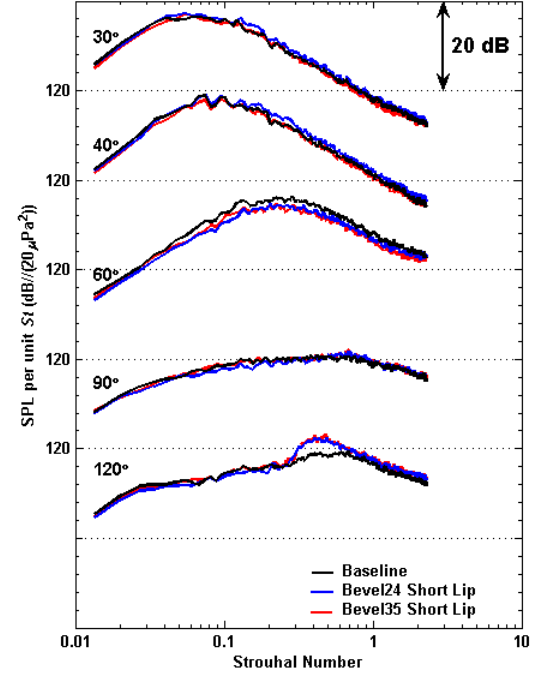


Figure 4.6: Spectra and OASPL Comparison of Heated jets, measured at $\phi = 180^\circ$ (Short Lip Side), issuing from $M_d = 1.65$ Beveled Nozzle, with $M_j = 1.64$, $TTR = 3$, $D_{noz} = 0.708''$, $f_c = 43644$ Hz, Scaled $R/D_j = 100$

It is noted that for noise issues the perfectly expanded pressure ratio condition is normally of much less importance than the over-expanded condition that occurs at take-off. It is included here to help complete the understanding of the noise generation physics.

For this perfectly balanced *NPR* case, a reduction of about 3 *dB* can be seen in the peak noise emission on the long lip side. On the short lip side, there is very little reduction or gain due to the beveled nozzle. When examining the forward polar angles it can be noticed that both beveled nozzles increase the peak *SPL* of the *BBSAN* by about 6-7 *dB*. This is expected following examination of the shadowgraph images in Figure 4.1 that showed stronger shocks in the nearly perfectly expanded flow issuing from the beveled nozzles.

Next, a more in depth azimuthal investigation on the noise field was conducted with measurements taken of the noise emitted with the nozzles at azimuthal orientations of 45° and 90°. In these cases the relevance of the higher degree azimuthal measurements is that if the nozzle is oriented long lip down during take-off, the quadrant containing the 45° to 90° direction most closely aligns with sideline microphones in aircraft noise certification and can still propagate to the ground. Figure 4.7 shows the comparison of a heat-simulated over-expanded condition between these two new azimuthal orientations with the baseline and the long lip side for reference. Only the Bevel35 nozzle is shown in this comparison. Both the spectra and the *OASPL* for all polar angles show that the noise produced at an angle of 45° is nearly identical to the baseline nozzle noise. The noise produced at an angle of 90° (directly in between the short and long lip) can be seen to be louder than the baseline nozzle. The magnitude of noise increase at 90° is similar to the magnitude of reduction seen on the long lip side. Figure 4.8 shows a comparison between the azimuthal orientations for the nearly perfectly expanded heat-simulated nozzle condition. The same trends as seen in the over-expanded case can be seen here with the addition of a noise gain at all azimuthal orientations in the upstream direction. This was previously noticed and believed to be due to the increasing strength of the shock cell structure when compared to the

jet exhausted from the baseline nozzle. The magnitude of reduction and gain for the perfectly expanded jet is slightly less than that of the over-expanded jet.

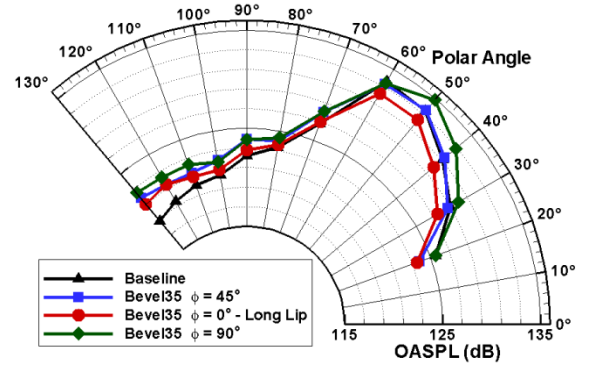
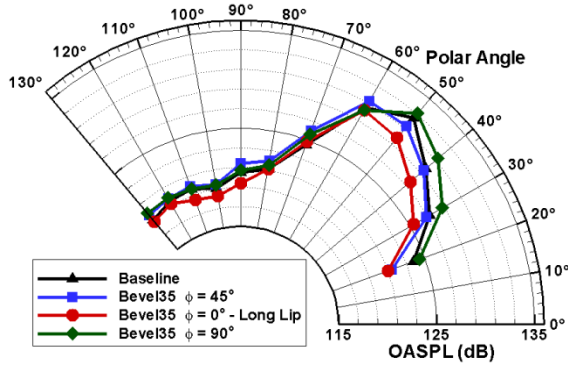
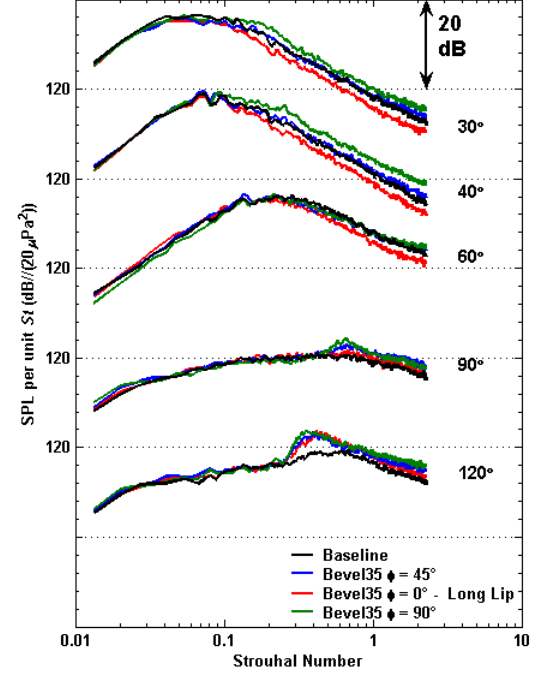
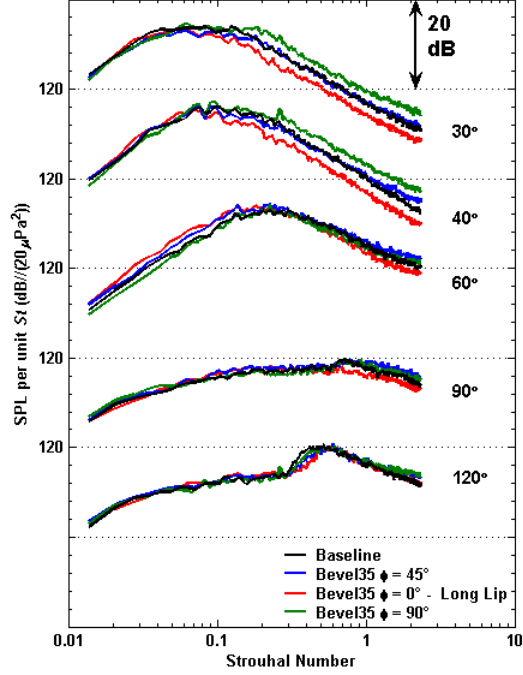


Figure 4.7: Spectra and OASPL Comparison of Heated jets issuing from $M_d = 1.65$ Beveled Nozzle, with $M_j = 1.47$, $TTR = 3$, $D_{noz} = 0.708''$, $f_c = 42693$ Hz, Scaled $R/D_j = 100$. The beveled nozzle jet data are shown for various azimuthal angles.

Figure 4.8: Spectra and OASPL Comparison of Heated jets issuing from $M_d = 1.65$ Beveled Nozzle, with $M_j = 1.64$, $TTR = 3$, $D_{noz} = 0.708''$, $f_c = 43644$ Hz, Scaled $R/D_j = 100$, again at various azimuthal angles.

Figure 4.9 again shows an azimuthal comparison between the baseline nozzle and the Bevel35 nozzle. A comparison at a more highly over-expanded jet Mach number of 1.36 is shown to emphasize the differences between the noise emitted from the short lip and the long lip of the beveled nozzle. At the low polar angles the noise emitted from the jet in the direction of the long lip ($\phi = 0^\circ$) is much less than the noise from the short lip ($\phi = 180^\circ$). We can see however, that the noise in the direction of the short lip is reduced more at the intermediate polar angles of 60° - 90° . By comparing the previous figures at the other over-expanded and the perfectly expanded condition, this trend at the intermediate polar angles can also be seen.

As already explored briefly, at azimuthal angles in between the short lip and the long lip, the noise reduction benefits are not always as pronounced. To illustrate this, Figure 4.10 shows the delta OASPL when compared to the baseline for the beveled nozzle at several different azimuthal orientations. Figure 4.10 emphasizes that the noise field has a strong azimuthal dependence, and the most noise reduction at each polar angle is sometimes at a different azimuthal angle. The noise from the long lip has the most noise reduction at the low polar angles, while the noise from the short lip is by far the quietest at the intermediate polar angles. In the forward arc at the high polar angles there is only a slight azimuthal variation of 1-2 *dB OASPL*. These trends are consistent with the previous studies by Viswanathan and Czech [43] as well.

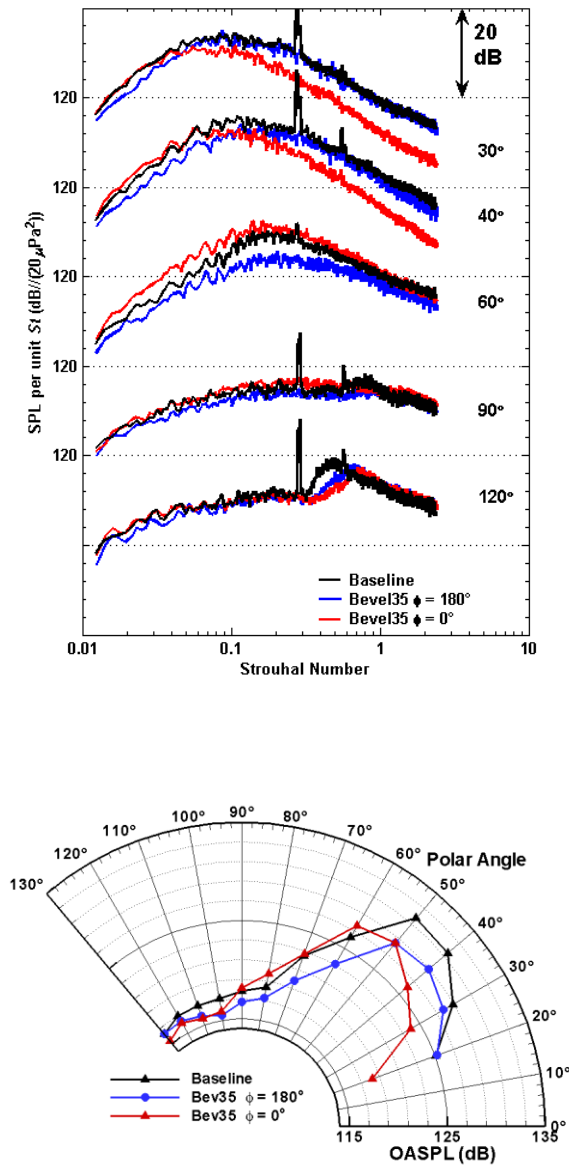


Figure 4.9: Spectra and OASPL Comparison of Heated jets, issuing from Md1.65 **Bevel35** Nozzle, with $NPR = 3.0$, $M_j = 1.36$, $TTR = 3$, $D_{noz} = 0.708''$, $f_c = 41562$ Hz, Scaled $R/D_j = 100$

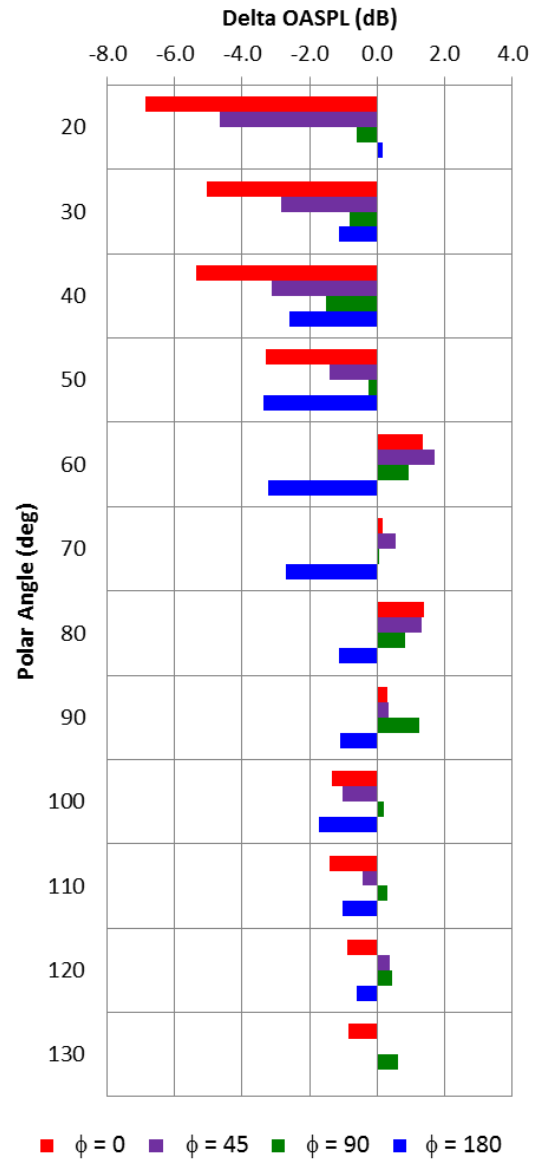


Figure 4.10: Delta OASPL Azimuthal Comparison of Heated jets issuing from Md1.65 **Bevel35** Nozzle, with $NPR = 3.0$, $M_j = 1.36$, $TTR = 3$

Next, the noise characteristics of the beveled nozzles in the presence of forward flight were investigated. Figure 4.11 shows the spectral and *OASPL* comparison for the over-expanded heat-simulated condition between the static noise and the noise with a forward flight Mach number of 0.17. The same trends as expected from references [52] and [53] can be seen.

Figure 4.12 shows the spectral and *OASPL* comparison between the baseline nozzle and the Bevel35 nozzle measured at two azimuthal angles, the long lip side ($\phi = 0^\circ$) and $\phi = 45^\circ$. When comparing the long lip side and the baseline, there is still a reduction of about 4 *dB* in the peak noise direction. Additionally, at high polar angles in the upstream direction there is a reduction of about 2 *dB* that was not present in for static tests. This could be due to the forward flight stream lessening the strength of the shock cells in the beveled nozzle jet. The noise produced at $\phi = 45^\circ$ is also no longer nearly identical to the baseline nozzle noise. There is a slight reduction when compared to the baseline at very low polar angles ($20^\circ - 40^\circ$) and an increase at intermediate polar angles ($60^\circ - 80^\circ$).

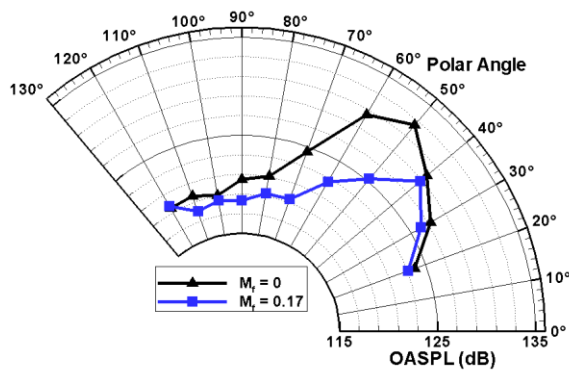
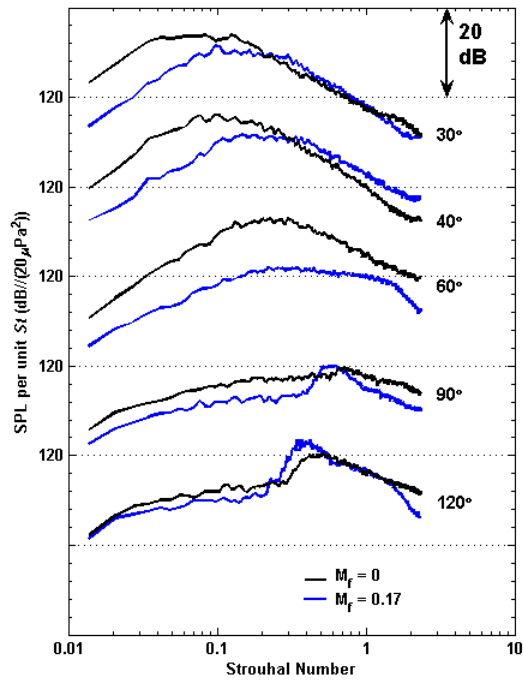


Figure 4.11: Spectra and OASPL Comparison of Heated Baseline jet with and without Forward Flight, issuing $M_d = 1.65$ Beveled Nozzle, with $M_j = 1.47$, $TTR = 3$, $D_{noz} = 0.708''$, $f_c = 42693$ Hz, Scaled $R/D_j = 100$. The forward flight data have been corrected for outer stream shear layer refraction.

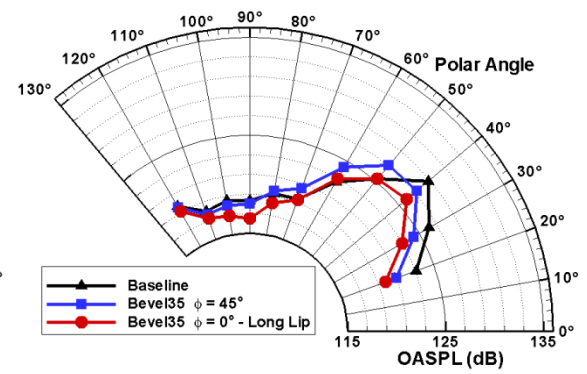
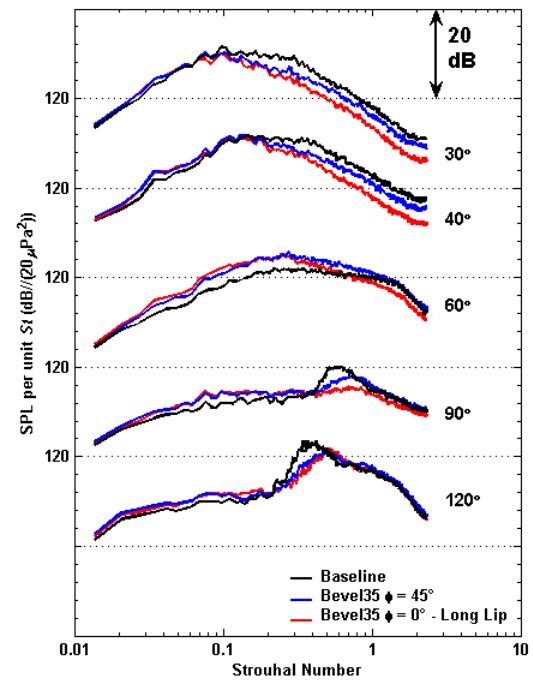


Figure 4.12: Spectra and OASPL Comparison of Heated jets issuing from $M_d = 1.65$ Beveled Nozzle, with Forward Flight of $M_f = 0.17$, with $M_j = 1.47$, $TTR = 3$, $D_{noz} = 0.708''$, $f_c = 42693$ Hz, Scaled $R/D_j = 100$.

Chapter 5

Examination of the Effects of Interior Hard Walled Nozzle Corrugations

5.1 Motivation and Review of Prior Work

As previously discussed, the interior hard wall corrugations were pioneered over several years of study by Seiner *et al.* [25] [44] [55]. The primary goal of the corrugation design was to reduce noise while not creating any adverse aero-performance effects for the Field Carrier Landing Practice (FCLP) mission. This mission is performed by U.S. Navy pilots in training to simulate the flight patterns typical of taking off and landing from a U.S. Navy Aircraft Carrier. It is performed using an F-18 aircraft at low altitude with the engine at settings near MIL power.

Acoustic measurements at various microphone polar locations along with thrust measurements and IR surveys of the jet exhaust were performed. Experiments were first conducted at the model scale at the University of Mississippi and later advanced to full-scale engine test stand tests. Figure 5.1 (taken from Seiner *et al.* [25]) shows narrowband acoustic spectra for three different far field microphone polar angles. These measurements were taken with a model scale with jet and nozzle conditions which simulated the engine operating at MIL power. The design Mach number of the baseline nozzle was 1.64, while the jet issuing from the nozzle had the following conditions: $NPR = 3.03$, $M_j = 1.37$, $TTR = 3.11$. The polar angles shown on the figure are industry angles such that they are measured from the jet inlet axis.

The corrugations can be seen to affect the acoustics in the downstream direction by decreasing the peak amplitude of the large scale structure noise and subsequently reducing noise at higher frequencies as well. Additionally, in the sideline and upstream directions the peak of the *BBSAN* is essentially eliminated. However, a slight increase in high frequency noise is noticeable at the upstream microphone. The corrugations achieve these noise reductions through two

methods. First the corrugations are designed to match this specific jet condition by matching the effective area ratio, thus eliminating most shocks within the flow and reducing the *BBSAN*. Additionally, the gradual buildup and abrupt termination of the corrugations at the nozzle exit creates downstream propagating vortices, similar to chevrons, and a wake flow which seemingly increases mixing and thus reduces the large scale structure noise.

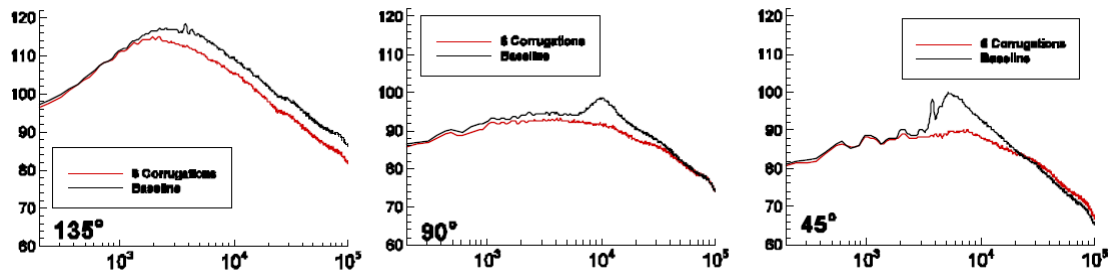


Figure 5.1: Narrowband Spectra Data from Seiner *et al.* [44] at model scale (1/10th Scale) which shows the effect of the interior nozzle corrugations. Three polar angles (measured from the upstream axis) are shown.

The corresponding model scale *OASPL* is shown in Figure 5.2 along with *OASPL* measured from a full scale test. The effects of the corrugations can be seen to scale very well to full-scale.

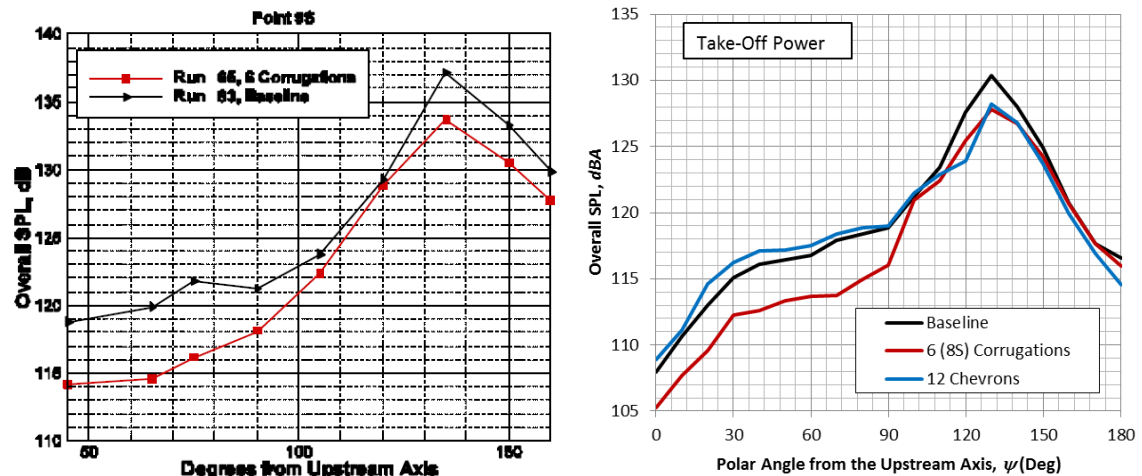


Figure 5.2: *OASPL* Data from Seiner *et al.* [44] [25] which shows the effect of the interior nozzle corrugations. The left image is model scale (1/10th Scale) and the right is a full scale test. The polar angles are measured from the upstream axis.

Significant noise reductions can be seen in Figure 5.2 of 3 *dB OASPL* in the peak noise emission direction along with 4-5 *dB OASPL* off the *BBSAN* noise in the upstream direction were measured. Additionally, thrust measurements showed that at these engine conditions the corrugations actually increased the measured thrust by ½ percent. This is due to the baseline engine nozzle typically operating off design with over-expanded jets, thus the corrugations increase thrust by decreasing the pressure drag. However, at altitude during cruise, the baseline engine exhaust nozzle would no longer be operating off design and the corrugations would then adversely affect thrust. Thus, the U.S. Navy never fully implemented the interior corrugations into the fleet. As already mentioned, Penn State has begun a program to develop fluidic corrugations which reproduce the acoustic benefits of the hard wall corrugations while having the ability to be actively controlled to better match engine exhaust nozzle conditions.

This current study was conducted to further the understanding of hard walled corrugations and facilitate the development of the nozzle fluidic corrugations. For these reasons many different over-expanded jet conditions were tested for both cold and heat-simulated jets. Acoustic measurements and flow visualizations were conducted at many different polar and azimuthal angles to enhance the understanding of the noise reduction mechanisms of the hard walled corrugations. The entirety of the acoustic measurement conditions are shown in Table 5.1 and flow visualizations were performed at a majority of these conditions as well. Important and meaningful comparisons were extracted and documented in the following sections.

At this time no measurements have been performed with the forward flight flow operating with corrugated nozzles. The fluidic injection system is still preliminary and not streamlined with tubes and pipes extending away from the nozzle, and thus the forward flight flow cannot be turned on. Therefore in order to be compared to the fluidic corrugations no forward flight was used for the hard walled corrugation measurements.

Table 5.1: Nozzle Parameters and Jet Conditions for Experiments

Nozzle	Jet Mach Number (M_j)	TTR	Polar Angle (ϑ) of 1 st Mic	Azimuthal Angle (ϕ)
Baseline	1.3, 1.37, 1.4, 1.47, 1.5, 1.6, 1.65	1	20° , 80°	-
2Corrug	1.3, 1.37, 1.4, 1.47, 1.5, 1.6, 1.65	1	20° , 80°	0° , 90°
3Corrug	1.3, 1.37, 1.4, 1.47, 1.5, 1.6, 1.65	1	20° , 80°	0° , 60°, 90°
6Corrug	1.3, 1.37, 1.4, 1.47, 1.5, 1.6, 1.65	1	20° , 80°	0° , 30°
6CorBev35	1.3, 1.37, 1.4, 1.47, 1.5, 1.6, 1.65	1	20° , 80°	0°, 45°, 90°, 135°, 180°
Baseline	1.36 , 1.47 , 1.56	3	20° , 80°	-
2Corrug	1.36 , 1.47	3	20° , 80°	0° , 90°
3Corrug	1.36 , 1.47	3	20° , 80°	60°, 90°
6Corrug	1.36	3	20° , 80°	0° , 30°
6Corrug	1.47 , 1.56	3	20° , 80°	30°
6CorBev35	1.36 , 1.47 , 1.56	3	20° , 80°	0° , 45° , 90° , 180°

Notes:

- 3) Column 4 lists the polar angle of the first microphone on the boom which holds 6 microphones separated by 10 degrees. So 20° means microphones were located at 20°, 30°, 40°, 50°, 60°, and 70°.

5.2 Flow Field Analysis

As already mentioned the nozzle corrugations were designed with a method of characteristics solution which should perform optimally at an NPR of 3.5. However, because of the small scale and low Reynolds's numbers of this facility, we have hypothesized that the boundary layers are larger in proportion to larger scale facilities. Therefore the most productive results are expected to be similar to those conditions run by Seiner *et al.* [44] [25]. To demonstrate this, averaged shadowgraph images are first shown for an NPR of 3.0 at a simulated TTR of 1.0 (cold), which results in a jet with a Mach number of 1.36. They will then be followed with shadowgraph images of the design condition. Unless otherwise noted, flow visualizations shown are averaged shadowgraph with 1 optical average and about ~60 digital averages.

Figure 5.3 shows the shadowgraph for both the Baseline nozzle and the 2Corrug nozzle at an NPR of 3.0. The 2Corrug nozzle is shown at two different azimuthal orientations to emphasize the three-dimensional flow that occurs. To the left of each shadowgraph image is a render of a cut-view nozzle at the same orientation to more easily visualize the location of the hard wall corrugations. The top image is the Baseline nozzle; you can clearly see the well-understood Mach disk and shock cell structure of this over-expanded jet. The middle image shows the 2Corrug with the corrugations in the horizontal orientation. The flow is spreading outwards slightly when compared to the baseline jet; also the Mach disk and oblique shock cone is smaller and weaker. The bottom image of Figure 5.3 shows the 2Corrug nozzle with the corrugations in the vertical orientation. From this perspective, the jet is shrinking and you cannot see the oblique shocks from the nozzle exit. In both orientations you can see the wake flow coming off of the corrugations and you can also notice a weakening of the downstream repeating shock cell structure.

Figure 5.4 is similar to the previous figure and shows the same jet condition, but for the 3Corrug and 6Corrug nozzles. The top two images show the 3Corrug nozzle at both the vertical and horizontal orientations. The wake flow and the deflection of the jet flow near the corrugations are still visible. The oblique shock cone and Mach disk can now be seen to be further weakened and shrunk from the 2Corrug nozzle. The spreading and shrinking of the jet is no longer as obvious with the 3Corrug nozzle. Furthermore, the downstream shock structure appears to be even weaker than the 2Corrug nozzle.

The third image, at the bottom, of Figure 5.4 is of the 6Corrug nozzle. The flow at the nozzle exit can be seen and appears to be in the flower petal design. The effect of the corrugations is easily visualized as strong streamwise wake flow. The normal shock is now almost completely eliminated, and the downstream shock cells are no longer visible. Additionally, the strength of any oblique shocks in the flow is weaker than any of the images already seen.

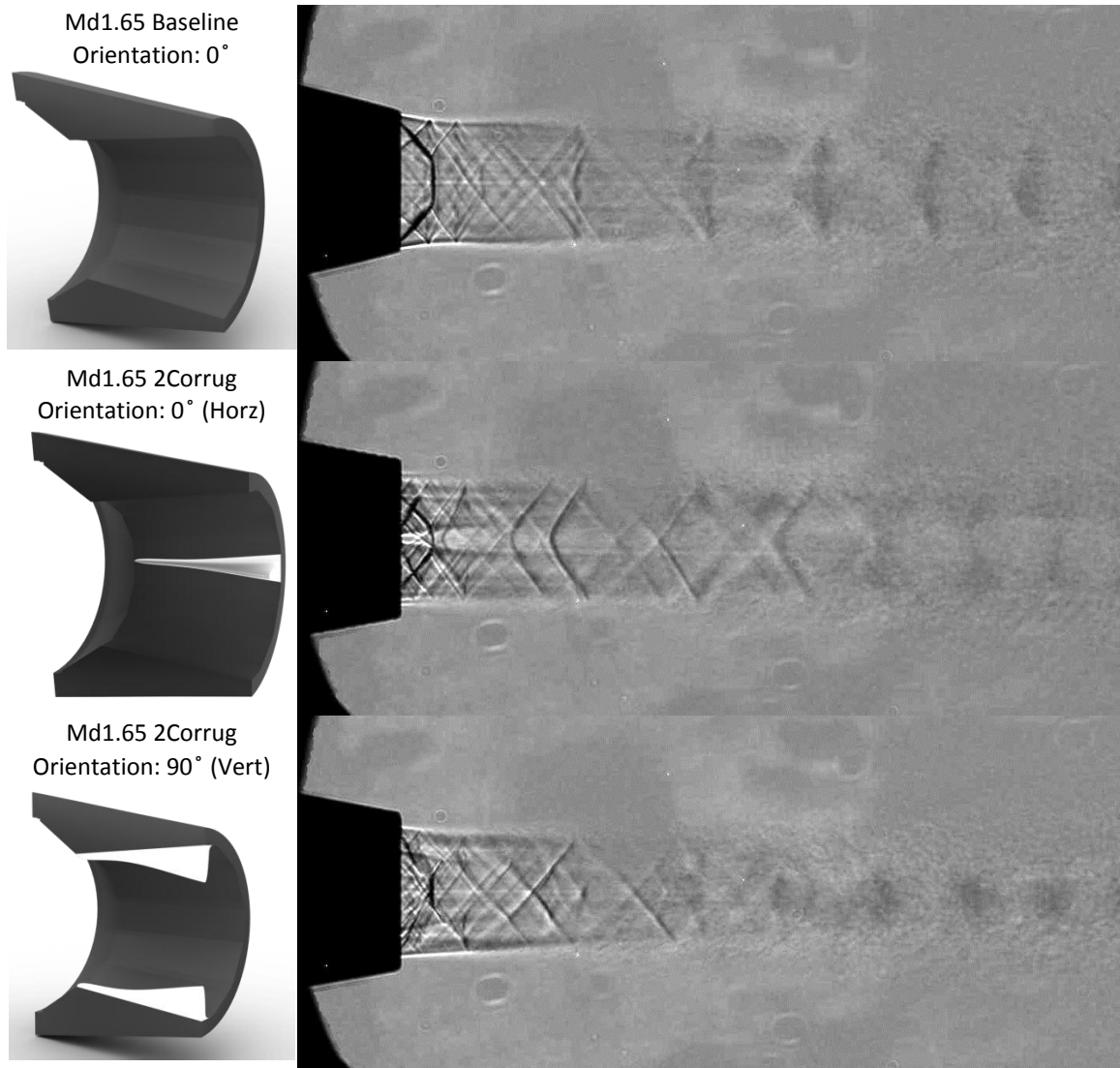


Figure 5.3: Averaged Shadowgraph Imagery of jets issuing from three different nozzles with $NPR = 3.0$, $M_j = 1.36$, $TTR = 1.2$, $D_{noz} = 0.708''$. From top to bottom the nozzles in each image are Md1.65 Baseline, Md1.65 2Corrug (Horizontal), Md1.65 2Corrug (Vertical). To the left of each image is also a description and visualization of the nozzle being used.

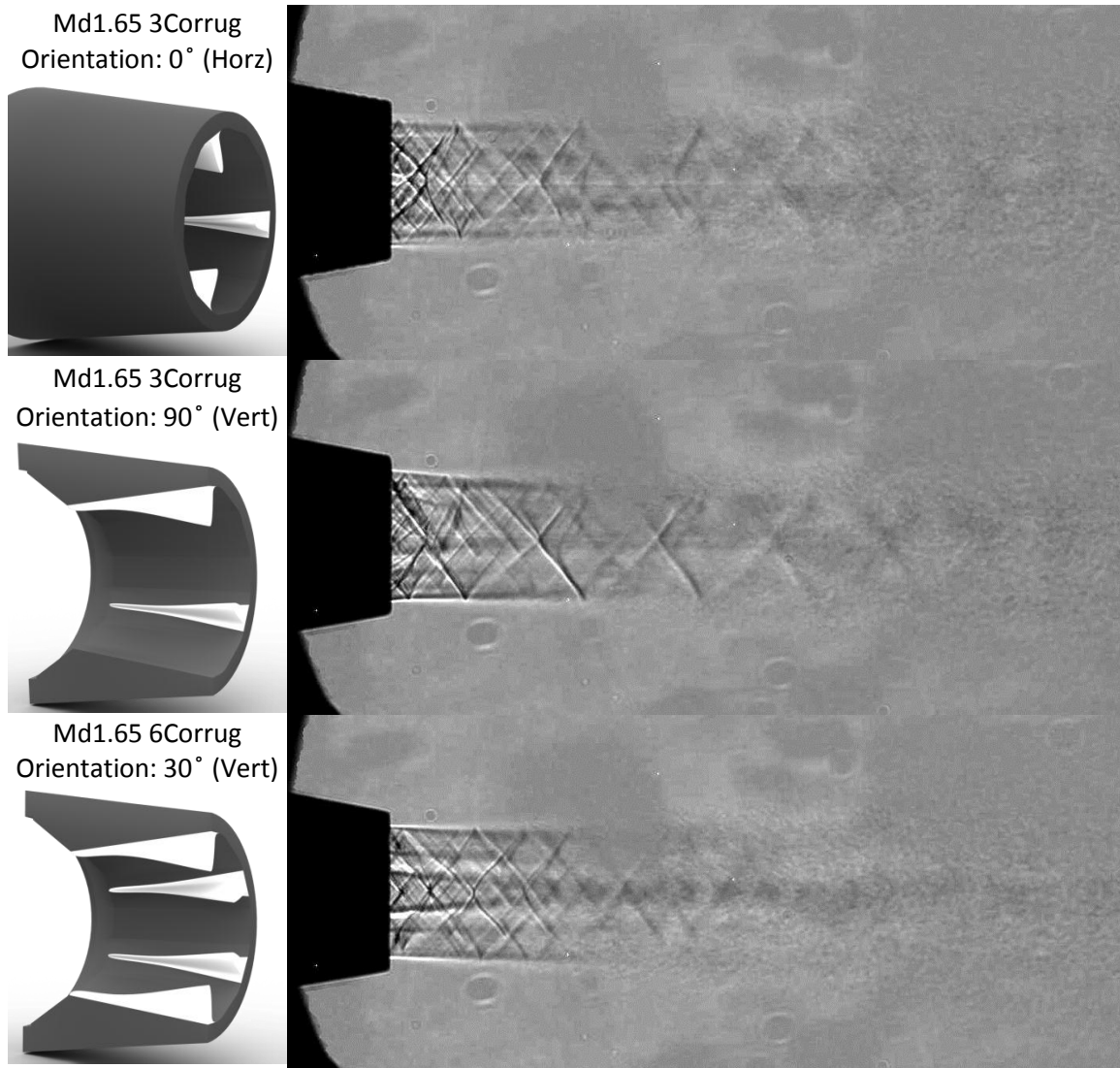


Figure 5.4: Averaged Shadowgraph Imagery of jets issuing from three different nozzles with $NPR = 3.0$, $M_j = 1.36$, $TTR = 1.2$, $D_{noz} = 0.708''$. From top to bottom the nozzles in each image are Md1.65 3Corrug (Horizontal), Md1.65 3Corrug (Vertical), Md1.65 6Corrug. To the left of each image is also a description and visualization of the nozzle being used.

The following two figures show the same nozzles and nozzle orientations as in Figure 5.3 and Figure 5.4 except at a different NPR . Figures 5.5 and 5.6 show cold jets issuing from the three nozzles at the original corrugation design condition, $NPR = 3.5$. Figure 5.5 shows the baseline jet on the top along two different azimuthal orientations of the 2Corrug nozzle in the middle and bottom shadowgraph images. The well-known flow features for an over-expanded

flow can still be seen from the baseline jet, with the oblique shock cone which terminates in a Mach disk followed by oscillating expansion waves and shock waves refracting off of the shear layer, creating the downstream shock cell structure. Comparing the two orientations of the 2Corrug nozzle to the previous jet condition, we can see that the Mach disk is now nearly eliminated from the flow. This indicates that the effective area ratio of the nozzle with two corrugations matches this jet condition better than was the case for the more highly over-expanded pressure ratio. Furthermore, the degradation of the downstream shock cell structure is seen to continue even more at this *NPR* of 3.5 than was seen in the previous figure for the 2Corrug nozzle at an *NPR* of 3.0.

Figure 5.6 then shows the same over-expanded jet condition of an *NPR* of 3.5 for two azimuthal orientations of the 3Corrug nozzle plus one view of the 6Corrug nozzle. All of the same dominant flow features as already discussed can still be seen, such as the weakening of the oblique shocks and downstream shock cells along with the strong streamwise wake flow issuing from the corrugations. The shocks from the 3Corrug nozzle at this condition appear weaker than any other nozzle or condition aside from the 6Corrug nozzle at an *NPR* of 3.0 in Figure 5.4. In the bottom image of Figure 5.6, which shows the jet issuing from the 6Corrug nozzle, the flow can be seen to expand slightly after the nozzle exit. This indicates that the effective area ratio of the nozzle with 6 corrugations causes the flow to be under-expanded at this *NPR* of 3.5. This further supports the hypothesis that the growth of the boundary layers causes the design nozzle pressure ratio to be lower than originally expected.

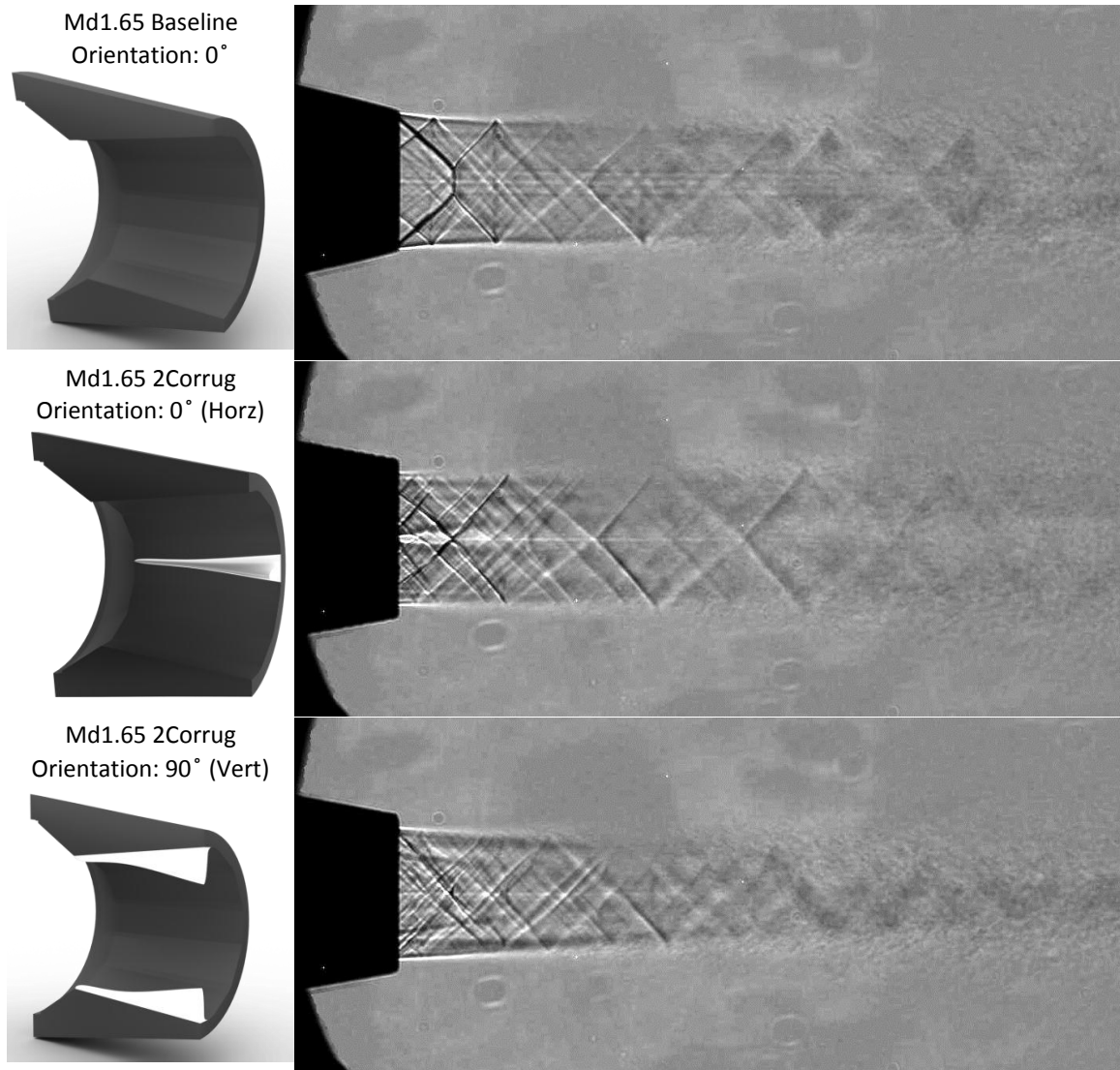


Figure 5.5: Averaged Shadowgraph Imagery of jets issuing from three different nozzles with $NPR = 3.5$, $M_j = 1.47$, $TTR = 1.2$, $D_{noz} = 0.708''$. From top to bottom the nozzles in each image are Md1.65 Baseline, Md1.65 2Corrug (Horizontal), Md1.65 2Corrug (Vertical). To the left of each image is also a description and visualization of the nozzle being used.

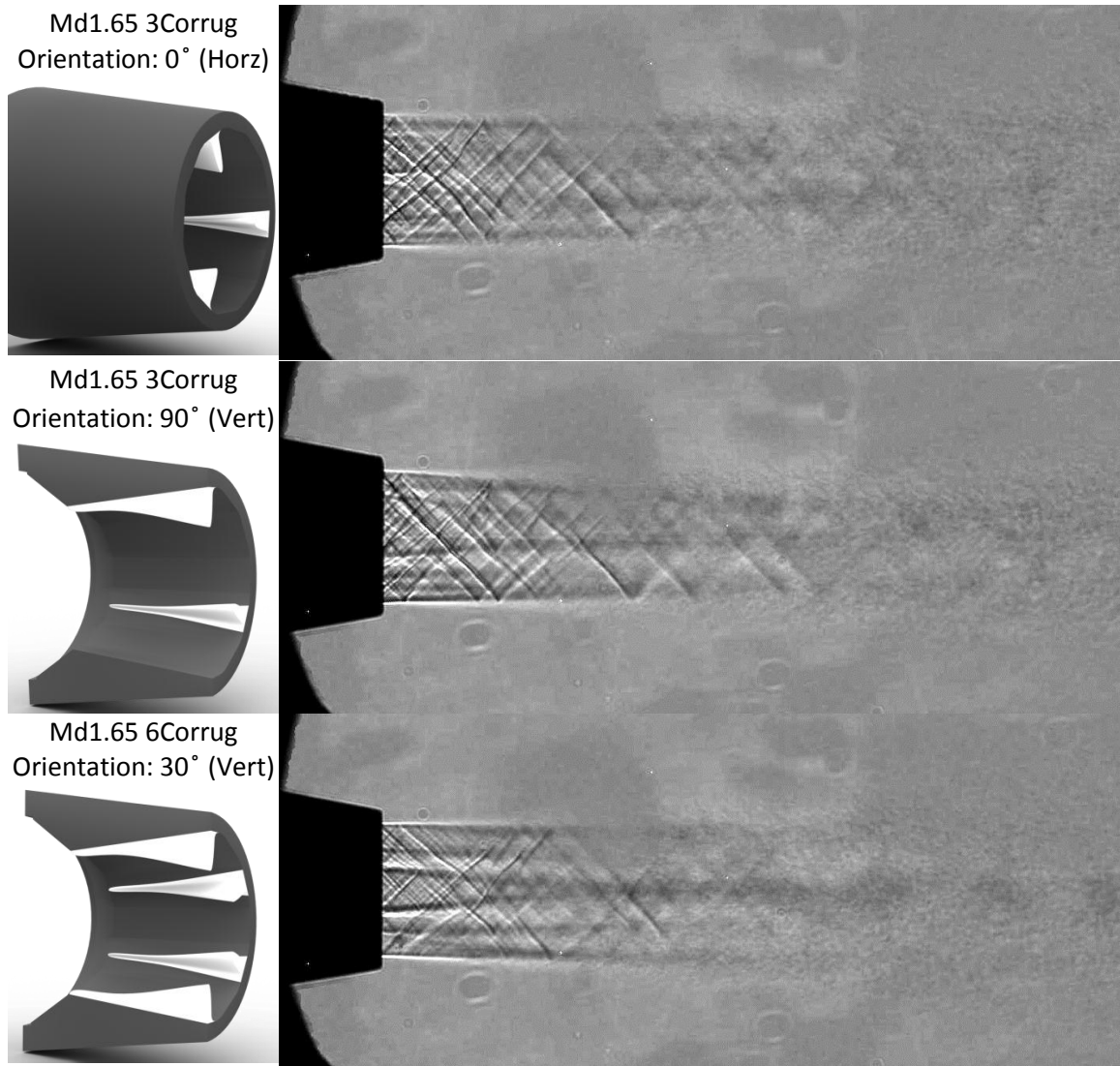


Figure 5.6: Averaged Shadowgraph Imagery of jets issuing from three different nozzles with $NPR = 3.5$, $M_j = 1.47$, $TTR = 1.2$, $D_{noz} = 0.708''$. From top to bottom the nozzles in each image are Md1.65 3Corrug (Horizontal), Md1.65 3Corrug (Vertical), Md1.65 6Corrug. To the left of each image is also a description and visualization of the nozzle being used.

In review, all of the previous flow visualization images in this chapter were averaged shadowgraph images of different cold jet conditions issuing from different nozzles. Figure 5.7 shows Schlieren images of an over-expanded, slightly heat simulated jet issuing from two different nozzles at two different nozzle orientations each. All images are averaged schlieren at an NPR of 3.5 and a simulated $TTR = 1.2$ with 10 optical averages and about 5 digital averages. The

addition of a small amount of helium enhances the optical quality of the image. Additionally, since the schlieren set-up was used, with a horizontal knife edge, the dark regions on the upper half of the image become light regions on the bottom half of the image.

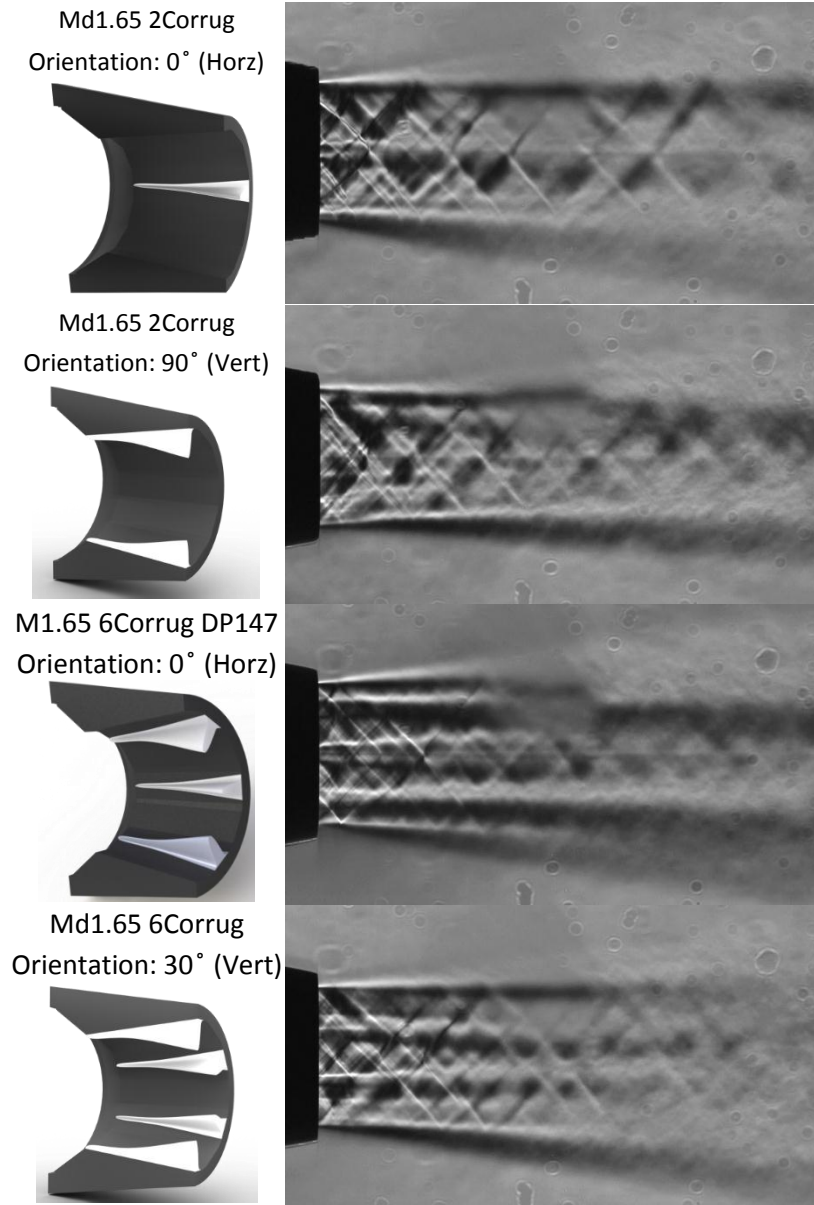


Figure 5.7: Averaged Schlieren Imagery of jets issuing from two different nozzles at two azimuthal orientations each with $NPR = 3.5$, $M_j = 1.47$, $TTR = 1.2$, $D_{noz} = 0.708''$. From top to bottom the nozzles in each image are Md1.65 2Corrug (Horizontal), Md1.65 2Corrug (Vertical), Md1.65 6Corrug (Horizontal), and Md1.65 6Corrug (Vertical). To the left of each image is also a description and visualization of the nozzle being used.

In Figure 5.7 the top two images show jets issuing from the 2Corrug nozzle with the corrugations both in the horizontal and vertical plane, while the bottom two images show the same for the 6Corrug nozzle. For reference an averaged schlieren image of the same jet condition for the baseline nozzle has already been shown in Chapter 3 in image C of Figure 3.4. Along with supporting and corroborating all the analysis presented from the previous shadowgraph images, these images clearly show the shape and spreading rate of the jet. The images of jets issuing from the 2Corrug nozzle show how the jet spreads outwards in the plane orthogonal to the 2 corrugations while shrinking and contracting in in plane with the corrugations. In comparison, the 6Corrug nozzle jets do not appear to have any significant azimuthal difference in the shape of the jet. Additionally, these images show that the corrugation wake flow does not disappear quickly, but still exists after several nozzle diameters.

Figure 5.8 presents more averaged shadowgraphs of cold under-expanded jets. The jet condition for this figure was at an NPR of 4.0 (results in $M_j = 1.56$) which results in only a slight pressure imbalance for the baseline jet (which has a design Mach number of 1.65). The top image shows the baseline nozzle while the bottom shows the 6Corrug nozzle with two corrugations in the vertical plane. The corrugations cause the jet to be under-expanded at this condition because of the effective area ratio with six corrugations. This is seen by the slight expansion of the jet after the nozzle exit and the reappearance of the downstream shock cell structure when compared to the 6Corrug nozzle at lower pressure ratios.

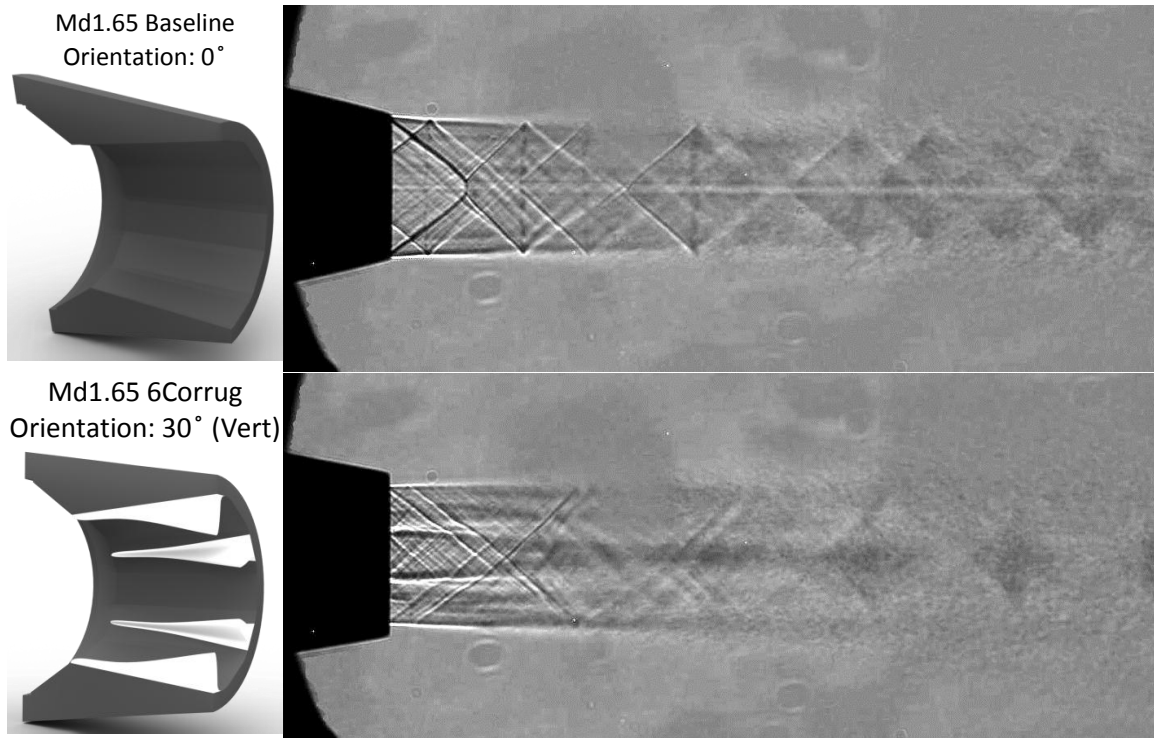


Figure 5.8: Averaged Shadowgraph Imagery of jets issuing from two different nozzles with $NPR = 4.0$, $M_j = 156$, $TTR = 1$, $D_{noz} = 0.708''$. From top to bottom the nozzles in each image are Md1.65 3Corrug Baseline, Md1.65 6Corrug. To the left of each image is also a description and visualization of the nozzle being used.

5.3 Acoustic Results and Noise Reduction

5.3.1 Unheated (Cold) Jets

Figure 5.9 shows the acoustic comparison of over-expanded cold jets emitted from the baseline and 2Corrug nozzles. The 2Corrug nozzle is shown at $\phi = 0^\circ$ (microphones in plane with the corrugations) and $\phi = 90^\circ$ (microphones out of plane with the corrugations). At both azimuthal angles the peak of the mixing noise is reduced, however when the corrugations are in plane with the microphones there is an increase in the high frequency noise at the low polar angles (20° - 60°). There is a slight reduction in the low frequency noise in the forward arc, and the

peak of the shock noise has been lowered and shifted to a higher frequency. Looking back at Figure 5.3, the effect of the changes in the *BBSAN* correlate well with the visualized change in the shock structure of the jet. The noise emitted from the 3Corrug nozzle (at three azimuthal orientations) is shown in Figure 5.10 with the same jet condition as those shown in Figure 5.9. The azimuthal directivity of this nozzle is very apparent at the low azimuthal angles. The peak noise is very nearly the same at all low angles, but the high frequency noise is at a maximum when in plane with a corrugation, and at a minimum when exactly in between two of the three corrugations. The difference is as much as ~ 4 dB on the narrowband spectra. The azimuthal directivity is most apparent at polar angles between 40° - 80° . Even with the azimuthal directivity, the 3 Corrugation nozzle still reduces the *OASPL* between 1.5-3.5 dB across all polar angles.

The effect of 6 corrugations on the emitted noise is shown in Figures 5.11 and 5.12.. Figure 5.11 shows the same over-expanded condition as the previous two figures ($NPR = 3.0$, $M_j = 1.36$) while Figure 5.12 shows a slightly higher pressure ratio condition at $NPR = 3.5$ ($M_j = 1.47$). The first thing to notice from both Figures is that the azimuthal directivity observed with both the 2Corrug and the 3Corrug nozzle is nearly eliminated. At $NPR = 3.0$ the 6Corrug nozzle reduces the *OASPL* by about 4 dB across all polar angles. By examining the narrowband spectra it can be seen that the peak of the mixing noise is lowered ~ 4 -5 dB across all low polar angles. Additionally, when examining the effect on the *BBSAN* the peak is again lowered and shifted to higher frequency, which correlates with the examination of the shock cell structure in Figure 5.4. Recalling that the corrugation design was based upon six corrugations at an *NPR* of 3.5, we would expect Figure 5.12 to show even more noise reduction than Figure 10 ($NPR = 3.0$). However, upon examining this condition we see that this is not the case. The peak noise level in the narrowband acoustic spectra is lowered by about the same amount as the other condition; however there is now a rise in the high frequency noise that wasn't observed before. This may be

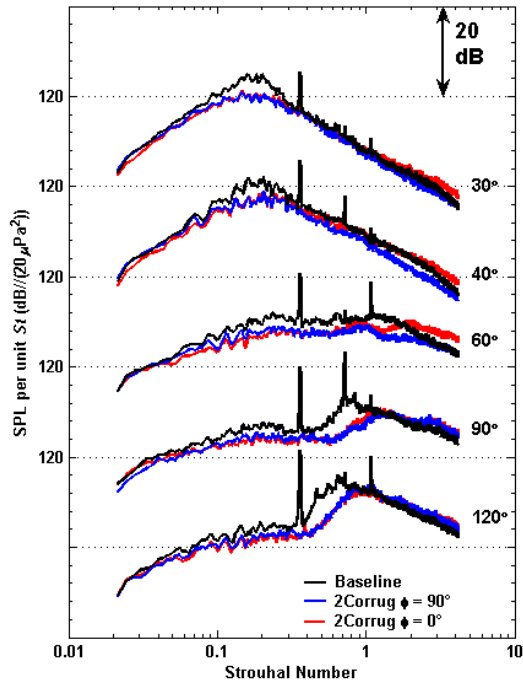


Figure 5.9: Spectra and OASPL Comparison of Heated jets, measured at two azimuthal angles, issuing from $M_d 1.65$ 2Corrug Nozzle, with $NPR = 3.05$, $M_j = 1.37$, $TTR = 1$, $D_{noz} = 0.708''$, $f_c = 24085$ Hz, Scaled $R/D_j = 100$

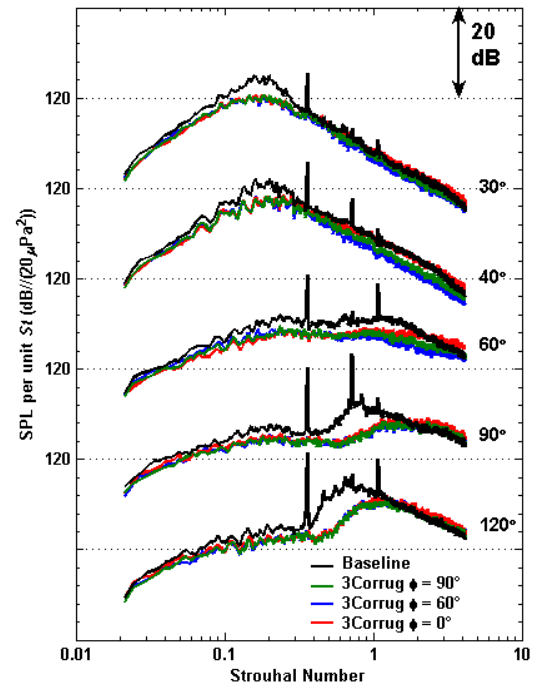


Figure 5.10: Spectra and OASPL Comparison of Heated jets, measured at three azimuthal angles, issuing from $M_d 1.65$ 3Corrug Nozzle, with $NPR = 3.05$, $M_j = 1.37$, $TTR = 1$, $D_{noz} = 0.708''$, $f_c = 24085$ Hz, Scaled $R/D_j = 100$

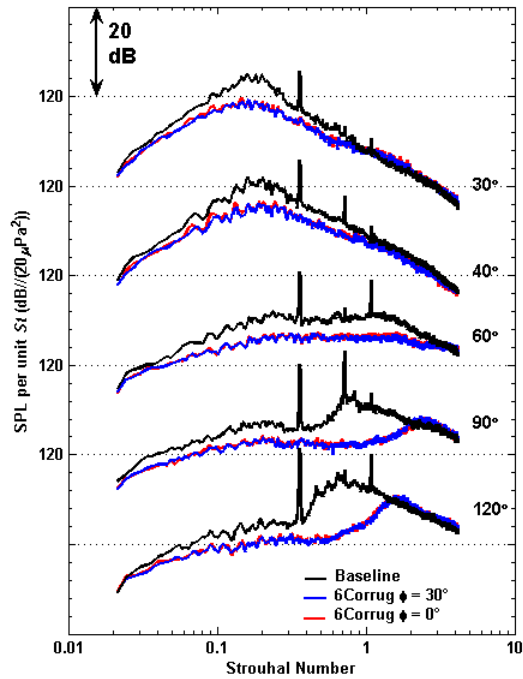


Figure 5.11: Spectra and *OASPL* Comparison of Heated jets, measured at two azimuthal angles, issuing from Md1.65 **6Corrug** Nozzle, with $NPR = 3.05$, $M_j = 1.37$, $TTR = 1$, $D_{noz} = 0.708''$, $f_c = 24085$ Hz, Scaled $R/D_j = 100$

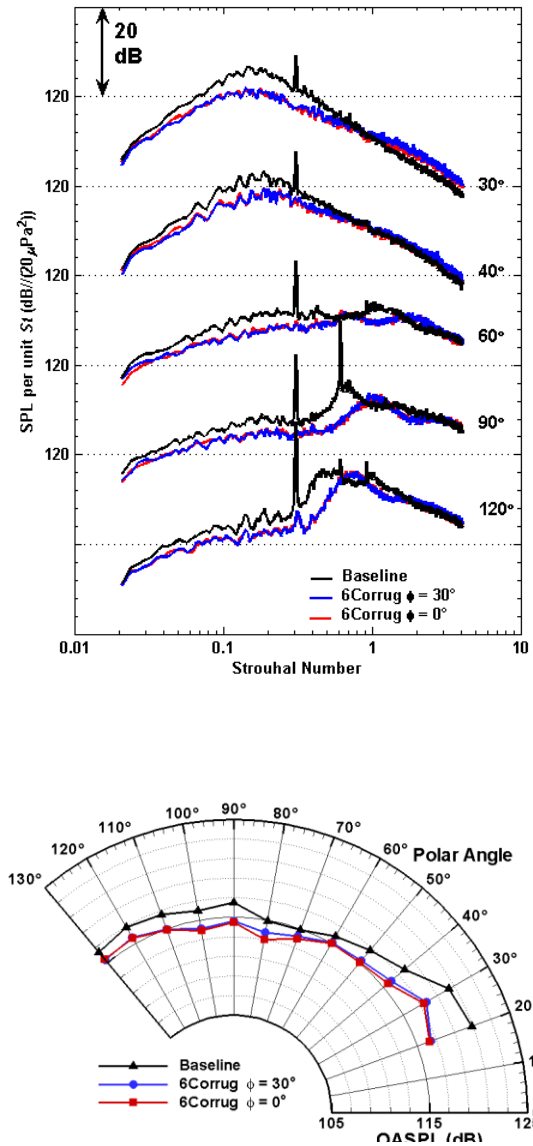


Figure 5.12: Spectra and *OASPL* Comparison of Heated jets, measured at two azimuthal angles, issuing from Md1.65 **6Corrug** Nozzle, with $NPR = 3.5$, $M_j = 1.47$, $TTR = 1$, $D_{noz} = 0.708''$, $f_c = 24673$ Hz, Scaled $R/D_j = 100$

due to the increase in energy of the vortices created by the corrugations. Furthermore, when examining the effect of the six corrugations on the *BBSAN* we can see that the peak of the *BBSAN* is only very slightly lowered and shifted less than before. Additionally, the *OASPL* reductions from the 6Corrug nozzle at this over-expanded condition of $NPR = 3.5$ range only from ~ 0.5 - 2.0

dB. This further substantiates the hypothesis that the nozzle performs better at an $NPR = 3.0$ than $NPR = 3.5$ because of the growth of the boundary layer in this low Reynolds's number experiment. The boundary layer growth causes the effective nozzle area of the six corrugation nozzle to be closer to the area ratio which results in a perfectly expanded cold jet at $NPR = 3.0$.

5.3.2 Heat Simulated Jets

Figures 5.13 and 5.14 examine the effect on the emitted noise by heat-simulated jets at an $NPR = 3.0$ issuing from the 2Corrug and 3Corrug nozzles. The azimuthal directivity observed in the cold jets is still apparent in heat-simulated jets. Again there is more noise reduction when the plane of microphones is located in between the corrugations. We can see that the 2Corrug nozzle shows reductions of $\sim 2\text{-}3$ *dB* in the aft polar angles ($20^\circ\text{-}50^\circ$), while the 3Corrug nozzle shows reductions between of $\sim 4\text{-}5$ *dB* at those same angles. Additionally both two corrugations and three corrugations show reductions of about $\sim 1\text{-}2$ *dB* in the *BBSAN* in the forward arc.

The acoustic spectra and *OASPL* from heat-simulated jets issuing from the 2Corrug and 3Corrug nozzles at an $NPR = 3.5$ are shown in Figures 5.15 and 5.16. The same trends observed at the lower nozzle pressure ratio are observed. However, the effective area ratio of the corrugated nozzle now causes the jet to be closer to perfectly expanded which results in more noise reduction in the *BBSAN*. The peak of the *BBSAN* in Figure 5.15 is significantly reduced and shifted to higher frequency, which results in a reduction of $\sim 2\text{-}3$ *dB OASPL* at the polar angles of $90^\circ\text{-}130^\circ$. In Figure 5.16 we can see that the 3Corrug nozzle affects the *BBSAN* even more with reductions of ~ 3 *dB OASPL* across all sideline and forward angles.

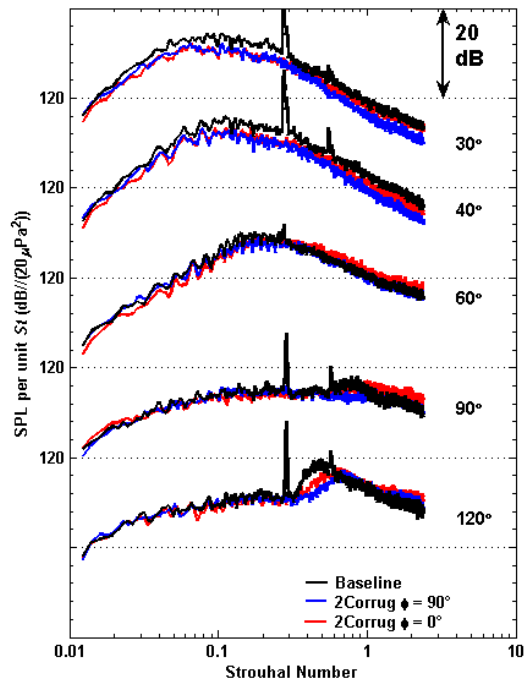


Figure 5.13: Spectra and OASPL Comparison of Heated jets, measured at two azimuthal angles, issuing from Md1.65 **2Corrug** Nozzle, with $NPR = 3.0$, $M_j = 1.36$, $TTR = 3$, $D_{noz} = 0.708''$, $f_c = 41562$ Hz, Scaled $R/D_j = 100$

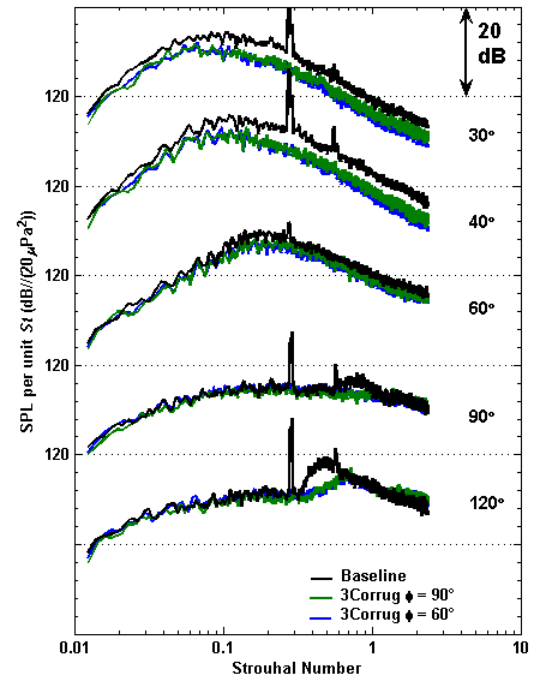


Figure 5.14: Spectra and OASPL Comparison of Heated jets, measured at two azimuthal angles, issuing from Md1.65 **3Corrug** Nozzle, with $NPR = 3.0$, $M_j = 1.36$, $TTR = 3$, $D_{noz} = 0.708''$, $f_c = 41562$ Hz, Scaled $R/D_j = 100$

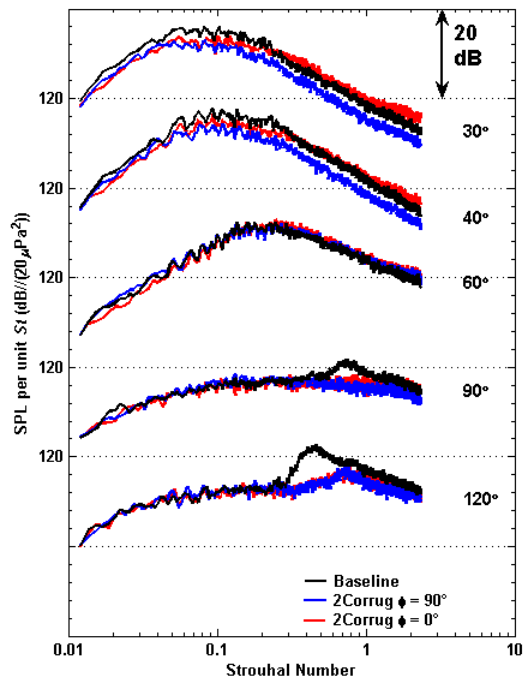


Figure 5.15: Spectra and *OASPL* Comparison of Heated jets, measured at two azimuthal angles, issuing from Md1.65 **2Corrug** Nozzle, with $NPR = 3.5$, $M_j = 1.47$, $TTR = 3$, $D_{noz} = 0.708''$, $f_c = 42735$ Hz, Scaled $R/D_j = 100$

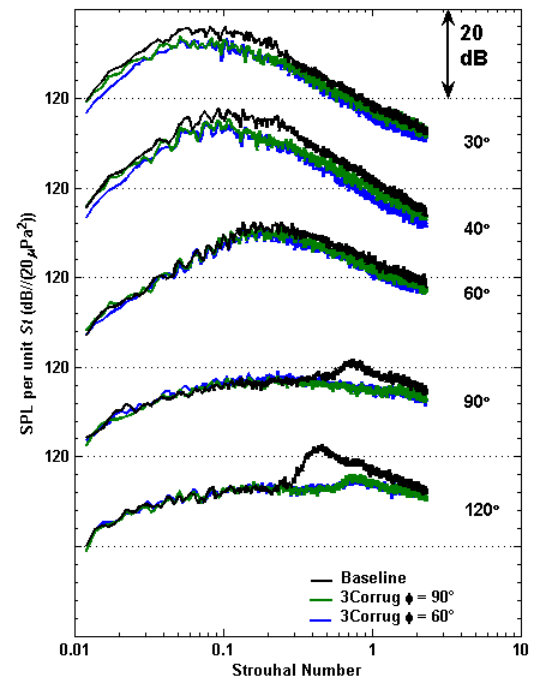


Figure 5.16: Spectra and *OASPL* Comparison of Heated jets, measured at two azimuthal angles, issuing from Md1.65 **3Corrug** Nozzle, with $NPR = 3.5$, $M_j = 1.47$, $TTR = 3$, $D_{noz} = 0.708''$, $f_c = 42735$ Hz, Scaled $R/D_j = 100$

Figure 5.17 and Figure 5.18 examine the acoustic spectra and *OASPL* emitted from jets issuing from the 6Corrug nozzle at the two different over-expanded pressure ratios already discussed. From Figure 5.17 we can see that the azimuthal directivity is mostly eliminated with the *OASPL* being within less than ~ 0.5 dB at all polar angles for both of the azimuthal angles. Just as with the 3Corrug nozzle there is a large reduction of about ~ 4 dB of the peak of the mixing noise at the low polar angles, which results in a reduction of ~ 3 -4 dB *OASPL* at the aft angles (20° - 50°). However, now we can notice that the reduction of the *BBSAN* for the 6Corrug nozzle in Figure 5.17 is not as pronounced as it was for the 3Corrug nozzle. The hypothesis is that this is again due to the low Reynolds's number of the small-scale helium-air mixture jets causing the boundary layer growth to be larger. Thus the effective area ratio was changed and the conditions we tested were not perfectly expanded. However, we can still see a reduction in the *OASPL* of about 2 dB at the forward angles for an *NPR* of 3.5. Thus it is hypothesized that for heat-simulated jets the optimal jet condition where the effective area ratio of six corrugations would best match the jet condition with growing boundary layers lies somewhere between an *NPR* of 3.0 and 3.5.

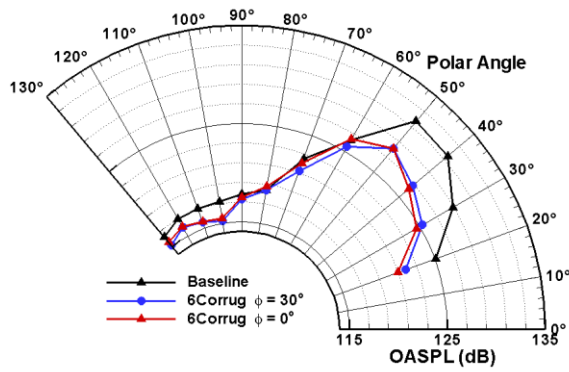
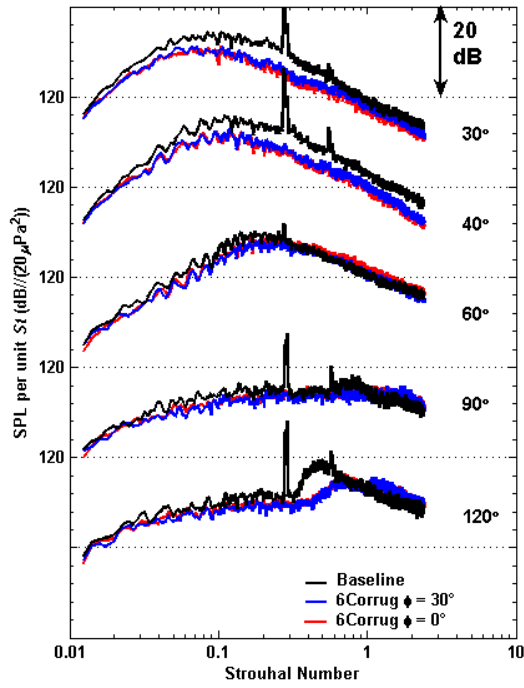


Figure 5.17: Spectra and *OASPL* Comparison of Heated jets, issuing from Md1.65 **6Corrug** Nozzle, with $NPR = 3.0$, $M_j = 1.36$, $TTR = 3$, $D_{noz} = 0.708''$, $f_c = 41562$ Hz, Scaled $R/D_j = 100$

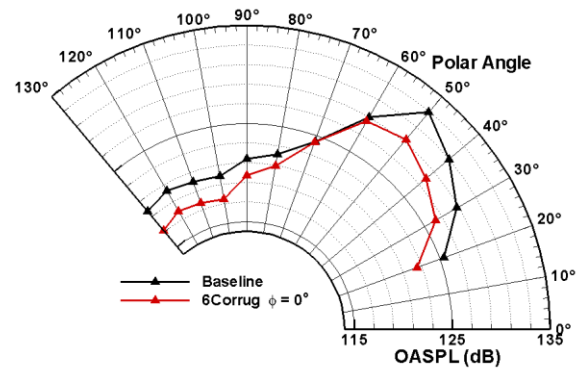
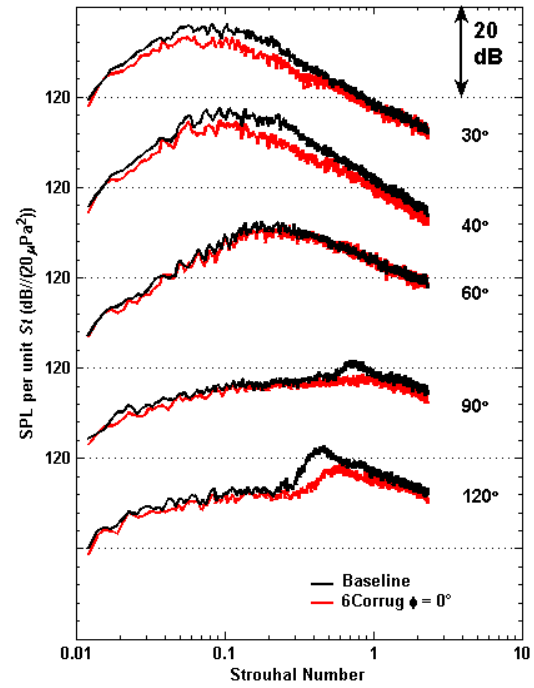


Figure 5.18: Spectra and *OASPL* Comparison of Heated jets, issuing from Md1.65 **6Corrug** Nozzle, with $NPR = 3.5$, $M_j = 1.47$, $TTR = 3$, $D_{noz} = 0.708''$, $f_c = 42735$ Hz, Scaled $R/D_j = 100$

Figure 5.19 shows the acoustic comparison between the baseline nozzle and the 6Corrug nozzle at one azimuthal orientation for an NPR of 4.0 and $TTR = 3.0$. This jet condition results in the baseline jet being only slightly over-expanded; recalling Figure 5.8 the Mach disk is almost eliminated along with weakened downstream shock cell structures. Therefore the effective area ratio of the nozzle with 6 corrugations does not match the jet condition and can be seen to increase the amount of shocks within the flow. This can be seen by an increase in the peak of the *BBSAN* and high frequency noise at the forward angles. However, it can be seen that there is still a benefit at the low polar angles due to the mixing enhancement created by the corrugations.

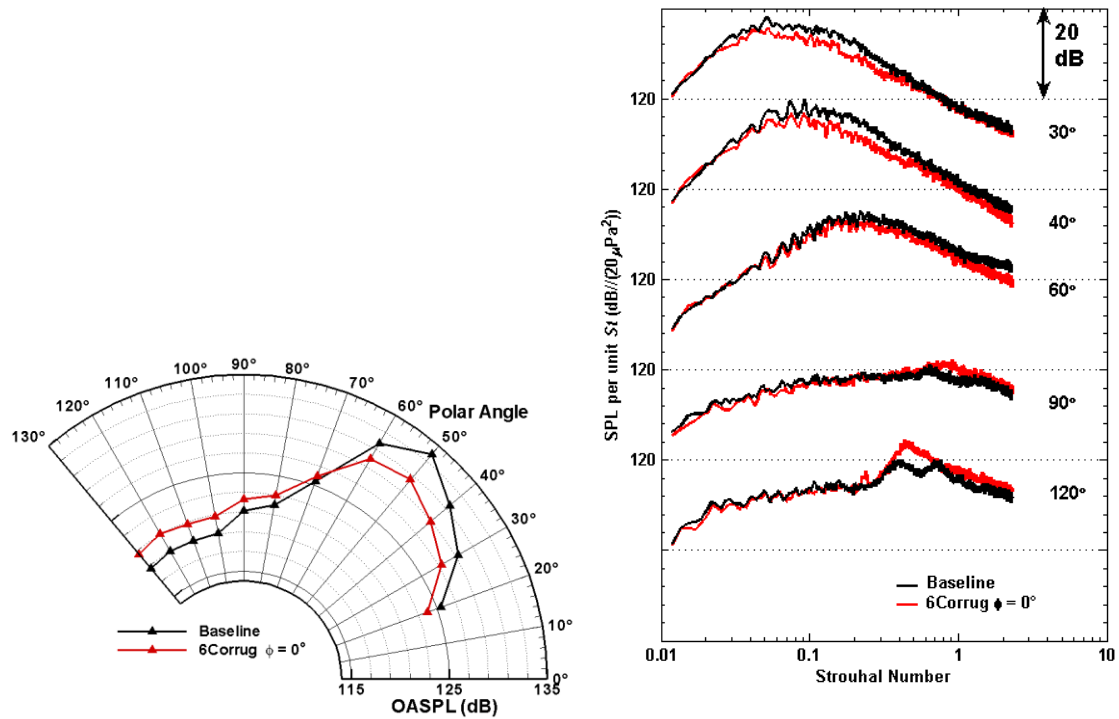


Figure 5.19: Spectra and *OASPL* Comparison of Heated jets, issuing from Md1.65 6Corrug Nozzle, with $NPR = 4.0$, $M_j = 1.56$, $TTR = 3$, $D_{noz} = 0.708''$, $f_c = 43531$ Hz, Scaled $R/D_j = 100$

Chapter 6

Comparison of the Combination of Interior Hard Walled Nozzle Corrugations and a Beveled Exit Plane

6.1 Motivation and Review of Prior Work

The noise suppression mechanisms of interior hard walled corrugations and a beveled exit on supersonic converging diverging nozzle are not fully understood. Whether or not the two different methods can be combined and the noise reduction superimposed is presently not known.

The combination has been explored only briefly by Viswanathan and colleagues [59]. Their results showed that when compared to a nozzle with only corrugations and no bevel, the combination nozzle increased shock noise significantly. However, upon further analysis the hard walled corrugations within the combination nozzle extended to the nozzle exit on the short lip side of the bevel, and were truncated abruptly throughout the rest of the nozzle at that point. Viswanathan *et al.* [59] attributed the lack of noise reduction and increase in noise to the large amount of shock waves in the flow which would have been created by this abrupt end of the corrugation inserts.

As already documented in Chapter 3, the corrugations used in the combination nozzle in this study continue to the nozzle exit plane. The difference in nozzle design should result in different results and conclusions. The flow field and acoustic field of nozzles with both corrugations and a beveled exit plane are examined in conjunction with purely beveled and purely corrugated nozzles to better understand the effects of the combination.

6.2 Flow Field Analysis

Figure 6.1 shows averaged shadowgraph images for the combination nozzle, 6CorBev35, with the long lip down. Each image is made up of 50-60 digital averages with zero optical averages. The orientation of the nozzle and location of the corrugations can be seen through a cut-view CAD rendering of the nozzle to the left of the shadowgraph image. Three jet conditions are shown with nozzle pressure ratios from top to bottom of 3.0, 3.5 and 4.0, respectively. These can be compared to the baseline and purely corrugated nozzles from shadowgraph images in Chapter 5.

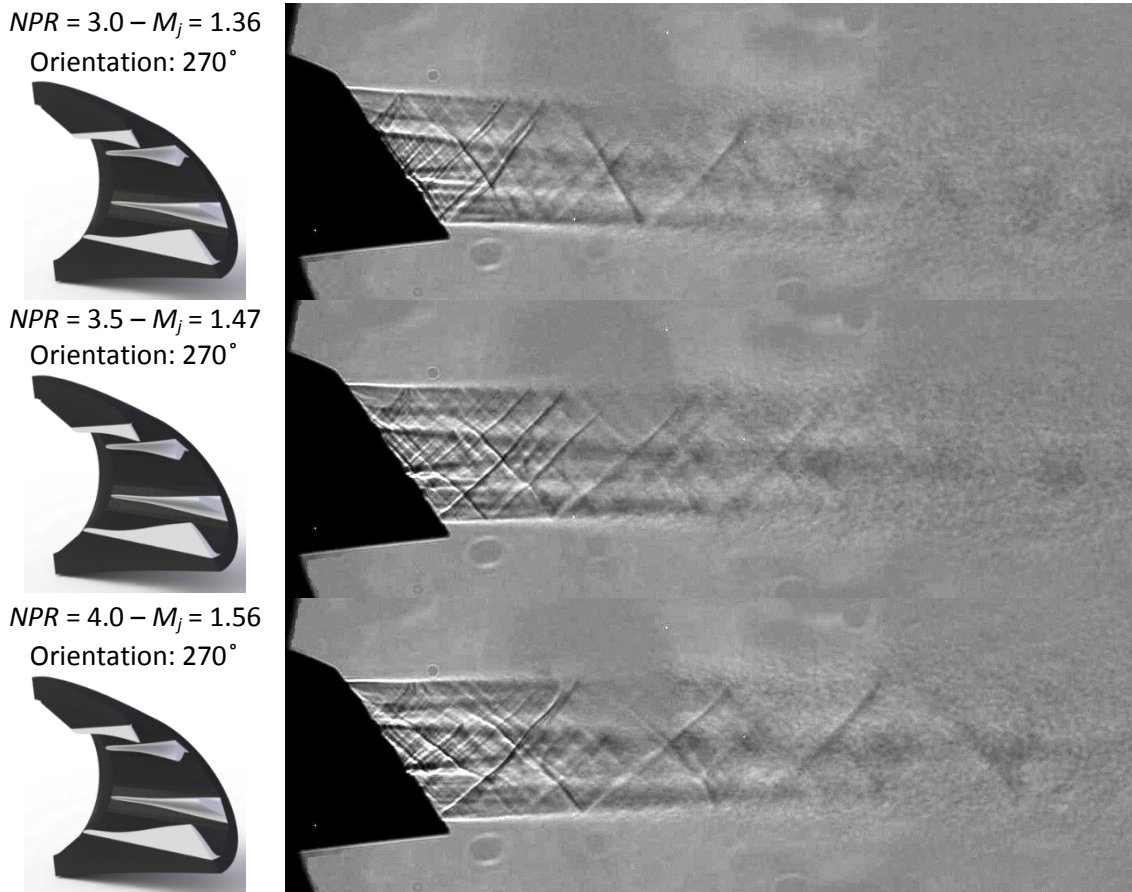


Figure 6.1: Averaged Shadowgraph Imagery of jets issuing from the Md1.65 6CorBev35 Nozzle with three different jet conditions. All jets are $TTR = 1$, $D_{noz} = 0.708''$. From top to bottom the jet conditions in each image are $NPR = 3.0$, $NPR = 3.5$, $NPR = 4.0$. To the left of each image is also a description and visualization of the nozzle being used.

The flow exhausting from the 6CorBev35 nozzle shows features similar to the 6Corrug nozzle with the weakening of the oblique shocks and downstream shock cell structure. It can be seen that there is no apparent Mach disk at any of the over-expanded flow conditions. Furthermore, the strong streamwise wake flow is visible. Additionally, the small deflection angle which has been observed in supersonic beveled nozzles is still existent for the combination of the bevel and the interior hard walled corrugations. For purely beveled nozzles, the flow was seen to deflect towards the long lip when over-expanded, have no deflection when perfectly expanded, and deflect towards the short lip when under-expanded. By examining the deflection direction of the three jet conditions for the 6CorBev35 nozzle at an NPR of 3.0, the nozzle is over-expanded, while at an NPR of 4.0 the nozzle is under-expanded. The flow through the nozzle at an NPR of 3.5 appears to be nearly perfectly expanded when examining the deflection angle.

6.3 Acoustic Results and Noise Reduction

6.3.1 Unheated (Cold) Jets

Presented first in Figures 6.2 and 6.3 are acoustic spectra of cold jets issuing from the 6CorBev35 nozzle in comparison with the same jet condition from the baseline nozzle. Both figures are for an NPR of 3.0, $TTR = 1.0$. The difference between the figures is that Figure 6.2 shows the measured sound from the polar array off the long lip side of the nozzle (azimuthal angles, $\phi = 0^\circ$, $\phi = 45^\circ$, $\phi = 90^\circ$), while Figure 6.3 shows the acoustics off of the short lip side of the nozzle (azimuthal angles, $\phi = 90^\circ$, $\phi = 135^\circ$, $\phi = 180^\circ$). The first thing to notice is that the 6CorBev35 nozzle shows very little azimuthal directivity, which in contradiction of the acoustic field that purely beveled nozzles produce. Second the jets emitted from combination 6CorBev35 nozzle shows a reduction in the peak of the large scale structure noise at the aft angles, while also

shifting and decreasing the peak of the *BBSAN* at the forward and sideline angles. This results in a uniform noise reduction of ~ 3 dB *OASPL* across all polar and azimuthal angles.

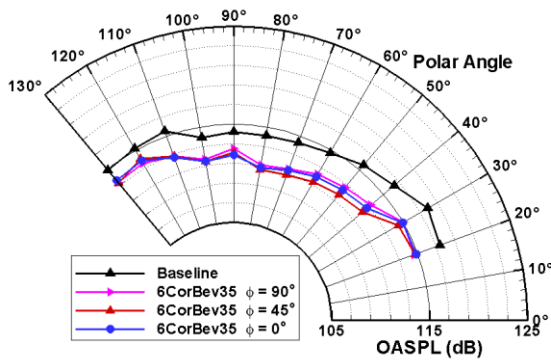
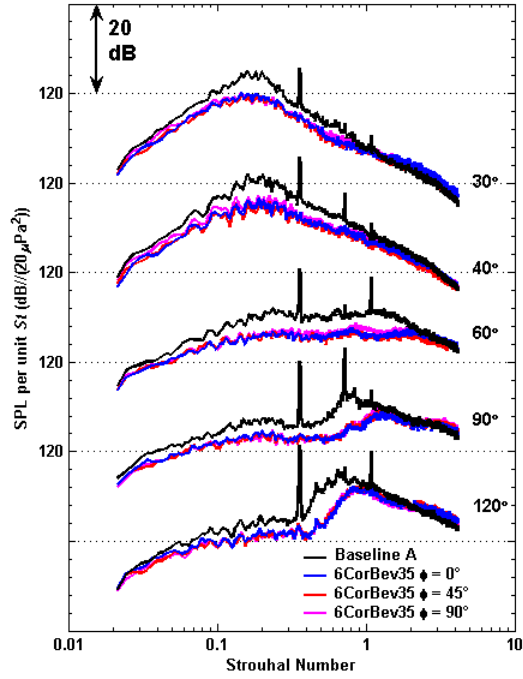


Figure 6.2: Spectra and *OASPL* Comparison of Cold jets, issuing from Md1.65 **6CorBev35** Nozzle from three azimuthal orientations on the long lip side, with $NPR = 3.05$, $M_j = 1.37$, $TTR = 1$, $D_{noz} = 0.708''$, $f_c = 24085$ Hz, Scaled $R/D_j = 100$

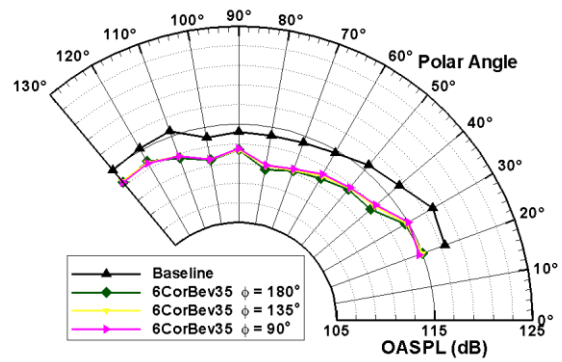
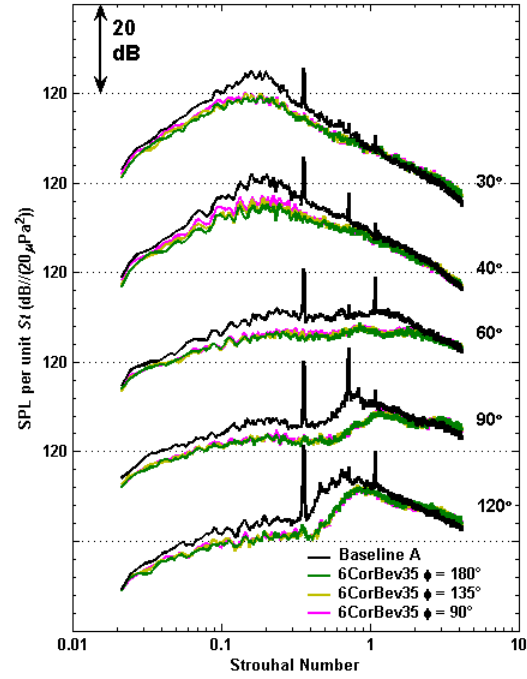


Figure 6.3: Spectra and *OASPL* Comparison of Cold jets, issuing from Md1.65 **6CorBev35** Nozzle from three azimuthal orientations on the short lip side, with $NPR = 3.05$, $M_j = 1.37$, $TTR = 1$, $D_{noz} = 0.708''$, $f_c = 24085$ Hz, Scaled $R/D_j = 100$

6.3.2 Heat Simulated Jets

The effects on the acoustics of heat-simulated jets issuing from a nozzle with a combination of a bevel and the hard wall interior corrugations are shown in Figure 6.4. Figure 6.4 shows the noise emitted from a jet issuing from this nozzle at an over-expanded pressure ratio of 3.0, and a *TTR* of 3.0. Four azimuthal orientations were tested and are shown in the *OASPL* plot, but for the ease of viewing, only 2 azimuthal orientations (the noise in the direction of the short lip and the long lip) are shown in the narrowband spectra. It can be seen that noise emitted from the short lip side ($\phi = 180^\circ$) differs from the noise emitted from the long lip side ($\phi = 0^\circ$) by a maximum of ~ 4 dB. However, the effect is the opposite of what was seen from the purely beveled nozzle where the noise from the long lip side is quietest in the peak noise emission direction, and different from cold jets from the 6CorBev35 nozzle seen previously. The design of the combination nozzle results in a large corrugation being present directly in line with the long lip side of the nozzle. It was seen in the 2Corrug nozzle the noise in plane with the corrugations was louder than out of plane, so a possible reason for the louder long lip side than short lip side is the size of the corrugation on the long lip side.

With the 6CorBev35 nozzle we see that the noise emitted in the peak noise direction (40° - 50°) is within ~ 1 dB at all azimuthal angles. Additionally, we can see that from polar angles 60° - 130° the short lip side is quieter than the long lip side, by as much as 3 dB at some polar angles.

Figure 6.5 shows a comparison between nozzles with different noise reduction techniques. The baseline nozzle, 6Corrug nozzle, the short lip side ($\phi = 180^\circ$) of the 6CorBev35 nozzle, and the short lip side of a purely beveled nozzle without corrugations are all shown. First we can see that the noise emitted from the 6CorBev35 nozzle is slightly louder than the 6Corrug nozzle at the very low aft angles (20° - 30°) and nearly equal at a polar angle of 40° . So the combination appears to mostly follow the 6Corrug nozzle at these angles. At intermediate polar angles from

50° -90° the 6CorBev35 nozzle emits almost exactly the same levels of noise as the purely beveled nozzle. Then at the forward and sideline polar angles there again is a switch and the 6CorBev35 nozzle is more like the 6Corrug nozzle.

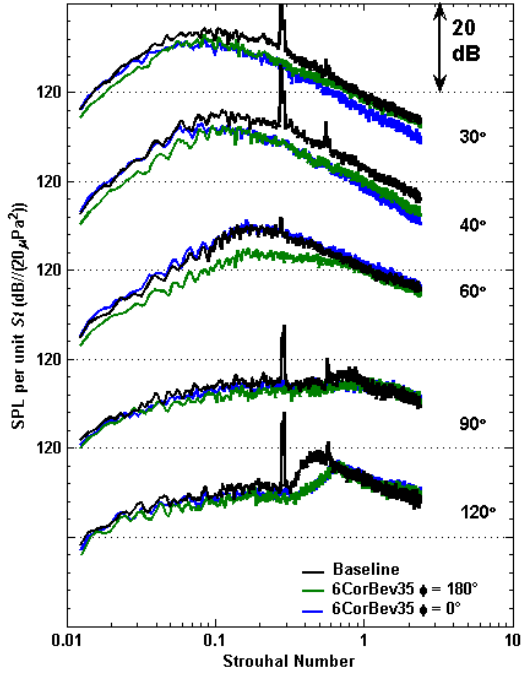


Figure 6.4: Spectra and OASPL Comparison of Heated jets, issuing from Md1.65 **6CorBev35** Nozzle, with $NPR = 3.0$, $M_j = 1.36$, $TTR = 3$, $D_{noz} = 0.708''$, $f_c = 41562$ Hz, Scaled $R/D_j = 100$

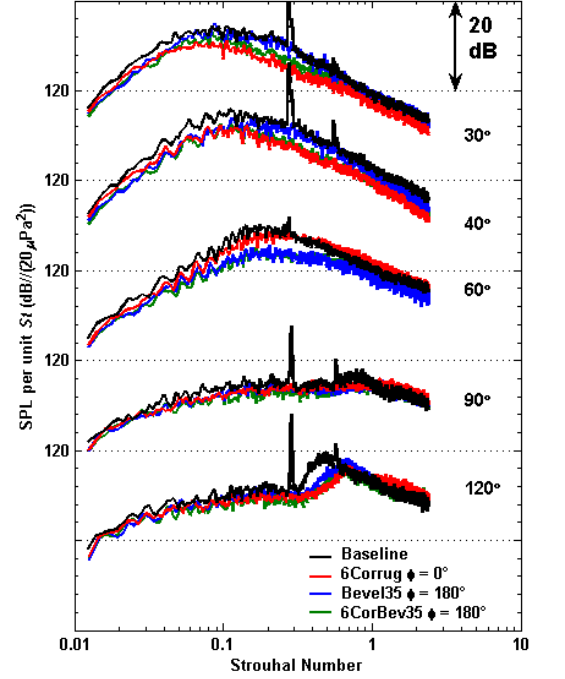


Figure 6.5: Spectra and OASPL Comparison of Heated jets, issuing from Md1.65 **6Corrug**, Md1.65 **Bevel35**, and Md1.65 **6CorBev35** Nozzles with $NPR = 3.0$, $M_j = 1.36$, $TTR = 3$, $D_{noz} = 0.708''$, $f_c = 41562$ Hz, Scaled $R/D_j = 100$

Figures 6.6 and 6.7 show the same comparison as the previous two figures, but for an increased NPR of 3.5, still with a TTR of 3.0. The same trends can be observed. The noise from the short lip side of the 6CorBev35 nozzle follows the noise from the short lip side of the purely beveled nozzle at angles from 50° - 90° (where Bev35 is quieter than 6Corrug) then follows the purely corrugated nozzle at all other polar angles (where 6Corrug is quieter than Bev35).

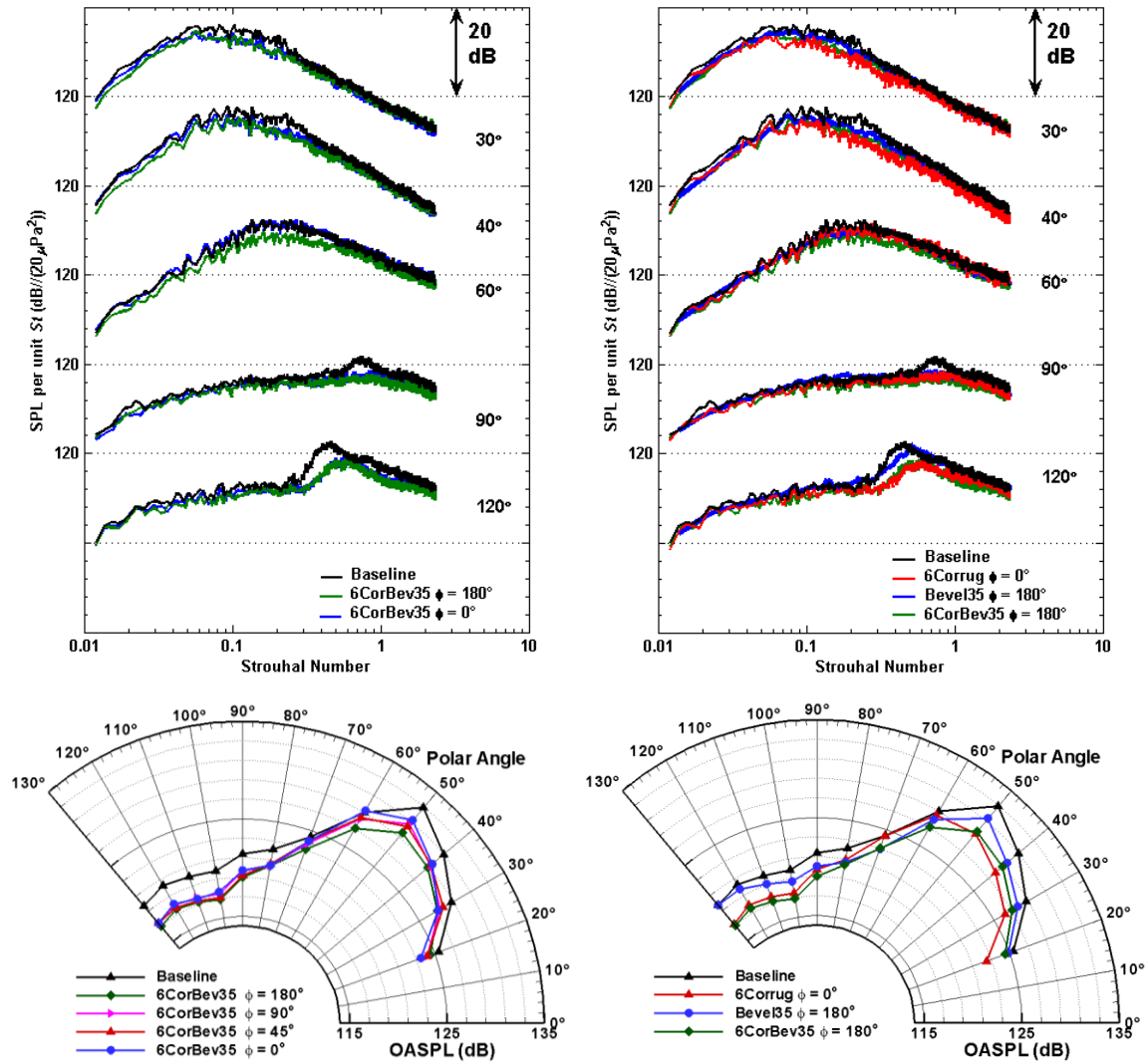


Figure 6.6: Spectra and OASPL Comparison of Heated jets, issuing from Md1.65 6CorBev35 Nozzle, with $NPR = 3.5$, $M_j = 1.47$, $TTR = 3$, $D_{noz} = 0.708''$, $f_c = 42735$ Hz, Scaled $R/D_j = 100$

Figure 6.7: Spectra and OASPL Comparison of Heated jets, issuing from Md1.65 6Corrug, Md1.65 Bevel35, and Md1.65 6CorBev35 Nozzles with $NPR = 3.5$, $M_j = 1.47$, $TTR = 3$, $D_{noz} = 0.708''$, $f_c = 42735$ Hz, Scaled $R/D_j = 100$

The remaining three figures show the delta *OASPL* in *dB* when compared to the baseline for different nozzles at three different jet conditions. The 6Corrug nozzle is compared to the 6CorBev35 nozzle at an azimuthal angle of $\phi = 0^\circ$ and $\phi = 180^\circ$. Figure 6.8 is for an over-expanded jet condition with an *NPR* of 3.0. The same results can be seen as observed before from Figure 6.5.

Looking at Figure 6.9 which is for an *NPR* of 3.5 we can see that the trends are all the same. The reductions across all polar angles are slightly less for this jet condition $\sim 2\text{-}3\text{ dB}$, but the noise of the 6CorBev35 nozzle as observed from the short lip side outperforms the 6Corrug nozzle at a majority of the polar angles.

Lastly, Figure 6.10 shows the same comparison for the slightly over-expanded *NPR* of 4.0. It can be seen that while the combination nozzle does not perform as well as the purely corrugated nozzle at the aft angles, the deficiency is made up for in the side and forward arc. In this region the 6Corrug nozzle increases noise from 1-2 *dB OASPL*, while the 6CorBev35 nozzle only has noise increases less than 0.5 *dB OASPL*.

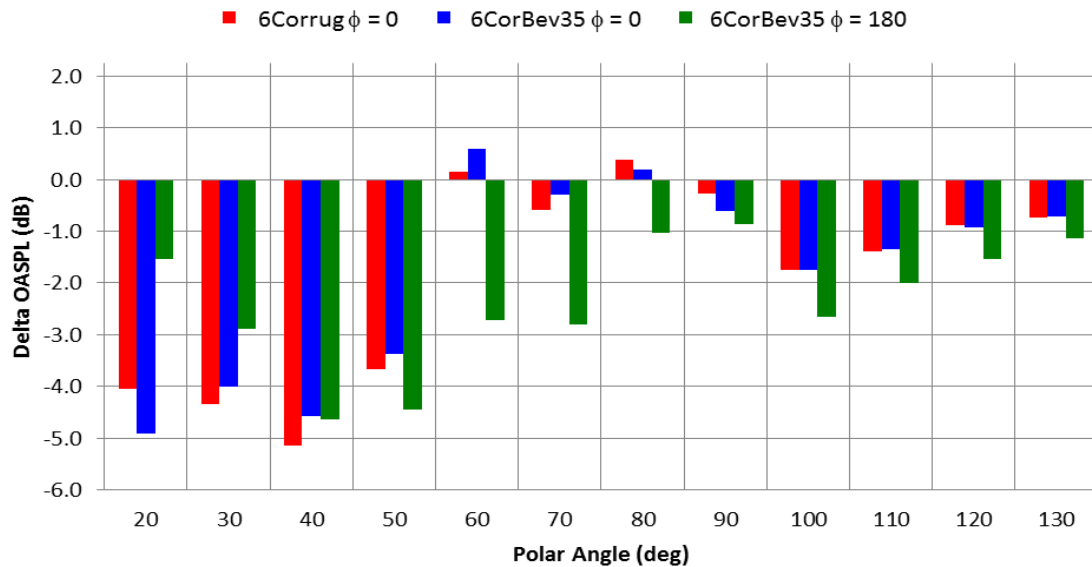


Figure 6.8: Delta *OASPL* Comparison for Different Nozzles, *NPR*= 3.0, $M_j = 1.36$, *TTR*= 3

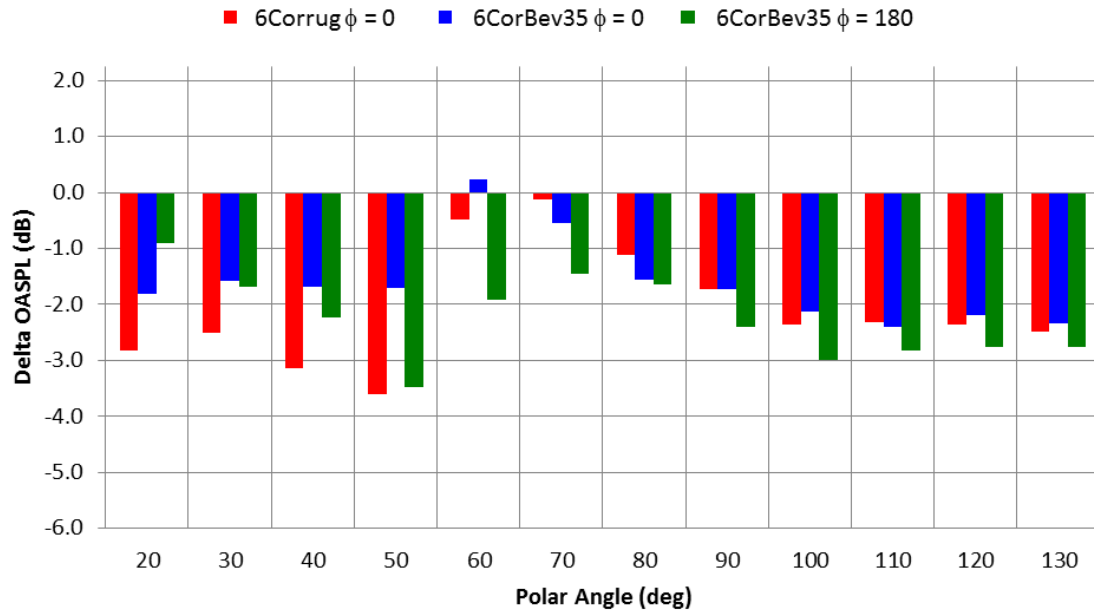


Figure 6.9: Delta *OASPL* Comparison for Different Nozzles, $NPR=3.5$, $M_j=1.47$, $TTR=3$

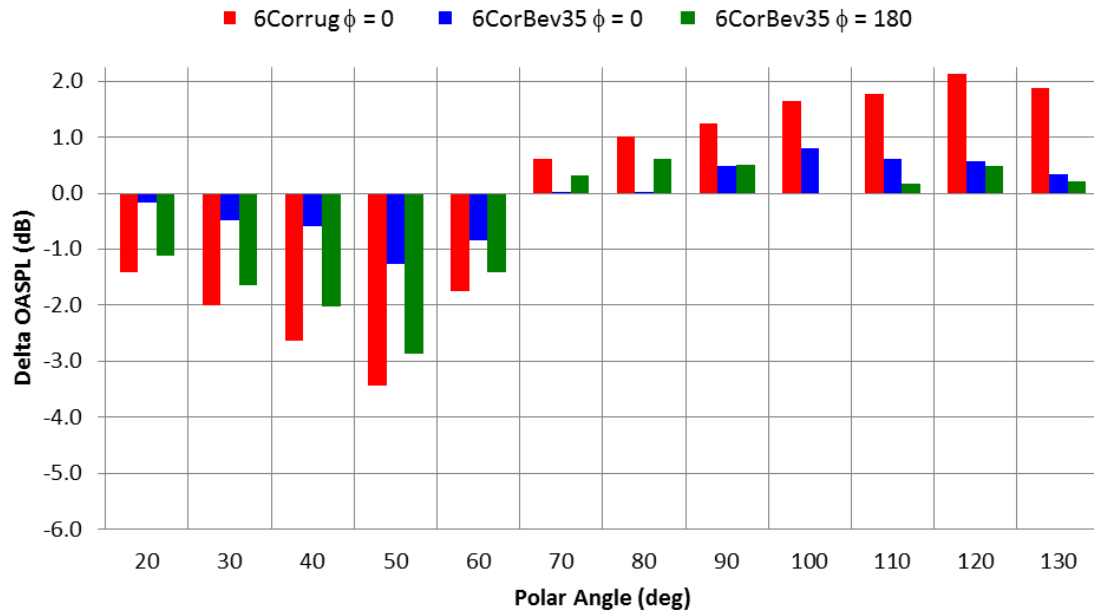


Figure 6.10: Delta *OASPL* Comparison for Different Nozzles, $NPR=4.0$, $M_j=1.56$, $TTR=3$

Chapter 7

Conclusions and Future Work

Acoustic measurements from small-scale heat simulated jets issuing from supersonic converging-diverging nozzles have been previously shown to compare very well to acoustic measurements from larger scale heated jets [2]. The extensive experience in this facility of comparing acoustic measurements with data from moderate scale (NASA size) experiments suggests that some of the detailed observations, particularly those with azimuthal variations, are not likely to be duplicated exactly at a larger scale. However, we expect the encouraging trends demonstrated in these present experiments to also be observed with larger models. A major goal is to extend the concepts to an aircraft scale.

7.1 Summary of Goals

The first part of this study examined the noise reduction potential of the concept of beveling the nozzle exit. Beveled exits for supersonic converging-diverging nozzles have only sparsely been explored. When using a new method of creating the nozzle exit bevel (which rotates the exit plane base on the center, thereby extending the bottom lip and shortening the top lip) the results show very good potential for noise reduction.

Another of the goals of this study was to better understand and develop the noise reduction potential of hard-wall corrugated nozzles as a preliminary step in our future plans to develop “fluidic corrugated” nozzles.

Finally, the combination of the supersonic converging-diverging beveled nozzle with the hard walled interior corrugations was examined, and proved to show very interesting results.

7.2 Major Results

The deflection angle of the jet plumes issuing from supersonic converging-diverging beveled nozzles is very small ($<5^\circ$). This, in conjunction with other experimental thrust measurements[43] results in the conclusion that the thrust is affected only in a minor way by the nozzle beveled exit.

For over-expanded jets without forward flight there is a noise reduction of ~ 4 dB on the long lip side in the peak noise emission direction; for nearly perfectly expanded jets there is a noise reduction of ~ 3 dB. In addition, the short lip side does not show an increase in noise of the same magnitude as the reduction on the long lip side. The *BBSAN* is affected very little for the over-expanded jets, whereas there is a noticeable rise in the peak of the *BBSAN* for the nearly perfectly expanded jets due to the presence of stronger shock cells.

The noise field produced by supersonic converging-diverging beveled nozzles appears to be at a minimum on the long lip side then approaches the baseline noise levels when an azimuthal angle of 45° is reached. The noise then increases at an angle of 90° , then decreases back down to baseline levels on the short lip side. Assuming the long lip side would be oriented in the downward direction on an aircraft, such nozzles would produce a modest noise reduction for very little thrust loss penalty.

The presence of a forward flight stream did not negatively affect the noise reduction seen on the long lip side of the beveled nozzle. Similar magnitudes of reduction were seen as in the static tests.

The noise emitted from nozzles with both two corrugations and three corrugations has a high azimuthal directivity due to the reshaping of the jet plume. When the amount of corrugations is increased to six, there is a weak variation in the azimuthal directivity. The corrugations can reduce the noise by as much as ~ 4 dB in the peak noise emission direction (at low polar angles).

Additionally, when operated at the optimal nozzle pressure ratio so the effective nozzle area causes the flow to be perfectly expanded, noise reductions of 2-4 *dB* were observed at the sideline polar angles. From examining the shadowgraphs of the jets issuing from these hard walled corrugation nozzles it can be seen that the corrugations significantly affect both the mixing shear layer and the shock structure of the jet.

The combination of the supersonic bevel and interior hard wall corrugations that extend all the way to the nozzle exit was examined for the first time. The combination nozzle showed only a slight azimuthal directivity. On the short lip side the combination nozzle seemed to maximize the noise reduction by following trends of the purely beveled nozzle at intermediate polar angles (50° - 90°) and following the trends of the nozzle with only corrugations at the low polar angles and the forward polar angles. While the combination of the bevel and the interior hard walled corrugations did not result in purely additive noise reduction, the acoustic field had better performance over a wider range of polar angles and jet conditions than either the purely beveled nozzle or the purely corrugated nozzle.

7.3 Future Work

Future Experiments

The research within this thesis presented an in depth analysis of the effect of supersonic beveled exits and interior hard walled corrugations and the combination of the two methods. However, the studies were in no way comprehensive, as only one of each the baseline nozzle Mach number and corrugation design were explored. Future work could involve the analysis of other nozzle design area ratios, and shapes, along with other corrugation design conditions to further understand the effects of the small scale Reynolds number on the boundary layer within the nozzle. Additionally, pitot rake measurements are planned to measure the mean flow

properties, which will provide another direct quantitative comparison to the fluidic corrugations for the facilitation of their design.

In addition to more design parameters and nozzle conditions, several other ideas have stemmed from this study. Future experiments could explore the use of a small number of corrugations to reshape the jet plume as was seen with two and three corrugations. The azimuthal directivity of the noise field could be used if implemented correctly to reduce noise seen on the ground. Also, the noise in plane with the corrugations was seen to increase, therefore future work could examine a combination nozzle which either has the corrugations on different facets such that one isn't directly in line with the long lip, or the area of the corrugation during the extension of the long lip could be calculated with a different approach such that it wasn't so large at the nozzle exit.

Future Numerical Simulations

A significant component in the Penn State noise reduction methodology development is the advanced numerical simulations led by Professor P. J. Morris. Besides the flow field characteristics, these simulations will perform estimates of the net thrust of variations on the nozzle corrugations. Additionally, we expect estimates of the noise reduction capabilities of various designs to provide guidance for new developments.

Bibliography

- [1] Lighthill, M. J., "On sound generated aerodynamically. I. General theory," *Proceedings of the Royal Society of London. Series A, Mathematical and Physical Sciences*, Vol. 211, No. 1107, 1952, pp. 564-587.
- [2] Lighthill, M. J., "On sound generated aerodynamically. II. Turbulence as a source of sound," *Proceedings of the Royal Society of London. Series A, Mathematical and Physical Sciences*, Vol. 222, No. 1148, 1954, pp. 1-32.
- [3] Ffowcs-Williams, J. E., "The noise from turbulence convected at a high-speed," *Philos. Trans. Roy Soc. London Ser. A*, Vol. 255, 1963, pp. 469-503.
- [4] G. M. Lilley, "Jet Noise Classical Theory and Experiments," in *Aeroacoustic of Flight Vehicles: Theory and Practice- Volume 1: Noise Sources*, H. H. Hubbard, Ed.: NASA Reference Publication 1258, WRDC Technical Report 90-3052, 1991, Aug. 1991, pp. 211-289.
- [5] Crow, S. C., and Champagne, F. H., "Orderly structure in jet turbulence," *Journal of Fluid Mechanics*, Vol. 48, No. 3, 1971, pp. 547-591.
- [6] Winant, C. D., and Browand, F. K., "Vortex pairing: the mechanism of turbulent mixing-layer growth at moderate Reynolds number," *Journal of Fluid Mechanics*, Vol. 63, No. 2, 1974, pp. 237-255.
- [7] Brown, G. L., and Roshko, A., "On density effects and large structure in turbulent mixing layers," *Journal of Fluid Mechanics*, Vol. 64, No. 4, 1974, pp. 775-816.
- [8] Tam, C. K. W., Golebiowski, M., and Seiner, J. M., "On the Two Components of Turbulent Mixing Noise From Supersonic Jets," AIAA Paper No. 96-1716, 1996.
- [9] Krothapalli, A., Arakeri, V., and Greska B., "Mach wave radiation: a review and an extension," AIAA Paper No. 2003-1200, 2003.
- [10] Tam, C. K. W., and Morris, P. J., "The radiation of sound by the instability waves of a compressible plane turbulent shear layer," *Journal of Fluid Mechanics*, Vol. 98, 1980, pp. 349-381.
- [11] Morris, P. J., and Tam, C. K. W., "On the radiation of sound by the instability waves of a compressible axisymmetric jet," in *Mechanics of Sound Generation in Flows, Proceedings of the Joint Symposium*, Goettingen, West Germany, Berlin, Springer-Verlag, 1979, August 28-31, 1979, pp. 55-61.
- [12] Tam, C. K. W., and Burton, D. E., "Sound generated by instability waves of supersonic flows. Part 2. Axisymmetric jets," *Journal of Sound and Vibration*, Vol. 65, No. 2, 1984, pp. 273-295.
- [13] McLaughlin, D. K., Morrison, G. L., and Troutt, T. R., "Experiments on the instability waves in a supersonic jet and their acoustic radiation," *Journal of Fluid Mechanics*, Vol. 69, No. 1, 1975.
- [14] Morrison, G. L., and McLaughlin, D. K., "The noise generation by

- instabilities in low Reynolds number supersonic jets," *Journal of Sound and Vibration*, Vol. 65, No. 2, 1979, pp. 177-191.
- [15] Troutt, T. R. and McLaughlin, D. K., "Experiments on the flow and acoustic properties of a moderate-Reynolds-number supersonic jet," *Journal of Fluid Mechanics*, Vol. 116, 1982, pp. 123-156.
 - [16] Veltin, J., Day, B. J., and McLaughlin, D. K., "Correlation of Flowfield and Acoustic Field Measurements in High Speed jets," *AIAA Journal*, Vol. 49, No. 1, 2011, pp. 150-163.
 - [17] Harper-Bourne, M. and Fisher, M.J., "The Noise from Shock Waves in Supersonic Jets," in *Proceedings of the AGARD Conference on Noise Mechanisms, No. 131*, Brussels, Belgium, 1973.
 - [18] Miller, S. A. E., and Morris, P. J., "The Prediction of Broadband Shock-Associated Noise Including Propagation Effects," AIAA Paper No. 2011-2923, 2011.
 - [19] Kuo, C. -W., McLaughlin, D. K., and Morris, P. J., "Effects of Supersonic Jet Conditions on Broadband Shock-Associated Noise," AIAA Paper No. 2011-1032, 2011.
 - [20] Seiner, J. M., "Advances in high speed jet Aeroacoustics," AIAA Paper No. 84-2275, 1984.
 - [21] Shen, H. and Tam, C.K.W., "The effects of jet temperature and nozzle lip thickness on screech tones," AIAA Paper No. 1999-1860, 1999.
 - [22] Panda, J., "An Experimental Investigation of Screech Noise Generation," *Journal of Fluid Mechanics*, Vol. 378, 1999, pp. 71-96.
 - [23] Norum, T. D., "Screech suppression in supersonic jets," *AIAA Journal*, Vol. 21, No. 2, 1983, pp. 235-240.
 - [24] Raman, G., "Cessation of screech in underexpanded jets," *Journal of Fluid Mechanics*, Vol. 336, 1997, pp. 69-90.
 - [25] Seiner, J. M., Ukeiley, L. S., and Jansen, B. J., "Aero-Performance Efficient Noise Reduction for the F404-400 Engine," AIAA Paper No. 2005-3048, 2005.
 - [26] Seiner, J. M., Jansen, B. J., Ukeiley, L. S., "Acoustic Fly-Over Studies of F/A E/F Aircraft During FCLP Mission," AIAA Paper No. 2003-3330, 2003.
 - [27] Viswanathan, K., "Does a Model-Scale Nozzle Emit the Same jet Noise as a Jet Engine?," *AIAA Journal*, Vol. 46, No. 2, 2008, pp. 336-355.
 - [28] Kuo, C.-W., Veltin, J., and McLaughlin, D. K., "Acoustic measurements of models of military style supersonic nozzle jets," AIAA Paper No. 2009-18, 2009.
 - [29] Kuo, C.-W., Veltin, J., and McLaughlin, D. K., "Methods to improve the accuracy of acoustic measurements in small scale high speed jets," AIAA Paper No. 2009-3251, 2009.
 - [30] McLaughlin, D. K., Bridges, J., and Kuo, C.-W., "On the scaling of small, heat simulated jet noise measurements to moderate size exhaust jets," *International Journal of Aeroacoustics*, Vol. 9, No. 4&5, 2010, pp. 627-654.
 - [31] Ponton, M. K., and Seiner, J. M., "The effects of nozzle exit lip thickness on plume resonance," *Journal of Sound and Vibration*, Vol. 154, No. 3, 1992, pp.

531-549.

- [32] Papamoschou, D. and Debiasi, M., "Noise measurements in supersonic jets treated with the Mach wave elimination method," *AIAA Journal*, Vol. 37, No. 2, 1999, pp. 154-160.
- [33] Koch, L. D., Bridges, J., Brown, C., and Khavaran, A., "Experimental and analytical determination of the geometric far field for round jets," *Noise Control Engineering Journal*, Vol. 53, No. 1, 2005, pp. 20-28.
- [34] Viswanathan, K., "Instrumentation considerations for accurate jet noise measurements," *AIAA Journal*, Vol. 44, No. 6, 2006, pp. 1137-1149.
- [35] Nagamatsu, H. T., Sheer, R. E., and Horvay, G., "Supersonic jet noise theory and experiments," in *Basic aerodynamic noise research NASA SP-20*, Washington, D. C., July 14-15, 1969.
- [36] Kuo, C. -W., "Extending Acoustic Data Measured with Small-Scale Supersonic Model Jets to Practical Aircraft Exhaust Jets," *Ph. D. Thesis, The Pennsylvania State University, University Park, PA*, 2010.
- [37] Goss, A. E., Veltin, J., Lee, J., and McLaughlin, D. K., "Acoustic measurements of high-speed jets from rectangular nozzle with thrust vectoring," *AIAA Journal*, Vol. 47, No. 9, 2009, pp. 1482-1490.
- [38] Henderson, B., and Bridges, J., "An MDOE Investigation of Chevrons for Supersonic Jet Noise Reduction," AIAA Paper No. 2010-3926, 2010.
- [39] Schlinker, R. H., Simonich, J. C., Shannon, D. W., Reba, R. A., Colonius, T., Gudmunsson, K., and Ladeinde, F., "Supersonic Jet Noise from Round and Chevron Nozzles: Experimental Studies," AIAA Paper No. 2009-3257, 2009.
- [40] Kuo, C.-W., Veltin, J., and McLaughlin, D. K., "Advanced acoustic assesment of small-scale military-style nozzles with chevrons," AIAA Paper No. 2010-3923, 2010.
- [41] Martens, S. and Spyropoulos, J. T., "Practical Jet Noise Reduction for Tactical Aircraft," in *Proceedings of the ASME Turbo Expo 2010: Power for Land, Sea and Air*, GT2010-23699, Glasgow, UK, 2010, June 14-18, 2010.
- [42] Martens, S., Spyropoulos, J. T., and Nagel, Z., "The Effect of Chevrons on Crackle - Engine and Scale Model Results," in *Proceedings of the ASME Turbo Expo 2011: Power for Land, Sea and Air*, GT2011-46417, Vancouver, Canada, 2011, June 6-10, 2011.
- [43] Viswanathan, K., and Czech, M. J., "Adaptation of the Beveled Nozzle for High speed jet Noise Reduction," *AIAA Journal*, Vol. 49, No. 5, 2011, pp. 932-944, 2010-654.
- [44] Seiner, J. M., Ukeiley, L. S., Jansen, B. J., Kannepalli, C., and Dash, S., "Noise Reduction Technology for F/A-18 E/F Aircraft," AIAA Paper No. 2004-2972, 2004.
- [45] Kuo, C. -W., Morris, P., and McLaughlin, D. K., "Noise Reduction in Supersonic Jets by Nozzle Fluidic Inserts," AIAA Paper No. 2012-XXXX to be presented at the AIAA Aeroacoustics Conference, Colorado Springs, CO, 2012.
- [46] Doty, M. J., "An Experimental Investigation of the Aeroacoustic Properties of High-Speed, Helium/Air Mixture Axisymmetric Jets," *Ph. D. Thesis, The*

Pennsylvania State University, University Park, PA, 2002.

- [47] Veltin, J., "On the Characterization of Noise Sources in Supersonic Shock Containing Jets," *Ph. D. Thesis, The Pennsylvania State University, University Park, PA*, 2008.
- [48] Kinzie, K. W., McLaughlin, D. K., "Measurements of Supersonic Helium/Air Mixture Jets," *AIAA Journal*, Vol. 37, No. 11, 1999, pp. 1363-1369.
- [49] Doty, M. J., McLaughlin, D.K., "Acoustic and mean flow measurements of high-speed, helium-air mixture jets," *International Journal of Aeroacoustics*, Vol. 2, No. 2, 2003, pp. 293-334.
- [50] Papamoschou, D., "Acoustic Simulation of Coaxial Hot Air Jets Using Cold Helium-Air Mixture Jets," *Journal of Propulsion and Power*, Vol. 23, No. 2, 2007, pp. 375-381.
- [51] Miller, S. and Veltin, D., "Experimental and numerical investigation of flow properties of supersonic helium-air jets," *AIAA Paper No. 2010-471*, 2010.
- [52] Viswanathan, K., and Czech, M. J., "Measurement and Modeling of Effect of Forward Flight on Jet Noise," *AIAA Journal*, Vol. 49, No. 1, 2011, pp. 216-234.
- [53] Veltin, J., Day, B. J., and McLaughlin, D. K., "Forward Flight Effect on Small Scale Supersonic Jet Acoustics," *AIAA Paper No. 2010-3924*, 2010.
- [54] Settles, G. S., *Schlieren and Shadowgraph Techniques*, Corrected ed.: Spring, 2001.
- [55] J. M. Seiner, "Method and device for reducing engine noise," *USA Patent US 7,475,550 B2*, January 13, 2009.
- [56] Argrow, B. M. and Emanuel, G., "Comparison of Minimum Length Nozzles," *Journal of Fluids Engineering*, Vol. 110, 1988, pp. 283-288.
- [57] Behera, B. and Srinivasan, K., "Design Methods for Axisymmetric Supersonic Nozzle Contours," *International Journal of Turbo and Jet Engines*, Vol. 24, No. 2, 2007, pp. 115-117.
- [58] Petitjean, B. P., Viswanathan, K., McLaughlin, D. K., and Morris, P. J., "Space-time correlation measurements in subsonic and supersonic jets using optical deflectometry," *AIAA Paper No. 2007-3613*, 2007.
- [59] Viswanathan, K., Krothapalli, A., Seiner, J. M., Czech, M. J., Greska, B., and Jansen, B. J., ""Assessment of Low-Noise Nozzle Designs for Fighter Aircraft Applications," *AIAA Journal*, Vol. 48, No. 2, 2011, pp. 412-423.

Appendix

Processing Codes

Two computer programs and their sub functions are included. The processing codes for the creation of the axisymmetric Method of Characteristics nozzle shape, MOC_GUI_V1.m, MOC_Axi_twoInsidePointsf2.m, MOC_Axi_KnownFlow2.m, MOC_Axi_Nozzle_Design_V_2.m, and the Schlieren/Shadowgraph processing code, AverageFolderofImages_vE.m, FingerPrintRemoval_vE.m, PostProcessing_vE.m, and ProcessMightexVideo_vE.m. Other processing codes were used; however they have been covered in previous Thesis mentioned in this study.

MOC_GUI_V1.m

```
function varargout = MOC_GUI_V1(varargin)
% MOC_GUI_V1 MATLAB code for MOC_GUI_V1.fig
%     MOC_GUI_V1, by itself, creates a new MOC_GUI_V1 or raises the
existing
%     singleton*.
%
%     H = MOC_GUI_V1 returns the handle to a new MOC_GUI_V1 or the
handle to
%     the existing singleton*.
%
%     MOC_GUI_V1('CALLBACK',hObject,eventData,handles,...) calls the
local
%     function named CALLBACK in MOC_GUI_V1.M with the given input
arguments.
%
%     MOC_GUI_V1('Property','Value',...) creates a new MOC_GUI_V1 or
raises the
%     existing singleton*. Starting from the left, property value
pairs are
%     applied to the GUI before MOC_GUI_V1_OpeningFcn gets called. An
%     unrecognized property name or invalid value makes property
application
%     stop. All inputs are passed to MOC_GUI_V1_OpeningFcn via
varargin.
%
%     *See GUI Options on GUIDE's Tools menu. Choose "GUI allows only
one
%     instance to run (singleton)".
%
% See also: GUIDE, GUIDATA, GUIHANDLES
```

```

% Edit the above text to modify the response to help MOC_GUI_V1

% Last Modified by GUIDE v2.5 10-Oct-2011 16:07:34

% Begin initialization code - DO NOT EDIT
gui_Singleton = 1;
gui_State = struct('gui_Name',       mfilename, ...
                  'gui_Singleton',   gui_Singleton, ...
                  'gui_OpeningFcn',   @MOC_GUI_V1_OpeningFcn, ...
                  'gui_OutputFcn',    @MOC_GUI_V1_OutputFcn, ...
                  'gui_LayoutFcn',    [], ...
                  'gui_Callback',     []);
if nargin && ischar(varargin{1})
    gui_State.gui_Callback = str2func(varargin{1});
end

if nargout
    [varargout{1:nargout}] = gui_mainfcn(gui_State, varargin{:});
else
    gui_mainfcn(gui_State, varargin{:});
end
% End initialization code - DO NOT EDIT


% --- Executes just before MOC_GUI_V1 is made visible.
function MOC_GUI_V1_OpeningFcn(hObject, eventdata, handles, varargin)
% This function has no output args, see OutputFcn.
% hObject    handle to figure
% eventdata  reserved - to be defined in a future version of MATLAB
% handles     structure with handles and user data (see GUIDATA)
% varargin   command line arguments to MOC_GUI_V1 (see VARARGIN)

% Choose default command line output for MOC_GUI_V1
handles.output = hObject;

% Update handles structure
guidata(hObject, handles);

% UIWAIT makes MOC_GUI_V1 wait for user response (see UIRESUME)
% uiwait(handles.figure1);


% --- Outputs from this function are returned to the command line.
function varargout = MOC_GUI_V1_OutputFcn(hObject, eventdata, handles)
% varargout  cell array for returning output args (see VARARGOUT);
% hObject    handle to figure
% eventdata  reserved - to be defined in a future version of MATLAB
% handles     structure with handles and user data (see GUIDATA)

% Get default command line output from handles structure

```



```

varargout{1} = handles.output;

% --- Executes on selection change in ParamBox.
function ParamBox_Callback(hObject, eventdata, handles)
% hObject      handle to ParamBox (see GCBO)
% eventdata    reserved - to be defined in a future version of MATLAB
% handles      structure with handles and user data (see GUIDATA)

% Hints: contents = cellstr(get(hObject,'String')) returns ParamBox
% contents as cell array
%          contents{get(hObject,'Value')} returns selected item from
%          ParamBox

% --- Executes during object creation, after setting all properties.
function ParamBox_CreateFcn(hObject, eventdata, handles)
% hObject      handle to ParamBox (see GCBO)
% eventdata    reserved - to be defined in a future version of MATLAB
% handles      empty - handles not created until after all CreateFcns
% called

% Hint: listbox controls usually have a white background on Windows.
%          See ISPC and COMPUTER.
if ispc && isequal(get(hObject,'BackgroundColor'),
get(0,'defaultUicontrolBackgroundColor'))
    set(hObject,'BackgroundColor','white');
end
set(hObject, 'Value', 1);

function ThetaStar_Callback(hObject, eventdata, handles)
% hObject      handle to ThetaStar (see GCBO)
% eventdata    reserved - to be defined in a future version of MATLAB
% handles      structure with handles and user data (see GUIDATA)

% Hints: get(hObject,'String') returns contents of ThetaStar as text
%          str2double(get(hObject,'String')) returns contents of
%          ThetaStar as a double

% --- Executes during object creation, after setting all properties.
function ThetaStar_CreateFcn(hObject, eventdata, handles)
% hObject      handle to ThetaStar (see GCBO)
% eventdata    reserved - to be defined in a future version of MATLAB
% handles      empty - handles not created until after all CreateFcns
% called

% Hint: edit controls usually have a white background on Windows.
%          See ISPC and COMPUTER.

```

```

if ispc && isequal(get(hObject,'BackgroundColor'),
get(0,'defaultUicontrolBackgroundColor'))
    set(hObject,'BackgroundColor','white');
end

```

```

function height_Callback(hObject, eventdata, handles)
% hObject      handle to height (see GCBO)
% eventdata    reserved - to be defined in a future version of MATLAB
% handles      structure with handles and user data (see GUIDATA)

% Hints: get(hObject,'String') returns contents of height as text
%         str2double(get(hObject,'String')) returns contents of height
as a double

```

```

% --- Executes during object creation, after setting all properties.
function height_CreateFcn(hObject, eventdata, handles)
% hObject      handle to height (see GCBO)
% eventdata    reserved - to be defined in a future version of MATLAB
% handles      empty - handles not created until after all CreateFcns
called

```

```

% Hint: edit controls usually have a white background on Windows.
%         See ISPC and COMPUTER.
if ispc && isequal(get(hObject,'BackgroundColor'),
get(0,'defaultUicontrolBackgroundColor'))
    set(hObject,'BackgroundColor','white');
end

```

```

function numC_Callback(hObject, eventdata, handles)
% hObject      handle to numC (see GCBO)
% eventdata    reserved - to be defined in a future version of MATLAB
% handles      structure with handles and user data (see GUIDATA)

% Hints: get(hObject,'String') returns contents of numC as text
%         str2double(get(hObject,'String')) returns contents of numC as
a double

```

```

% --- Executes during object creation, after setting all properties.
function numC_CreateFcn(hObject, eventdata, handles)
% hObject      handle to numC (see GCBO)
% eventdata    reserved - to be defined in a future version of MATLAB
% handles      empty - handles not created until after all CreateFcns
called

```

```

% Hint: edit controls usually have a white background on Windows.

```

```

%       See ISPC and COMPUTER.
if ispc && isequal(get(hObject,'BackgroundColor'),
get(0,'defaultUicontrolBackgroundColor'))
    set(hObject,'BackgroundColor','white');
end

function gamma_Callback(hObject, eventdata, handles)
% hObject      handle to gamma (see GCBO)
% eventdata    reserved - to be defined in a future version of MATLAB
% handles      structure with handles and user data (see GUIDATA)

% Hints: get(hObject,'String') returns contents of gamma as text
%         str2double(get(hObject,'String')) returns contents of gamma as
a double

% --- Executes during object creation, after setting all properties.
function gamma_CreateFcn(hObject, eventdata, handles)
% hObject      handle to gamma (see GCBO)
% eventdata    reserved - to be defined in a future version of MATLAB
% handles      empty - handles not created until after all CreateFcns
called

% Hint: edit controls usually have a white background on Windows.
%       See ISPC and COMPUTER.
if ispc && isequal(get(hObject,'BackgroundColor'),
get(0,'defaultUicontrolBackgroundColor'))
    set(hObject,'BackgroundColor','white');
end

function radC_Callback(~, eventdata, handles)
% hObject      handle to radC (see GCBO)
% eventdata    reserved - to be defined in a future version of MATLAB
% handles      structure with handles and user data (see GUIDATA)

% Hints: get(hObject,'String') returns contents of radC as text
%         str2double(get(hObject,'String')) returns contents of radC as
a double

% --- Executes during object creation, after setting all properties.
function radC_CreateFcn(hObject, eventdata, handles)
% hObject      handle to radC (see GCBO)
% eventdata    reserved - to be defined in a future version of MATLAB
% handles      empty - handles not created until after all CreateFcns
called

```

```

% Hint: edit controls usually have a white background on Windows.
% See ISPC and COMPUTER.
if ispc && isequal(get(hObject,'BackgroundColor'),
get(0,'defaultUicontrolBackgroundColor'))
    set(hObject,'BackgroundColor','white');
end

% --- Executes on button press in createNoz.
function createNoz_Callback(hObject, eventdata, handles)
% hObject      handle to createNoz (see GCBO)
% eventdata    reserved - to be defined in a future version of MATLAB
% handles      structure with handles and user data (see GUIDATA)
%plotting routines
cd 'Two-Dimensional Code (Axi)'
global gamma r r0 Mach pop0 tot0 rhorh0 theta nu xT rT xW rW MachT info
pA pB lengthJ;
gamma = str2double(get(handles.gamma,'String'));
num_C = str2double(get(handles.numC,'String'));
MachEx = str2double(get(handles.ThetaStar,'String'));
radC = str2double(get(handles.radC,'String'));
point_Num = num_C*(num_C+1)/2;
clc
[r, r0, pA, pB, Mach, pop0, tot0, rhorh0, nu, theta,
info, xT, rT, xW, rW, lengthJ, MachT] = MOC_Axi_Nozzle_Design_V_1(MachEx,
num_C, radC);
if info == Inf
    msgbox('Note: The Expansion section is too large, the reflecting
waves intersect the wall before it is done expanding. This is beyond
the scope of this program. Please either decrease the radius of
expansion, or increase the initial flow angle.','Error');
    cla(handles.MOCChart,'reset');
else
    nozColors = [0 0 0; 0 0 1; 0 0.498039215803146 0; 1 0 0; 0 0 0.5];
    cla(handles.MOCChart,'reset');
    cla(handles.FluidGraph,'reset');
    axes(handles.MOCChart);
    hold on;
    plot([r0(1,1) r0(1,1)], [0, r0(1,2)], 'Color', nozColors(1,:));
    plot(r0(:,1), r0(:,2), 'Color', nozColors(3,:), 'LineWidth', 1.5);
    plot([r0(1,1) r(1,1)], [r0(1,2) r(1,2)], 'Color', nozColors(2,:),
'LineWidth', 1);
    plot([r0(1,1) r(1,1)], [0 r(1,2)], 'Color', nozColors(1,:),
'LineWidth', 1);
    for i = 2:num_C
        plot([r0(i,1) r(i,1)], [r0(i,2) r(i,2)], 'Color', nozColors(2,:),
'LineWidth', 1);
        plot([r(i-1,1) r(i,1)], [r(i-1,2) r(i,2)], 'Color', nozColors(2,:),
'LineWidth', 1);
    end
    % plot([r(num_C,1) r(num_C+1,1)], [r(num_C,2)
r(num_C+1,2)], 'Color', nozColors(2,:), 'LineWidth', 1);
    for p = num_C+1:point_Num

```

```

        if info(p) == 0
            plot([r(pA(p),1) r(p,1)], [r(pA(p),2)
r(p,2)], 'Color', nozColors(2,:), 'LineWidth', 1);
            plot([r(pB(p),1) r(p,1)], [r(pB(p),2)
r(p,2)], 'Color', nozColors(2,:), 'LineWidth', 1);
        elseif info(p) == 1
            plot([r(pA(p),1) r(p,1)], [r(pA(p),2)
r(p,2)], 'Color', nozColors(2,:), 'LineWidth', 1);
            plot([r(pB(p),1) r(p,1)], [r(pB(p),2)
r(p,2)], 'Color', nozColors(1,:), 'LineWidth', 1);
        end
    end

    numJ = size(xT,2);
    for j = 2:numJ
        plot([xT(1,j) xT(1,j-1)], [rT(1,j) rT(1,j-
1)], 'Color', nozColors(5,:), 'LineWidth', 1)
        for i = 2:lengthJ(j)
            plot([xT(i,j) xT(i-1,j)], [rT(i,j) rT(i-
1,j)], 'Color', nozColors(5,:), 'LineWidth', 1)
            plot([xT(i,j) xT(i,j-1)], [rT(i,j) rT(i,j-
1)], 'Color', nozColors(5,:), 'LineWidth', 1)
        end
    end
    plot(xW,rW, 'Color', nozColors(4,:), 'LineWidth', 1.5)

    axis equal;
    MachEnd = MachT(1,1);
    rFromMach = sqrt(rW(1)^2*1/MachEnd*(2/(gamma+1)*(1+(gamma-
1)/2*MachEnd^2))^( (gamma+1)/(2*(gamma-1)) ));
    perError = abs((rFromMach^2-rW(end)^2)/rFromMach^2)*100;
    [MachIdeal, ~,~,~,~] =
flowisentropic(gamma,rW(end)^2/rW(1)^2, 'sup');
    perError2 = abs((MachIdeal-MachEnd)/MachIdeal)*100;

    set(handles.AreaRatio, 'String', num2str(rW(end)^2/rW(1)^2));
    set(handles.PercentError, 'String', num2str(perError2));
    set(handles.MachNumber, 'String', num2str(MachEnd));
    set(handles.KernalLength, 'String', num2str(r(end,1)));
    set(handles.NoZLength, 'String', num2str(xW(end)));
end
cd ..

% --- If Enable == 'on', executes on mouse press in 5 pixel border.
% --- Otherwise, executes on mouse press in 5 pixel border or over
createNoz.
function createNoz_ButtonDownFcn(hObject, eventdata, handles)
% hObject    handle to createNoz (see GCBO)
% eventdata  reserved - to be defined in a future version of MATLAB
% handles    structure with handles and user data (see GUIDATA)

```

```

% --- Executes on button press in ExportPoints.
function ExportPoints_Callback(hObject, eventdata, handles)
% hObject      handle to ExportPoints (see GCBO)
% eventdata    reserved - to be defined in a future version of MATLAB
% handles      structure with handles and user data (see GUIDATA)

% --- Executes on button press in ExportMOC.
function ExportMOC_Callback(hObject, eventdata, handles)
% hObject      handle to ExportMOC (see GCBO)
% eventdata    reserved - to be defined in a future version of MATLAB
% handles      structure with handles and user data (see GUIDATA)
newFig = figure;
global gamma r r0 Mach pop0 tot0 rhorr0 theta nu xT rT xW rW MachT info
pA pB lengthJ;
gamma = str2double(get(handles.gamma, 'String'));
num_C = str2double(get(handles.numC, 'String'));
MachEx = str2double(get(handles.ThetaStar, 'String'));
radC = str2double(get(handles.radC, 'String'));
point_Num = num_C*(num_C+1)/2;
clc
    nozColors = [0 0 0; 0 0 1; 0 0.498039215803146 0; 1 0 0; 0 0 0.5];
    hold on;
    plot([r0(1,1) r0(1,1)], [0, r0(1,2)], 'Color', nozColors(1,:));
    plot(r0(:,1), r0(:,2), 'Color', nozColors(3,:), 'LineWidth', 1.5);
    plot([r0(1,1) r(1,1)], [r0(1,2) r(1,2)], 'Color', nozColors(2,:),
'LineWidth', 1);
    plot([r0(1,1) r(1,1)], [0 r(1,2)], 'Color', nozColors(1,:),
'LineWidth', 1);
    for i = 2:num_C
        plot([r0(i,1) r(i,1)], [r0(i,2) r(i,2)], 'Color', nozColors(2,:),
'LineWidth', 1);
        plot([r(i-1,1) r(i,1)], [r(i-1,2) r(i,2)], 'Color', nozColors(2,:),
'LineWidth', 1);
    end
    % plot([r(num_C,1) r(num_C+1,1)], [r(num_C,2)
r(num_C+1,2)], 'Color', nozColors(2,:), 'LineWidth', 1);
    for p = num_C+1:point_Num
        if info(p) == 0
            plot([r(pA(p),1) r(p,1)], [r(pA(p),2)
r(p,2)], 'Color', nozColors(2,:), 'LineWidth', 1);
            plot([r(pB(p),1) r(p,1)], [r(pB(p),2)
r(p,2)], 'Color', nozColors(2,:), 'LineWidth', 1);
        elseif info(p) == 1
            plot([r(pA(p),1) r(p,1)], [r(pA(p),2)
r(p,2)], 'Color', nozColors(2,:), 'LineWidth', 1);
            plot([r(pB(p),1) r(p,1)], [r(pB(p),2)
r(p,2)], 'Color', nozColors(1,:), 'LineWidth', 1);
        end
    end

    numJ = size(xT,2);
    for j = 2:numJ

```

```

        plot([xT(1,j) xT(1,j-1)], [rT(1,j) rT(1,j-1)], 'Color', nozColors(5,:), 'LineWidth', 1)
        for i = 2:lengthJ(j)
            plot([xT(i,j) xT(i-1,j)], [rT(i,j) rT(i-1,j)], 'Color', nozColors(5,:), 'LineWidth', 1)
            plot([xT(i,j) xT(i,j-1)], [rT(i,j) rT(i,j-1)], 'Color', nozColors(5,:), 'LineWidth', 1)
        end
    end
    plot(xW, rW, 'Color', nozColors(4,:), 'LineWidth', 1.5)

% --- Executes on button press in CreateGraph.
function CreateGraph_Callback(hObject, eventdata, handles)
% hObject      handle to CreateGraph (see GCBO)
% eventdata    reserved - to be defined in a future version of MATLAB
% handles      structure with handles and user data (see GUIDATA)
cd 'Two-Dimensional Code (Axi)'
num_C = str2double(get(handles.numC, 'String'));
n = str2double(get(handles.numberofpoints, 'String')); %number of
subdivisions for plotting purposes
global gamma r r0 Mach pop0 tot0 rhorh0 theta nu;
point_Num = num_C*(num_C+3)/2;

if ~isempty(r)
    clear prop p;
    val = get(handles.ParamBox, 'Value');
    switch val
        case 1
            prop = Mach;
            propThroat = 1;
        case 2
            prop = pop0;
            [propThroat, ~, ~, ~] = IsentropicRelations(1, gamma);
        case 3
            prop = tot0;
            [~, propThroat, ~, ~] = IsentropicRelations(1, gamma);
        case 4
            prop = rhorh0;
            [~, ~, propThroat, ~] = IsentropicRelations(1, gamma);
        case 5
            prop = theta*180/pi;
            propThroat = 0;
        case 6
            prop = nu*180/pi;
            propThroat = 0;
    end
    p = r;

    c = point_Num+1;
    p(c,:) = [p(end,1) 0];
    prop(c) = prop(point_Num); c = c+1;
    p(c,:) = r0(1,:);

```

```

prop(c) = prop(1);
c = c+1;
if r0(2,1) ~= r0(1,1)
    for i = 2:num_C
        p(c,:) = r0(i,:);
        prop(c) = prop(i);
        c = c+1;
    end
end
p(c,:) = [r0(1,1),0];
prop(c) = propThroat;    c = c + 1;
[b t] = MOC_pointSequences(num_C);
p(b,2) = 0;

p(c:c+num_C-1,:) = (p(t(2:end),:)/3+2*p(t(2:end)-1,:)/3);
prop(c:c+num_C-1) = prop(t(2:end)); c = c + num_C;

p(c:c+num_C-1,:) = (2*p(t(2:end),:)/3+p(t(2:end)-1,:)/3);
prop(c:c+num_C-1) = prop(t(2:end));    c = c+num_C;

for i = 1:num_C
    p(c,:) = (2*p(i,:)/3+r0(i,:)/3);
    prop(c) = prop(i); c = c + 1;

    p(c,:) = (p(i,+)/2+r0(i,+)/2);
    prop(c) = prop(i); c = c + 1;

    p(c,:) = (p(i,+)/3+2*r0(i,+)/3);
    prop(c) = prop(i); c = c + 1;

    p(c,:) = (p(i,+)/4+3*r0(i,+)/4);
    prop(c) = prop(i); c = c + 1;

    p(c,:) = (p(i,+)/8+7*r0(i,+)/8);
    prop(c) = prop(i); c = c + 1;

    p(c,:) = (p(i,+)/10+9*r0(i,+)/10);
    prop(c) = prop(i); c = c + 1;

    p(c,:) = (p(i,+)/1000+999*r0(i,+)/1000);
    prop(c) = prop(i);    c = c+1;
end

[xi,yi]=meshgrid(linspace(min(p(:,1)),max(p(:,1)),2*n),linspace(0,max(p
(:,2)),n));
zi=griddata(p(:,1),p(:,2),prop',xi,yi); clc;
cla(handles.FluidGraph,'reset');
axes(handles.FluidGraph);
contourf(xi,yi,zi,200,'LineStyle','none')
axis equal;

```



```

        colorbar
    else
        msgbox('Please create a nozzle before attempting to plot the fluid
parameters','Error');
    end
    cd ..

% --- Executes on button press in exportFluidFig.
function exportFluidFig_Callback(hObject, eventdata, handles)
% hObject    handle to exportFluidFig (see GCBO)
% eventdata  reserved - to be defined in a future version of MATLAB
% handles    structure with handles and user data (see GUIDATA)

% --- If Enable == 'on', executes on mouse press in 5 pixel border.
% --- Otherwise, executes on mouse press in 5 pixel border or over
CreateGraph.
function CreateGraph_ButtonDownFcn(hObject, eventdata, handles)
% hObject    handle to CreateGraph (see GCBO)
% eventdata  reserved - to be defined in a future version of MATLAB
% handles    structure with handles and user data (see GUIDATA)

function numberofpoints_Callback(hObject, eventdata, handles)
% hObject    handle to numberofpoints (see GCBO)
% eventdata  reserved - to be defined in a future version of MATLAB
% handles    structure with handles and user data (see GUIDATA)

% Hints: get(hObject,'String') returns contents of numberofpoints as
text
%         str2double(get(hObject,'String')) returns contents of
numberofpoints as a double

% --- Executes during object creation, after setting all properties.
function numberofpoints_CreateFcn(hObject, eventdata, handles)
% hObject    handle to numberofpoints (see GCBO)
% eventdata  reserved - to be defined in a future version of MATLAB
% handles    empty - handles not created until after all CreateFcns
called

% Hint: edit controls usually have a white background on Windows.
%       See ISPC and COMPUTER.
if ispc && isequal(get(hObject,'BackgroundColor'),
get(0,'defaultUicontrolBackgroundColor'))
    set(hObject,'BackgroundColor','white');
end

```

```

function [Mach3f, theta3f, x3f, r3f] = MOC_Axi_twoInsidePointsf2(Mach1,
theta1, x1, r1, Mach2, theta2, x2, r2, gamma, perConv)
%UNTITLED2 Summary of this function goes here
% Detailed explanation goes here

i = 1;
theta13(i) = theta1;
Mach13(i) = Mach1;
r13(i) = r1;

theta23(i) = theta2;
Mach23(i) = Mach2;
r23(i) = r2;
if r23(i) == 0
    r23(i) = 0.5;
end

convergence = 0;

while convergence == 0
    A13 = ((Mach13(i))^2-1)^(1/2)/(Mach13(i)*(1+(gamma-
1)*Mach13(i)^2/2));
    B13 = -tan(theta13(i))/((sqrt(Mach13(i)^2-1)*tan(theta13(i))-
1)*r13(i));
    C13 = tan(theta13(i)-asin(1/Mach13(i)));

    A23 = ((Mach23(i))^2-1)^(1/2)/(Mach23(i)*(1+(gamma-
1)*Mach23(i)^2/2));
    C23 = tan(theta23(i)+asin(1/Mach23(i)));

    D1 = A13*Mach1+theta1+B13*r1;

    x3(i) = (r1-r2+C23*x2-C13*x1)/(C23-C13);
    r31 = r1 + C13 * (x3(i)-x1);
    r32 = r2 + C23 * (x3(i)-x2);
    r3(i) = (r31+r32)/2;

    Mach3(i) = (2*(D1 - B13*x3(i))+A23*Mach2)/(2*A13+A23);
    theta3(i) = D1 - A13*Mach3(i)-B13*x3(i);

    i = i+1;
    r13(i) = (r1+r3(i-1))/2;
    Mach13(i) = (Mach1 + Mach3(i-1))/2;
    theta13(i) = (theta1 + theta3(i-1))/2;
    r23(i) = (r2+r3(i-1))/2;
    Mach23(i) = (Mach2 + Mach3(i-1))/2;
    theta23(i) = (theta2 + theta3(i-1))/2;

    EpsM = abs((Mach13(i)-Mach13(i-1))/Mach13(i-1));
    Epsr = abs((r13(i)-r13(i-1))/r13(i-1));
    Epst = abs((theta13(i)-theta13(i-1))/(theta13(i-1)));

```

```

        if EpsM < perConv && Epsr < perConv && Epst < perConv
            convergence = 1;
        end
    end

    Mach3f = Mach3(end);
    x3f = x3(end);
    r3f = r3(end);
    theta3f = theta3(end);

end

```

MOC_Axi_KnownFlow2.m

```

function [Mach3f, x3f, r3f] = MOC_Axi_KnownFlow2(Mach1, theta1, x1, r1,
rw, xw, thetaw, gamma, perConv)
%UNTITLED2 Summary of this function goes here
% Detailed explanation goes here

i = 1;
theta13 = (theta1+thetaw)/2;
Mach13(i) = Mach1;
r13(i) = r1;
convergence = 0;

while convergence == 0
    A13 = ((Mach13(i))^2-1)^(1/2)/(Mach13(i)*(1+(gamma-
1)*Mach13(i)^2/2));
    B13 = -tan(theta13)/((sqrt(Mach13(i)^2-
1)+tan(theta13))*r13(i));
    C13 = tan(theta13-asin(1/Mach13(i)));

    x3(i) = x1 + r1/C13;
    r3(i) = rw + (x3(i) - xw)*tan(thetaw);
    Mach3(i) = Mach1+ (theta1-B13*(x3(i)-x1))/A13;

    i = i+1;
    r13(i) = (r1+r3(i-1))/2;
    Mach13(i) = (Mach1 + Mach3(i-1))/2;
    EpsM = abs((Mach13(i)-Mach13(i-1))/Mach13(i-1));
    Epsr = abs((r13(i)-r13(i-1))/r13(i-1));
    if EpsM < perConv && Epsr < perConv
        convergence = 1;
    end
end

```

```

Mach3f = Mach3(end);
x3f = x3(end);
r3f = r3(end);

```

```

end

```

MOC_Axi_Nozzle_Design_V_2.m

```

clear all; close all; clc;
Nozzle_Exit_Desired_Mach = 1.7749;
gamma = 1.4;
num_C = 10;
tolerance = 0.00001;
rad_C = 0;

point_Num = num_C*(num_C+1)/2;
[MachExIdeal, nuExIdeal, ~] =
Prandtl_Meyer(Nozzle_Exit_Desired_Mach,[],[],1,gamma);
[~, ~, ~, AoAsExIdeal] = IsentropicRelations(MachExIdeal,gamma);

THETA_max = nuExIdeal/2;

r0(1,1) = 0; r0(1,2) = 1;
Num_Initial_Thetas = floor(num_C/4);
j = Num_Initial_Thetas;
if j == 0
    theta(1) = THETA_max/100;
    j = 1;
elseif j == 1
    theta(1) = THETA_max/100;
elseif j == 2
    theta(1) = THETA_max/100;
    theta(2) = theta(1)*5;
elseif j == 3
    theta(1) = THETA_max/500;
    theta(2) = THETA_max/100;
    theta(3) = THETA_max/20;
else
    theta(1) = THETA_max/(num_C-3)/1000;
    theta(2) = THETA_max/(num_C-3)/100;
    theta(3) = THETA_max/(num_C-3)/10;
    theta(4) = THETA_max/(num_C-3)/2;
    j = 4;
end
delTheta = (THETA_max-theta(j))/(num_C-j);
for i = j+1:num_C
    theta(i) = theta(j) + (i-j)*delTheta;

```

```

end

nu(1) = theta(1);

[Mach(1), ~, ~] = Prandtl_Meyer([],nu(1),[],2,gamma);

% Use the compatability equations
for i = 2:num_C
    nu(i) = theta(i);

    r0(i,1) = r0(1,1)+rad_C*sin(theta(i));
    r0(i,2) = r0(1,2)+rad_C*(1-cos(theta(i)));
end

%calculate characteristic slopes and the new point P's location
[le, ~, mu(1)] = Prandtl_Meyer([],nu(1),[],2,gamma);
c = -sign(le); le = abs(le);
r(1,1) = r0(1,1)+le*cos(theta(1)+c*mu(1));
r(1,2) = 0;

for p = 2:num_C
    [Mach(p), ~, ~] = Prandtl_Meyer([],nu(p),[],2,gamma);
    if p == 2
        [Mach(p), theta(p), r(p,1), r(p,2)] =
MOC_Axi_twoInsidePointsf2(Mach(p), theta(p), r0(p,1), r0(p,2), Mach(p-
1), theta(p-1), r(p-1,1), r(p-1,2), gamma, tolerance);
    else
        [Mach(p), theta(p), r(p,1), r(p,2)] =
MOC_Axi_twoInsidePoints2(Mach(p), theta(p), r0(p,1), r0(p,2), Mach(p-
1), theta(p-1), r(p-1,1), r(p-1,2), gamma, tolerance);
    end
end

% if r0(num_C,1) > r(num_C,1)
%     perError = 0;
%     r = 0;
%     r0 = 0;
%     pA = 0;
%     pB = 0;
%     Mach = 0;
%     info = Inf;
%     return;
% end

AverageFolderofImages_vE.m

%% Program to remove the fingerprint out of schlieren imagee. Only
issue
%% so far is if the no flow and flow images are not properly aligned.
%% This will result in error.

```

```

%%% written by RWP 2/2012
%%% updated by RWP 2/29/2012

clear all
close all
clc

oldPath = pwd;
cd ..
cd 'Raw Images'
[FlowName, pathflow] = uigetfile('.jpg', 'Select an Image File from one
set in the folder you want to average');
%currently processes the entire folder

cd (pathflow)

fileNames = dir('*.jpg');
Number = size(fileNames,1);

FlowName = fileNames(1).name;
FlowImage = imread(strcat(pathflow,FlowName));
fileHeight = size(FlowImage,1);
fileWidth = size(FlowImage,2);

FlowFrames = zeros(fileHeight,fileWidth,2);

currName = FlowName(1:end-9);
FrameN = 1;
for imageN = 1:Number

    FlowName = fileNames(imageN).name;
    if strcmp(FlowName(1:end-9),currName)
        FlowImage = imread(strcat(pathflow,FlowName));
        FlowFrames(:, :, FrameN) = FlowImage;
        FrameN = FrameN+1;
        if imageN == Number
            FlowImageAv = round(mean(FlowFrames,3));
            fileName = strcat(currName, '_av.jpg');
            s = uint8(FlowImageAv); % Change to integer unit
            imwrite(s, fileName, 'JPEG');
            clear FlowFrames
        end
    else
        FlowImageAv = floor(mean(FlowFrames,3));
        fileName = strcat(currName, '_av.jpg');
        s = uint8(FlowImageAv); % Change to integer unit
        imwrite(s, fileName, 'JPEG');

        clear currName
        clear FlowFrames
        FlowImage = imread(strcat(pathflow,FlowName));
        fileHeight = size(FlowImage,1);

```

```

        fileWidth = size(FlowImage,2);

        FlowFrames = zeros(fileHeight,fileWidth,2);
        currName = FlowName(1:end-9);
        FrameN = 1;
        FlowFrames(:, :, FrameN) = FlowImage;
    end
end

```

```

cd (oldPath)
msgbox('All Done');

```

FingerPrintRemoval_vE.m

```

%% FingerPrintRemoval_vE.m
%% Program to remove the fingerprint out of schlieren imagee. Only
issue
%% so far is if the no flow and flow images are not properly aligned.
%% This will result in error.

```

```

%% written by RWP 10/2010
%% updated by RWP 2/29/2012

```

```

clear all
close all
clc

```

```

%%%%% INPUTS %%%%%
    showProcess = 0;
    plotQ = 0;
%%%%% %%%%%%%%% %%%%%
oldPath = pwd;
cd ..
cd 'Raw Images'

```

```

ExperimentSetName = 'Apr2012 - Hardwalled';

```

```

[FlowName, pathflow] = uigetfile('.jpg', 'Select an image file with
Flow from the folder you want to process');
%currently processes the entire folder
s = pathflow;
c= {} ;
while ~isempty(s),
    [c{end+1}, s] = strtok(s, '\\') ;
end
dateName = char(c(end-4));
measurementName = char(c(end-3));
outputName = char(c(end-1));

```

```

sch = strcmp(measurementName, 'Schlieren');

cd (pathflow)
clc;
cd NoFlow
info = dir;
NoneName = info(3).name;

NoFlowImage = imread(NoneName);
cd ..

fileWidth = size(NoFlowImage,2);
fileHeight = size(NoFlowImage,1);

GrayImage = zeros(fileHeight,fileWidth);
start = round(1/4*fileHeight);
stop = fileHeight-start;
GrayImage(:, :) =
uint8(round(mean(mean(NoFlowImage(start:stop,start:stop),2))));
Gray2 = uint8(InvertIm(GrayImage,[],0,255));

[junk threshold] = edge(NoFlowImage, 'sobel');
fudgeFactor = 0.75;
BW_s = edge(NoFlowImage, 'sobel', threshold * fudgeFactor);
% figure, imshow(BW_s), title('binary gradient mask');
se90 = strel('line', 3, 90);
se0 = strel('line', 3, 0);
BWsdil = imdilate(BW_s, [se90 se0]);
% figure, imshow(BWsdil), title('dilated gradient mask');
borderObjects = imfill(BWsdil, 'holes');
% figure, imshow(borderObjects), title('hole in the middle filled');
seD = strel('diamond',4);
BWfinal = imerode(borderObjects, seD);
BWfinal = imerode(BWfinal, seD);
% figure, imshow(BWfinal), title('segmented image');
InvNoFlowImage = InvertIm(NoFlowImage,[],0,255);

% Removes the nozzle from the no flow image and exterior
InvNoFlowImage2 = InvNoFlowImage;
InvNoFlowImage2 = InvNoFlowImage.*uint8(BWfinal);

FingerPrint = imsubtract(InvNoFlowImage2, Gray2);
FingerPrintView = InvertIm(FingerPrint,[],0,255);

height = 0:1:fileHeight;
if sch
    center = 305;
    strength = 0.5;
    sd = 70;
else
    center = 375;

```



```

    strength = 0;
    sd = 200;
end
y = 1/(2*pi*sd)*exp(-(height-center).^2/(2*sd^2));
weight = 1 - strength/max(y).*y;
for i = 1:fileHeight
    FingerPrint2(i,:) = FingerPrint(i,:).*weight(i);
end
FingerPrintView2 = InvertIm(FingerPrint2,[],0,255);

fileNames = dir('*.jpg');
Number = size(fileNames,1);

for imageN = 1:Number
    FlowName = fileNames(imageN).name;
    FlowImage = imread(strcat(pathflow,FlowName));

    InvFlowImage = InvertIm(FlowImage,[],0,255);

    ResultInv1 = imsubtract(InvFlowImage, FingerPrint);
    ResultInv2 = imsubtract(InvFlowImage, FingerPrint2);

    Result1 = InvertIm(ResultInv1,[],0,255);
    Result2 = InvertIm(ResultInv2,[],0,255);

%
%     Result1 = imcrop(Result1,[3 4 1363 1364]);
%     Result2 = imcrop(Result2,[3 4 1363 1364]);
Result1 = mat2gray(Result1,[15 115]);
Result2 = mat2gray(Result2,[15 115]);

    if showProcess
        fullscreen = get(0,'ScreenSize');
        figure('Position',[10 50 fullscreen(3)-20 fullscreen(4)-125])
        subaxis(2,3,1, 'Spacing', 0.03, 'Padding', 0, 'Margin', 0);
        imshow(FlowImage,[0,255]);
        subaxis(2,3,2, 'Spacing', 0.03, 'Padding', 0, 'Margin', 0);
        imshow(NoFlowImage,[0,255])
        subaxis(2,3,4, 'Spacing', 0.03, 'Padding', 0, 'Margin', 0);
        imshow(FingerPrintView2,[0,255])
        subaxis(2,3,5, 'Spacing', 0.03, 'Padding', 0, 'Margin', 0);
        imshow(Result1)
        subaxis(2,3,6, 'Spacing', 0.03, 'Padding', 0, 'Margin', 0);
        imshow(Result2)
        subaxis(2,3,3, 'Spacing', 0.03, 'Padding', 0, 'Margin', 0);
        imshow(InvNoFlowImage2,[0,255])
        xlim([-0.1 1.1])
    end
    if plotQ
        figure
        imshow(Result2)
    end
end

```

```

end

outputFolder = 'Processed Images';

cd ../; cd ../; cd ../; cd ../; cd ../;
if ~exist(outputFolder, 'dir')
    mkdir(outputFolder);
end
cd (outputFolder)
if ~exist(ExperimentSetName, 'dir')
    mkdir(ExperimentSetName);
end
cd (ExperimentSetName)
if ~exist(measurementName, 'dir')
    mkdir(measurementName);
end
cd (measurementName)
if ~exist(outputName, 'dir')
    mkdir(outputName);
end
cd (outputName)
s = uint8(Result2); % Change to integer unit
imwrite(Result2, FlowName, 'JPEG');

cd (pathflow)
end

cd (oldPath)
msgbox('All Done');

```

PostProcessing_vE.m

```

%%% FingerPrintRemoval_vE.m
%%% Program to remove the fingerprint out of schlieren imagee. Only
issue
%%% so far is if the noflow and flow images are not properly aligned.
%%% This will result in error.

%%% written by RWP 10/2010
%%% updated by RWP 2/29/2012

clear all
close all
clc

%%%%%% %%%%%%%%% %%%%%%%%%
oldPath = pwd;
cd ..
cd 'Processed Images'

```

```

ExperimentSetName = 'Apr2012 - Injection (PostProcess)';

[FlowName, pathflow] = uigetfile('.jpg', 'Select an image file with
Flow from the folder you want to process');
%currently processes the entire folder
s = pathflow;
c= {} ;
while ~isempty(s),
    [c{end+1}, s] = strtok(s, '\\') ;
end
measurementName = char(c(end-2));
outputName = char(c(end-1));

cd (pathflow)
fileNames = dir('*.jpg');
Number = size(fileNames,1);

for imageN = 1:Number
    FlowName = fileNames(imageN).name;
    FlowImage = imread(strcat(pathflow,FlowName));

    FlowImageEditted = imcrop(FlowImage,[40 533 1300 450]);
    Result1 = mat2gray(FlowImageEditted,[0 150]);

    outputFolder = 'Processed Images';

    cd ../; cd ../; cd ../; cd ../;
    if ~exist(outputFolder, 'dir')
        mkdir(outputFolder);
    end
    cd (outputFolder)
    if ~exist(ExperimentSetName, 'dir')
        mkdir(ExperimentSetName);
    end
    cd (ExperimentSetName)
    if ~exist(measurementName, 'dir')
        mkdir(measurementName);
    end
    cd (measurementName)
    if ~exist(outputName, 'dir')
        mkdir(outputName);
    end
    cd (outputName)
    imwrite(Result1, FlowName, 'JPEG');

    cd (pathflow)
end

cd (oldPath)

```

```
msgbox('All Done');
```

ProcessMightexVideo_vE.m

```
%%% ProcessMightexVideo_vE
%%% Program to remove the fingerprint out of schlieren imagee. Only
issue
%%% so far is if the no flow and flow images are not properly alignned.
%%% This will result in error.

%%% written by RWP 2/2012
%%% updated by RWP 2/29/2012

clear all
close all
clc

oldPath = pwd;
cd ..
cd 'Raw Video'

[FlowName, pathflow] = uigetfile('.avi', 'Select a video file with flow
from the folder you want to process');
% processes the entire folder
disp('');
disp('*****');
disp('      If This Measurement Contained Helium Type 1 ');
disp('      otherwise type 0 and hit Enter      ');
disp('*****');
Helium = input(['Input : '], 's');
Helium = str2num(Helium);

s = pathflow;
c= {} ;
while ~isempty(s),
    [c{end+1}, s] = strtok(s, '\\') ;
end
dateName = char(c(end-4));
measurementName = char(c(end-3));
outputFolder = char(c(end-2));
outputName = char(c(end-1));
sch = strcmp(measurementName, 'Schlieren');

cd (pathflow)
clc;

NoFlowFound = exist('NoFlow', 'dir');
if NoFlowFound
    cd NoFlow
    info = dir;
```

```

NoneName = info(3).name;

NoFlowVideo = VideoReader(NoneName);

fileWidth = NoFlowVideo.Width;
fileHeight = NoFlowVideo.Height;
NoFlowFrameRate = NoFlowVideo.FrameRate;
NoFlowFrameNum = NoFlowVideo.NumberofFrames;
NoFlowImageFrame = zeros(fileHeight,fileWidth,NoFlowFrameNum);

for i = 1:NoFlowFrameNum%NoFlowFrameNum
    NoFlowImageFrame(:, :, i) = rgb2gray(read(NoFlowVideo,i));
end
NoFlowImage = round(mean(NoFlowImageFrame,3));
clear NoFlowImageFrame
cd ..
else
    disp('No NoFlow Image Found, note you will');
    disp('not be able to post process and remove the fingerprint');
end

fileNames = dir('*.avi');
Number = size(fileNames,1);

for imageN = 1:Number
    FlowName = fileNames(imageN).name;
    FlowVideo = VideoReader(strcat(pathflow,FlowName));
    FlowName = FlowName(1:end-4);

    FlowFrameRate = FlowVideo.FrameRate;
    FlowFrameNum = FlowVideo.NumberofFrames;
    fileWidth = FlowVideo.Width;
    fileHeight = FlowVideo.Height;
    FlowImageFrame = zeros(fileHeight,fileWidth,FlowFrameNum);

    cd ../; cd ../; cd ../; cd ../; cd ../;
    if ~exist('Raw Images', 'dir')
        mkdir('Raw Images');
    end
    cd ('Raw Images')
    if ~exist(dateName, 'dir')
        mkdir(dateName);
    end
    cd (dateName)
    if ~exist(measurementName, 'dir')
        mkdir(measurementName);
    end
    cd (measurementName)
    if ~exist(outputFolder, 'dir')
        mkdir(outputFolder);
    end
    cd (outputFolder)

```

```

if ~exist(outputName, 'dir')
    mkdir(outputName);
end
cd (outputName)

if NoFlowFound
    if ~exist('NoFlow', 'dir')
        mkdir('NoFlow');
    end
    cd 'NoFlow'
    fileNameNo = strcat(outputName, '_NoFlow', '.jpg');

    data = NoFlowImage;
    s = uint8(data); % Change to integer unit
    imwrite(s, fileNameNo, 'JPEG');
    cd ..
end
if Helium
    for i = 1:FlowFrameNum%NoFlowFrameNum
        fileName = strcat(FlowName, '_', char(sprintf('%04d',
i)), '.jpg');
        FlowImageFrame = rgb2gray(read(FlowVideo,i));
        s = uint8(FlowImageFrame); % Change to integer unit
        imwrite(s, fileName, 'JPEG');
    end
else
    for i = 1:FlowFrameNum%NoFlowFrameNum
        FlowImageFrame(:, :, i) = rgb2gray(read(FlowVideo,i));
    end
    if FlowFrameNum < 3
        framePull1 = 1;
        framePull2 = 2;
    else
        framePull1 = floor(1/3*FlowFrameNum);
        framePull2 = floor(2/3*FlowFrameNum);
    end

    FlowImage01 = FlowImageFrame(:, :, framePull1);
    FlowImage02 = FlowImageFrame(:, :, framePull2);
    FlowImageAv = floor(mean(FlowImageFrame, 3));
    clear FlowImageFrame

    s = FlowName;
    c= {} ;
    while ~isempty(s),
        [c{end+1}, s] = strtok(s, '_') ;
    end
    FlowName2 = strcat(char(c(end-1)), '_', char(c(end)));

    oldpath2 = pwd;
    fileNameav = strcat(outputName, '_av_', FlowName2, '.jpg');
    fileName01 = strcat(outputName, '_01_', FlowName2, '.jpg');

```

```
fileName02 = strcat(outputName, '_02_', FlowName2, '.jpg');

data = FlowImageAv;
s = uint8(data); % Change to integer unit
imwrite(s, fileNameav, 'JPEG');
data = FlowImage01;
s = uint8(data); % Change to integer unit
imwrite(s, fileName01, 'JPEG');
data = FlowImage02;
s = uint8(data); % Change to integer unit
imwrite(s, fileName02, 'JPEG');
end
cd (pathflow)
end

cd (oldPath)
msgbox('All Done');
```